To the Graduate Council:

I am submitting herewith a dissertation written by Young Keun Chang entitled 'Dynamics of Vortex Rings in Cross-Flow.' I have examined the final copy of this dissertation for form and content and recommend that it be accepted in partial fulfillment of the requirements for the degree of Doctor of Philosophy with a major in Aerospace Engineering.

Ahmad D. Vakili, Major Professor

We have read this dissertation
and recommend its acceptance:

John E. Caruthers

Roy J. Schulz

Accepted for the Council:

Vice Provost
and Dean of the Graduate School

DYNAMICS OF VORTEX RINGS IN CROSS-FLOW

A Dissertation

Presented for the

Doctor of Philosophy

Degree

The University of Tennessee, Knoxville

Young Keun Chang

December 1991

Acknowledgements

I would like to express my deepest gratitude to my major professor and supervisor of the doctoral committee, Dr. Ahmad D. Vakili for his continuous support and guidance provided during this work. His broad knowledge and keen sense of experimental techniques combined with nice personality were greatly appreciated. Special appreciation is extended to Dr. Jain-Ming Wu for teaching how to approach and think about in solving the scientific problems. Appreciations are also given to other committee members who reviewed this dissertation carefully, Dr. Trevor Moulden, Dr. John Caruthers and Dr. Roy Schulz.

I would also like to thank Mr. Richard Ray, Mr. Harold Sartain, Mr. Ricky Meeker and Mr. Jim Boazman of Wind Tunnel Laboratory in UTSI for their assistance during the experimental phase of this work. Special thanks are expressed to late Mr. Loyd Lester for his invaluable idea on the design and construction of models.

I wish to thank my mother, Jung-Ok Choi Chang, and other members of my family who support and encourage me to continue higher education in this country. My only regret is that one of my elder brothers, Young Tae Chang, is not alive to share this achievement with me.

I also want to appreciate my wife, Hye Jung, for her continuous encouragement, and I am indebted to my lovely son and daughter, Jiwon and Jenny, for not sharing more time with them.

Finally, this work was supported by Office of Naval Research under the grant number N00014-89-1696. Their support is greatly appreciated.

Abstract

Vortex rings formed in a cross-flow by continuous and/or single pulsations of a jet were studied. The pulsations were provided by the periodic closing and opening of a jet flow and/or by the sudden movement of a circular piston inside a cylinder, respectively. Single pulsations were selected to investigate the effects of different jet exit geometries on the generation, dynamics and penetration of vortex rings: one geometry was a straight walled tube, and the other was a sharp-edged orifice with the same exit diameter. Continuous pulsation was used to study its effects on the development of vortex rings and their penetration in a cross-flow. Pulsation frequency and the ratio of piston velocity to cross-flow velocity were selected as key parameters for each experiment. Detailed measurements were made using flow visualization techniques, including laser induced fluorescence, and hot-film anemometry. Characteristic parameters investigated consisted of the translational velocity, circulation, diameter and core of the ring. To theoretically simulate the dynamics of vortex rings in cross-flow, a numerical simulation for three-dimensional vortex rings was performed based on a Lagrangian, grid-free, three-dimensional vortex method. For continuous pulsations, it was found that, at low frequencies, the fluid in the vortex rings penetrated into the cross-flow to a height much greater than that for high frequency pulsation or for a steady jet injection (up to five times). Dynamically, the downstream segment of the vortex rings moved upward (tilted) by about $3°$ to $4°$ under the effect of interaction between the vortex ring and the cross-flow. This type of motion was also qualitatively predicted by the numerical simulation of three-dimensional vortex rings in cross-flows. The detailed velocity field within a vortex ring generated by pulses at 1 Hz was measured using a hot-film probe. From the study of the velocity field

along the exit centerlines it was observed that the vortex rings were fully-formed at $Z = 3.0\ d_j$. This is in agreement with other experiments in air as well as computational results. Single pulsations showed that the vortex ring penetration height was much greater for a sharp-edged orifice than for a straight walled tube, for the same piston and cross-flow velocities. Hence, it was seen that the jet exit boundary condition is a key parameter which determines the formation process of a vortex ring, its penetration and characteristic parameters mentioned above.

Table of Contents

List of Figures

List of Tables

List of Symbols

A	empirical constant in the equation of ring translational velocity
a	core radius of ring
C	constant $(R(t)a^2(t))$ in equation (4-1)
D	ring diameter
D_p	piston diameter
d_c	vortex ring core diameter
d_j	jet exit diameter
F_1	force acting on the forward portion of ring in Figure 2.2
F_2	force acting on the rearward portion of ring in Figure 2.2
f	frequency (Hz)
K	reducing coefficient in equations (2-2) & (2-4)
k	similarity parameter in equation (4-14)
k_1	yaw factor in hot-film probe
k_2	pitch factor in hot-film probe
l_d	separation distance between adjacent vortex rings
l_{fm}	modified frequency-momentum length scale
L_p	piston stroke length
$\dot{Q}$	flow rate in jet flow
R	vortex ring radius
Re	Reynolds number based on circulation and viscosity
Re_{d_e}	Reynolds number based on jet exit conditions

T_p	time duration of piston motion
Δt	time interval between vortex ring generation
δt	increment between time steps
$\overline{U}$	mean velocity component in X-direction
U_c	jet centerline velocity at the exit
$\overline{U}_{eff}$	effective cooling velocity
$\overline{U}_p$	average piston velocity
$\overline{u}$	mean pulsating velocity
$\overline{u_s}$	slip velocity
$\overline{U}_j$	average jet exit velocity
U_{ie}	inner edge velocity of ring core
U_{oe}	outer edge velocity of ring core
U_{max}	peak velocity at inner edge of ring core
U_N	velocity component normal to the sensor
U_{BN}	binormal velocity component of the sensor
U_{rot}	rotational velocity of vortex ring core
U_∞	cross-flow velocity
U_T	translational velocity of vortex ring
U_{R1}	resultant velocity acting on the forward section of ring
$\overline{W}$	mean velocity component in Z-direction
X	coordinate in the streamwise direction
Y	coordinate perpendicular to XZ plane
Z	coordinate along the jet axis

X_1, X_2	locations where the forces F_1 & F_2 are acting on, measured from the geometric center of the ring in the upstream and downstream directions, respectively
α	probe slant angle
β	angle between cross-flow and local segment of the ring in the plane of ring
ρ	density
ϕ	yaw angle of the probe
ψ	pitch angle of the probe
θ	rotation angle measured from the reference plane about Z-axis
$\dot{\theta}$	angular velocity at inner and outer edges of ring core
Γ	circulation of each ring filament in computations
Γ_i	initial circulation of vortex ring
Γ_c	effective core circulation of ring
Γ_m	measured circulation of ring
γ	circulation per unit length of a cylindrical vortex sheet
ν	kinematic viscosity

Subscripts

1	condition at the forward portion of ring
2	condition at the rear portion of ring
c	vortex ring core
i	initial condition

ie	inner edge
e	exit
eff	effective
oe	outer edge
j	jet condition
p	piston
T	translational quantity
∞	free-stream condition

1. Introduction

1.1 Background

Efficient mixing of two fluids frequently plays a major role in fluid engineering problems affecting combustion, propulsion, petrochemical, food engineering and environmental applications. In these applications, a fluid is frequently introduced in the form of a jet into a main flow. The spread of a fluid jet into an ambient stream occurs at a fixed rate which is too slow under certain conditions. As a result, mixing enhancement techniques are frequently introduced into the jet flow to increase the mixing rate between the jet and the surrounding fluid. An important technique for enhancing the mixing of axial jet flows has been to introduce different periodic disturbances into the mixing process to increase the rate of mixing.

Pulsation of axial jets for mixing enhancement was first introduced through the development of the pulse jet engine (Lockwood, 1963). He noted the generation of vortex rings by pulsating flow. Sarohia and Bernal (1981) attempted to improve mixing of a round turbulent jet by pulsating the mean flow. Reynolds and Bouchard (1981) noted that, by forcing the jet at a sufficient amplitude and at a well-chosen frequency, jet entrainment can be suppressed in a whole region of the jet. Mixing improvement in pulsating turbulent jets was examined by Binder and Favre-Marinet (1973, 1981). They showed that both the decay of the centerline velocity and the axial distance of the jet were strongly affected by pulsations. Bremhorst and Harch (1979) investigated the effects of pulsing an air jet with large amplitudes for frequencies of 10 and 25 Hz. They found that local entrainment in the jet was increased by up to three times within $x/D = 17$ compared to the steady jet. Vandsburger et al. (1986) used a loudspeaker to excite a laminar flame at a frequency of 16 Hz and observed the formation of large-scale vortex rings in the flame zone. Recently, an experimental study of the effects of strong axisymmetric pulsing on a free, vertical turbulent jet diffusion flame was presented by Lovett and Turns (1990). The jet flame was pulsed over the frequency range of 2-1300 Hz with different ranges of amplitudes. The average length and width of the luminous flame were measured to examine the effect of pulsing on the overall flame dimensions. The results showed that a turbulent jet flame is sensitive to axisymmetric pulsing of the stream and that the effects observed are largely frequency-dependent.

Next, as an efficient means to enhance the mixing process through deeper penetration and increased entrainment rate, Wu et al. (1988) introduced a transverse injection with forced pulsation into a uniform cross-flow with unsteady effects. Introducing unsteadiness in the jet of such flows generally resulted in flow patterns and features which were totally different from those of a steady jet and which could be of considerable value in improving the mixing rate and increasing the diffusion and entrainment of jets in cross-flow. At low frequencies, vortex rings are formed penetrating into the cross-flow with relatively high speeds. The penetration level, translational speed of the vortex ring and the entrainment rate will be important parameters that determine the mixing process. Also, these parameters are dependent upon the ratio of cross-flow velocity to ring translational velocity and pulsation frequency.

The superiority of scramjets for hypersonic flight has been known since the late 1950s. In the scramjet combustors, the development and growth of the shear layers which are responsible for the mixing of fuel and air are relatively much slower in supersonic flows than in subsonic flows. The reasons for reduced mixing at Mach numbers greater than 1 are known to result from high fluctuating Mach numbers, the consequent formation of transient eddy shocklets, and the influence of compressibility on turbulent free mixing (Hussaini et al., 1985). Therefore, mixing enhancement is one of the important problems for scramjet combustor designs. Conventional mixing techniques are inefficient and may lead to significant drag increase, so, new approaches must be developed to accomplish enhanced mixing at supersonic speeds. One of the mixing techniques to enhance turbulence and mixing rate is to provide for an enlarged mixing area by the increase of jet flow penetration. Our new approach utilizes the transverse injection of a jet into the mainstream in a pulsed manner to optimize the mixing between the two streams. The pulsation of jet injection in a controlled manner is not only a means to improve the jet and ambient flow mixing process but it is also a way towards controlling the dump type combustor instabilities.

To better understand the relationships of pulsations to mixing enhancement, some basic questions should be answered. Since the vortex ring in cross-flow has not been studied in detail before, this fundamental study is conducted to try to answer some basic questions. In the process of identifying key variables and for better understanding the physical phenomena involved, an experimental study was performed on the transverse injection with pulsation in the cross-flow. In the next section, a literature survey of vortex rings formed at low frequency and/or by discrete jet pulsation will be presented as a first step for this study.

1.2 Literature Review on Vortex Ring Studies

Vortex ring phenomena have been the focus of research by many investigators for over a century ever since Helmholtz (Thomson, 1883) formulated the general vortex theorems. The motion of vortex rings is one of the interesting fluid phenomena with concentrated vorticity. The fact that a vortex ring can transport fluid and momentum over a certain distance has been one of the motivations for vortex ring research.

This part is divided into five subsections; experimental, analytical and numerical investigations for the formation, motion and disintegration of vortex rings in quiescent flow, the interactions of mutual vortex rings, and applications of ring problems.

1.2.1 Experimental Work

A large volume of literature has been devoted to experimentally investigating the formation, structure, decay and motion of laminar and turbulent vortex rings in quiescent fluids. The early works on the vortex ring phenomena are well described in the paper by Guhler and Sallet (1979). These early studies (Thomson (1883), Hicks (1885)) are based on the following simplifying assumptions; the ratio of core radius to ring radius, a/R, is very small and the vorticity is concentrated in the vortex core. These classic considerations were extended later by Fraenkel (1970) and Norbury (1973). They assumed that the core shape and vorticity distribution in the core are important factors to calculate the translational velocity of non-deforming vortex rings. Recently, more interest in the study of vortex rings has been focused on the behaviour and structure of viscous vortex rings including turbulent vortex rings.

Krutzsch (1939) studied the propagation, decay and stability of a laminar vortex ring using trace technique. This is considered to be the first paper to report experimental studies on a vortex ring.

Magarvey and Maclatchy (1964) used photography to extensively investigate the formation, structure and disintegration of vortex rings by flow visualization with smoke in air. They inferred from the experimental evidence that the vortex ring formed at the orifice is not a true ring, but a layer of disperse fluid rolled about a circular axis. A qualitative investigation was made of the flow patterns within the structure, but no attempt was made to relate velocities to ring geometry. They studied the mechanism by which a fully developed ring is destroyed as it impacts on a solid surface.

A quantitative study of the detailed structure of a vortex ring in air has been accomplished using hot-wire anemometry and high-speed motion picture photography by Akhmetov and Kisarov (1966). The velocity field and streamline pattern have been determined, together with the vorticity distribution. It was shown that the vorticity is almost entirely localized in the vortex ring core and quickly diminishes with distance from the core center.

The propagation property of vortex rings in air has been investigated by using stroboscopic photography and hot-wire anemometry by Johnson (1970). The study was devoted to accurately measuring the decay of real vortex rings in quiescent air and comparing calculated ring behaviour with the various theoretical predictions. He noted that the linear momentum of vortex rings is conserved and that the ratio of vortex ring radius to core radius is approximately constant.

Experimental studies on the motion of vortex rings ejected from a circular and a lenticular orifice were conducted by Oshima (1972). It was found that there is a favorable range of impulse to produce the stable vortex ring. The vortex ring ejected from the lenticular shape orifice was deformed intermittently in the plane of the ring and bends forward and backward.

Sullivan et al. (1973) measured the axial and radial velocity distribution in vortex rings using a two-component laser doppler velocimeter. The circulation, streamlines and vorticity distribution were found throughout the ring from the results of the axial and radial velocities measured prior to the instability. They also noted that vortex rings are unstable to azimuthal perturbations.

Sallet and Widmayer (1974) measured the characteristic features of laminar and turbulent vortex rings with hot-wire anemometers. These measurements were comprised of the translational velocity, ring diameter, core diameter, and circulation at several points downstream from the orifice exit. In addition to the quantitative description of vortex rings, the study showed that vortex rings are fully-formed within three ring diameters downstream from the exit.

The thorough discussion of the structure and stability of viscous vortex rings was qualitatively performed in a series of papers by Maxworthy (1972, 1974, 1977). Using flow visualization and laser doppler velocimetry he investigated the formation process, vorticity, the flow fields, the translational velocity, and stability of vortex rings over a wide range of Reynolds numbers.

The temporal development of the rolling-up process of vortex rings was investigated in detail using flow visualization and laser doppler velocimeter by Didden (1979). He examined the variation of velocity, diameter, and circulation of vortex rings which move between the point of formation and a location three jet diameters downstream.

Guhler and Sallet (1979) also studied the formation and intial motion of vortex rings. Their results represent the geometric and kinematic relationships between the vortex ring and the initial cylindrical slug model of fluid which formed the ring.

Glezer (1988) categorized the generating conditions for vortex rings and classified the conditions under which a given vortex generator produces either an initially laminar ring, which may or may not undergo instability and transition to turbulence, or an initially turbulent ring. He also suggested a possible connection between generating conditions and the transition to turbulence.

Auerbach (1991) studied vortex ring evolution experimentally, from the initial roll-up phase through to the final turbulent phase, to investigate the dependence of its stirring properties on both the initial piston motion as well as on the boundary conditions. He showed that stirring between fluid initially upstream and that initially downstream of the nozzle plane is done more by convective entrainment at the beginning (roll-up and contraction phases), by diffusive entrainment during the laminar and wavy phases, and by mixed entrainment and ejection during the transition to turbulence and the turbulent phase itself.

1.2.2 Analytical Work

Systematic research on the stability of vortex rings have been theoretically and experimentally performed by Widnall et al. (1973, 1974). They showed that a vortex ring is unstable to short azimuthal bending waves, which was also demonstrated by Didden (1979).

The motion and decay of a vortex in a two-dimensional, incompressible, nonuniform flow field was studied by Ting and Tung (1965). By including the viscous effects in the inner core of the vortex and applying a matched asymptotic expansion technique, they eliminated the mathematical singularity, which is the main drawback of the inviscid model.

Fraenkel (1970) found approximate but explicit formulae for the translational velocity and shape of vortex rings in the nearly plane, or two-dimensional, nature of the flow in the neighborhood of a small cross-section. The study was restricted to rings whose cross-sectional area is small relative to the square of a mean ring radius.

Motion of vortex rings with bilaterally symmetric initial shape was investigated theoretically and experimentally by Viets and Sforza (1972). The induced velocity was related to the motion of the ring according to two different concepts: a hydrodynamic vortex and a Rankine vortex. In the Rankine vortex analysis the local relative velocity produces lift and drag forces on the ring, which then distort the ring. This concept treats each segment of a vortex ring as if it were a locally two-dimensional spinning cylinder. Lift and drag on the ring are then evaluated based on the Kutta-Joukowski result (see, e.g., Ting & Tung (1965)).

The formula for the velocity of a ring in an ideal fluid with an arbitrary distribution of vorticity in the core was analytically derived by Saffman (1970). He also concluded that the method used to calculate the ring velocity in an ideal fluid can be extended to find the velocity of a "real" viscous vortex ring.

Kambe and Oshima (1975) studied the generation and decay of vortex rings in a viscous fluid by using a solution in the form of an asymptotic expansion and numerical integration of the Navier-Stokes equation. Time-dependent physical quantities such as total energy, impulse and velocity of vortex rings were obtained.

1.2.3 Numerical Work

Many studies have been done based upon vortex methods to simulate a vorticity-dominated flow of an incompressible, two-dimensional flow since Rosenhead (1931). Even though the method has some inherent difficulty that has limited the application of the method, it is generally known that the rotational region of fluid motion is well simulated by a number of discrete vortex filaments in an inviscid flow. A vortex ring is a typical example of vorticity-dominated flow with small compact region of vorticity. There have been a lot of simulations of two-dimensional axisymmetric vortex rings. But, some studies were done on three-dimensional vortex ring configuration with variations of size, position and shape considered together. A series of vortex rings can be simulated by the three-dimensional discrete vortex method and the time dependent variation of each discretized vorticity followed. Then the motion of three-dimensional vortex rings can be traced.

The detailed analysis and review of the vortex method were given by Leonard (1980, 1985), Ashurst (1988), Sarpkaya (1989) and Chorin (1989) in modelling jets, wakes, boundary layers, vortex rings, and other vorticity-dominated flow.

A comprehensive review (Sarpkaya, 1989) was presented of the computational methods and procedures based on Helmholtz's powerful concepts of vortex dynamics, making use of Lagrangian or mixed Lagrangian-Eulerian schemes, the Biot-Savart law or the Vortex-in-Cell methods. Ingenious approximations and smoothing schemes that were developed in search of predictive models, qualitative solutions, new insights, or just for inspiration in the simulation of, usually incompressible, fluids in two- and three-dimensions, were described in detail.

Whitehead (1968) presented a detailed numerical study of the generation and development of a viscous vortex ring. The vorticity transport equation and the definition of the vorticity equation were derived in order to solve for velocity vector fields, vorticity contours, and streamline patterns. The radius, trajectory, and velocity of the ring were calculated and employed to predict the propagation velocity of a vortex ring using the vortex models of Helmholtz and Hill.

Oshima & Kuwahara (1984) studied three-dimensional vortex ring interactions numerically as well as experimentally by considering the viscous dissipation.

The trailing vortices in a shear wind were modeled theoretically and numerically by Liu & Ting (1986) as a two-dimensional configuration of the vortex ring in a cross-flow, based on an unsteady, two-dimensional, rotational flow field with a concentration of large vorticity in a pair of "vortical spots". Their results showed that both vortices will initially drift forward together, spread apart, and move downward. Gradually, under the effects of mutual interaction, the redistribution of the background vorticity changes the trajectories. The vortex that is in the opposite sense to that of the background flow will reach a minimum height, reverse its downward drift, and turn upward, whereas the other vortex will eventually reverse its forward motion and turn backward. The numerical results also demonstrated the strong interaction between the trajectories of the vortical spots and the change of the vorticity distribution in the background flow field.

Chorin (1973, 1978, 1980) introduced a technique called the random vortex method by implementing two additional mechanisms to solve the equations of viscous, incompressible flow; one mechanism was to satisfy the no-slip boundary condition at the solid boundaries through vorticity generation, and the other mechanism was the transports of vortex elements by diffusion. The viscous diffusion was simulated by the random walk motion of the vortex elements based on Gaussian distributed random numbers. This numerical scheme has been successfully applied to flow past an impulsively started cylinder (Cheer, 1983), unsteady separated wake development past a cylinder (Cheer, 1989), stability of the boundary layer (Chorin, 1980), driven cavity flow (Choi et al., 1988), flow past a backward facing step (Sethian and Ghoniem, 1988), blood flow through heart valves (McCracken and Peskin, 1980) and wind flow over a building (Summers et al., 1985). The random walk algorithm is compatible with the traditional vortex method from the point of view that both methods use a Lagrangian, grid-free formulation.

1.2.4 Mutual Interactions

A series of papers was published by Oshima and her colleagues (1975, 1977a,b,

1978) who reported on experimental investigations of the interaction of multi-vortex rings. Oshima et al. (1975) examined the interaction of two vortex rings moving along the same axis of symmetry by experiments and numerical analysis. The mutual slip-through of two vortex rings does not happen at low Reynolds number. This game of passing through each other was successfully accomplished in air experiment by Yamada and Matsui (1978). Their experiment was conducted with larger vortex ring diameters and larger circulations, resulting in larger Reynolds numbers, compared to those used by Oshima et al. (1975). Oshima and Asaka (1977a) investigated the interaction of two vortex rings along their parallel axes in air. They found three typical patterns of vortex rings, depending on their initial speeds; (1) At low speeds, two rings merged into one distorted ring. (2) at higher speeds, it splits into two rings after merging. (3) At much higher speeds, they merge, split and merge again into one ring before they diffuse away. They (1977b) also experimentally studied the interaction of vortex rings simultaneously ejected from a number of orifices. Oshima (1978) carried out experimental studies of head-on collision of two vortex rings. These showed that the trajectories of the colliding rings were different from the trajectory of one ring impacting against a solid wall.

Fohl and Turner (1975) similarly observed the interaction between pairs of vortex rings during certain collisions. Oshima and Izutsu (1988) recently investigated the mechanism for cross-linking two vortex rings. It was found that a new pair of vortex tubes was created, which connected the interacting vortex rings and grows gradually, while the vorticity intensity of the main ring decreases.

The behaviour of vortex rings in the vicinity of a wall was described by Boldes and Ferreri (1973). Their experimental study showed that a vortex ring moving toward a wall normal to its axis may undergo momentary reversals of its forward velocity. They qualitatively predicted the rebound phenomenon, and attributed it to generation of a separated shear layer on the wall. Similar experimental studies were carried out on such flowfields by Yamada et al. (1982). They confirmed Boldes and Ferreri's conjecture.

The detailed characteristics of the flow induced by a vortex ring approaching a plane wall was investigated by Walker et al. (1987). Their experimental and theoretical results showed that an unsteady separation develops in the wall boundary layer flow, in the form of a secondary ring attached to the wall. A period of explosive boundary layer growth then ensues and a strong viscous-inviscid interaction occurs in the form of the ejection of the secondary vortex ring from the boundary layer. Then the primary vortex ring interacts with the secondary ring and in some cases a third, tertiary ring is induced near the wall.

Cerra and Smith (1983) examined the interaction of a convecting vortex ring with a laminar boundary layer above a solid surface to develop a better understanding of the behaviour and interaction of a ring vortex element in the vicinity of a solid boundary. They found a speculiar trajectory of the vortex ring and pronounced tilting of the ring inside the boundary layer above the solid surface. They assumed that the increase in angle of the vortex ring as it approaches the solid surface can be explained plausibly by the interaction between the vorticity of the vortex ring and the vorticity of the boundary layer. However, as they mentioned, their discussion is much too simple to adequately explain the interaction occurring between the primary vortex ring and the boundary layer vorticity. The boundary layer vorticity should be properly considered as a field or distributed vorticity to fully explain the results of this study.

The flow field produced by the oblique collision of two laminar vortex rings was studied by Schatzle (1987) in his thesis. Spatial finite differences of the velocity data were calculated and used to compute the vorticity field and the strain field resulting from the collision. A dramatic change was observed in the structure of the vorticity field during the interaction: the vortex ring cores were observed to become elongated in the mean direction of travel due to the straining field, and the circulation of the colliding cores decreases during this time.

An experimental study was made of the interaction of a vortex ring with an inclined wall (1989). Flow visualizations revealed the formation of bi-helical vortex lines around the circumferential axis of the ring due to variations in the rate of vortex stretching along the circumference of the ring. These bi-helical vortex lines, once generated, are constantly being displaced along the circumferential axis and are eventually compressed onto the plane of symmetry by the induced velocity field of the secondary vortex.

The interaction of a free surface with a vortex ring moving parallel to the surface was described by Bernal and Kwon (1989). They noted that the interaction results in vortex tube reconnection similar to the reconnection process of colliding vortex rings described by Oshima and Izutsu (1988). The second interaction results in the generation of vorticity at the free surface in a manner reminiscent of a solid surface (Walker et al., 1987), or at a density interface (Dahm et al., 1989)

Bernal et al. (1989) also reported the interaction of a free surface with vortex rings and vortex pairs moving perpendicular to the surface when different amounts of surface active agents (surfactants) are present on the surface. They noted that very small concentrations of surfactant material in the bulk water can result in significant changes in surface tension when and if the material reaches the surface. This resulted in the generation of increased amounts of secondary vorticity when additional surface active agents are present on the surface.

1.2.5 Applications

It is well known that vortex structures are commonly observed within the coherent structures in turbulent boundary layers. Falco (1982) and Doligalski et al. (1980) have proposed that the coherent structures observed in a turbulent boundary layer may be caused by the interaction of vortices with fluid near the boundary surface.

To provide a better understanding of the turbulent shear flow in complicated flow problems, vortex ring interactions with a turbulent boundary layer were studied by Chu and Falco (1988). These were fundamental researches on coherent structures in turbulent shear flows in terms of active agents of the mixing process.

The interactions of two identical rings moving on a collision course along parallel lines were investigated using a vortex-in-cell method in terms of mixing by Zawadzki and Aref (1991). Diagnostics of mixing of the scalar particles demonstrated an improvement in mixing as the offset of the lines of propagation of the vortices is increased from zero to about a quarter of the ring diameter. With further increase of the offset, the mixing is gradually reduced due to a vortex reconnection process. They noted an interesting findings that vortex connection may not be as important a source of mixing as one might intuitively expect.

Southerland at al. (1991) recently presented an experimental study of the molecular mixing of a dynamically passive conserved scalar quantity in an axisymmetric laminar vortex ring. It showed the diffusional cancellation term arising in the scalar dissipation transport equation plays an important role in limiting the total amount of mixing that takes place.

A flow model consisting of a train of randomly spaced viscous vortex rings was employed by Fung et al. (1979) and Liu et al. (1979) in order to simulate the pressure field in the acoustic region near an axially symmetric jet. The time interval between the shedding of successive vortices was taken to be a random variable with a probability distribution chosen to match that from experiments.

Wan and Payne (1989) developed an unsteady vortex ring model to simulate microburst (low-level wind shear) generated by a thunderstorm or a small rain cloud. They showed that the microburst resembles a turbulent free jet at altitude and a vortex ring both in mid-air and near the ground surface.

1.3 Objectives and Approach of the Present Study

The present work was originally initiated to investigate the behaviour of steady jets in a cross-flow. Steady jets in a cross-flow have been extensively studied due to their practical aerodynamics applications, e.g. the cooling of combustion products, VTOL aerodynamics and the discharge of an effluent into a waterway or air. Many experimental studies (Keffer & Baines (1963), Kamotami & Grober (1972), Andreopoulos & Rodi (1984)) present the striking features of deflected jet dynamics, including the transition from an initially vertical jet through a bending phase during which the jet becomes aligned with the cross-flow and takes the form of two counter-rotating vortices with that flow. In the study of wing tip jets blowing from rectangular orifices in a wing tip, Wu et al. (1982) observed " spin-off" vortices. Further investigations by Wu & Vakili (1984) and Wu et al. (1986) revealed a system of auxiliary vortices, which they named as follows: jet vortices, wake vortices and spin-off vortices. These vortices compose a complicated vortical flow field downstream of asymmetrical jets injected into a uniform cross-flow.

To the author's knowledge, there has not been a systematic study of the dynamics of vortex rings in cross-flows. Wu, et al. (1988) introduced and studied the pulsating jet concept in a cross-flow. Their study was mainly undertaken as an extension of an effort to investigate the flow field of asymmetric jets in cross-flows and to examine the effect of jet flow periodicity on the resulting flow field. Their study especially concentrated on the origin of various vortices which were generated by the jet in the downstream flow. They showed that once the jet flow pulsated it resulted in the formation of vortex rings that, at low frequencies, penetrated into the cross-flow deeper than the steady jet flow. The penetration depth was reduced, when the jet were pulsated at high frequencies. The frequency range investigated in this study was 1 Hz to 16 Hz.

A qualitative analysis of vortex rings in cross-flow will be done in the present study using a simple approach to discuss the physical mechanism of added ring penetration by applying engineering analysis to the experimental results. The analysis given here is limited to flow situations where the spacing between the sequential vortices are large (low frequency pulsation and low speed flows), that is, where the interactions between such rings may be ignored.

Since most of the vorticity of rings created by jet pulsations is generated in the boundary layer on the wall of the cylinder and around the exit where the jet flow is created, it is postulated that the jet exit boundary condition is a very important parameter to determine the amounts of vorticity and the formation process of a vortex ring. Irdumsa & Garris (1987) observed qualitatively different vortex rings when generated by an orifice and by a chimney nozzle in quiescent ambient conditions. They noted that exit boundary conditions of the vortex ring generator can have a very large effect on the entrainment and energy distribution of the rings. Pullin (1979) investigated the formation, at tube and orifice openings, of vortex rings generated by the motion of a piston. For large Reynolds numbers the ring diameter and circulation were not strongly dependent on the piston velocity profile. The present study will investigate how different exit geometries result in the generation of vortex rings and how vorticity affects the dynamics and kinematics of the vortex rings with different piston/cross-flow velocity ratios for the case of single pulsation.

The primary purpose of the present study is to investigate the penetration trajectory of vortex rings and the motion of the vortex ring in cross-flows. The secondary purpose of this study is to investigate the mixing improvement of pulsed jet flow with cross-flow.

This study will be conducted in three steps. First, an experimental investigation will be carried out of vortex rings produced by pulsed transverse jet injection into a uniform, subsonic cross-flow using flow visualization techniques and hot-film anemometry. The dynamics of ring growth and propagation, and the resulting level of mixing improvement will be examined. Second, an analytical model of the vortex ring in a cross-flow will be formulated, developed and applied to compare the predicted characteristic parameters of the vortex ring with experimental results. Third, a numerical simulation of a three-dimensional vortex ring will be performed based upon a Lagrangian, grid-free, vortex method to support the results of the experimental investigations. In this study, the discrete vortex filament method will be used to simulate the motion of vortex rings in cross-flows, and its time evolution. It is intended to show that some of the characteristics and mechanisms can be reproduced by a numerical simulation of this kind, since a detailed understanding of the interaction between cross-flow and vortex rings is important in terms of entrainment and mixing control.

The schematic chart of the systematic vortex ring research in cross-flow being carried out in the laboratory is presented in Figure 1.1. A detailed study of mixing

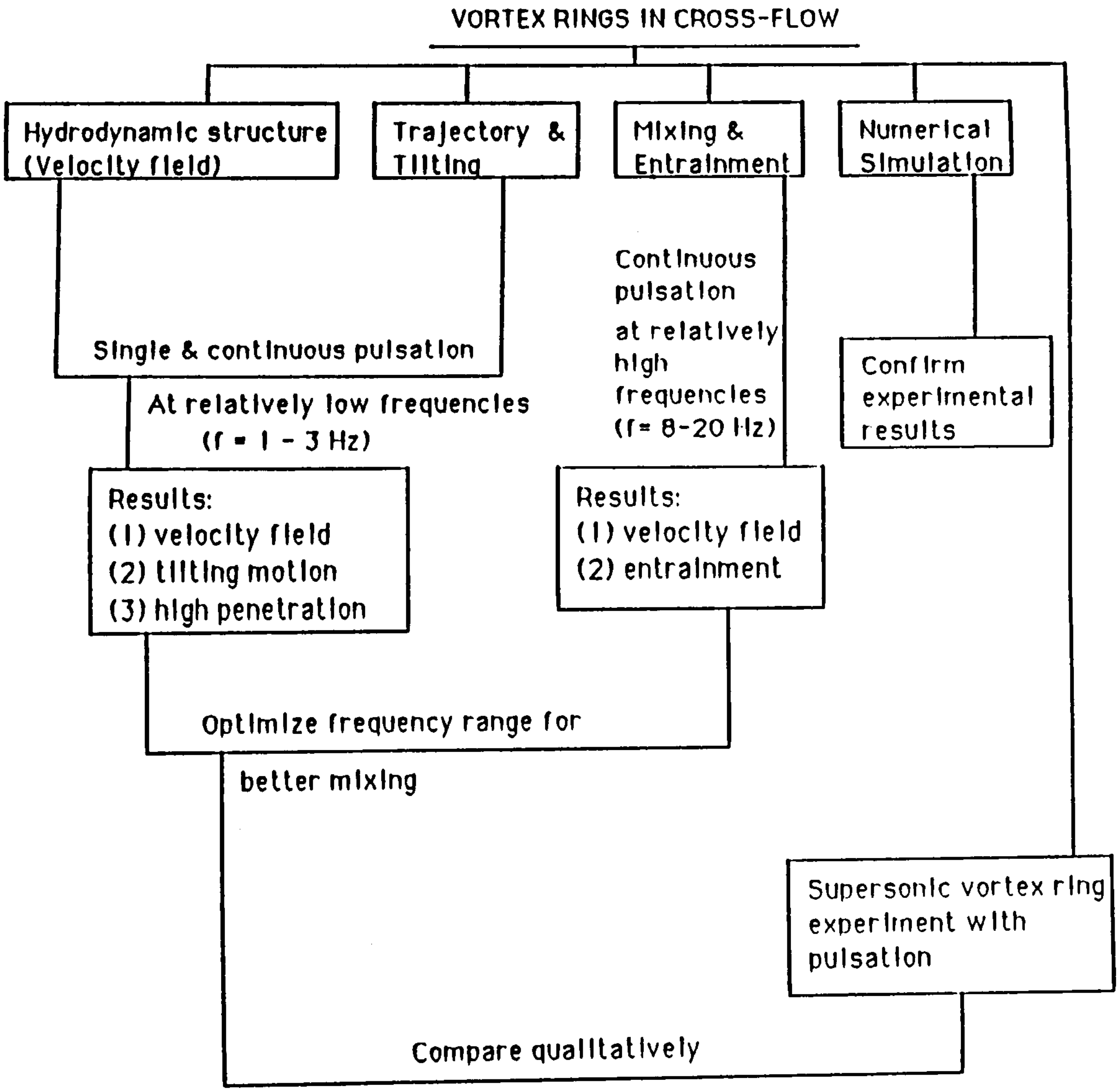

Figure 1.1 Research on vortex rings in cross-flow at UTSI

improvement in the supersonic cross-flow, using the present concept of transverse injection with pulsation, is being conducted at UTSI. The results of the present study will be used to guide this supersonic study. The research that the present study is directed towards will deal mainly with the ring structure at low frequencies in terms of motion and penetration.

1.4 Structure of This Study

The experimental, numerical and analytical investigations carried out in the present study are described in seven sections and two appendices of the dissertation as followings;

Section 2 focusses on the motion of vortex rings in uniform cross-flow, the theoretical predictions of vortex ring circulation, and some characteristic properties of vortex ring for both inviscid and viscous flows.

Section 3 presents the experimental setup for continuous and single pulsation, design of the vortex ring generator for single pulsation, flow visualization techniques, hot-film anemometry measurements and data acquisition procedures.

Section 4 describes some characteristics of vortex rings in cross-flow based on the results from flow visualization (dye technique) and laser-induced fluorescence technique for continuous and single pulsation. Mean velocity flow field measurements within vortex rings are analysed, including detailed quantitative data for characteristic parameters of the ring. Also, a dimensional analysis is discussed for vortex ring trajectories at different velocity ratio($\overline{U}_j/U_\infty$) and frequencies (f).

In Section 5, the details of numerical computation of vortex motion based on three-dimensional, Lagrangian, grid-free method will be discussed. The computational formulation, numerical scheme and calculation procedures are presented. The simulation of roll-up of shear layers into a vortex ring is modeled in a cross-flow by implementing viscous boundary condition on the wall. The vortex sheet method is applied to satisfy the no-slip boundary condition at the solid boundary.

In Section 6, the numerical results are described in terms of the effects of certain parameters (frequency of pulsation, ring circulation and cross-flow) on the trajectory and motion of vortex ring. The uniform potential, uniform shear and exponential-type velocity profiles are adopted for the study of various cross-flow effect. The tilting motion of vortex ring are compared for experiment and numerical model at low frequencies, without mutual interactions.

Section 7 presents the conclusions and recommendations of the present study for further extension of the research program.

Appendix *A* discusses a hot-film probe calibration and some results.

Appendix *B* identifies the sources and magnitudes of the uncertainties of the experimental measurements in terms of the various experimental techniques used in this study.

2. Analysis

2.1 Tilting Motion of Vortex Rings in Cross-Flow

Vortex rings can be produced by ejecting puffs of fluid through an opening. For the purpose of this study, vortex rings were created by either of two techniques; pulsing a flow using a frequency generator or a sudden motion of a piston in a cylinder whose exit was in the plane of a wall of a water tunnel. The vortex rings produced in this manner move as unit blobs and tilt into a cross-flow up to the free surface of the water tunnel. The motion of a typical ring may be analyzed qualitatively using the analogy with a solid body rotation of a circular cylinder. An estimate of the forces acting on the ring can be determined based on the quantitative measurements obtained from experimental observations. Depending on the pulsation frequency or piston velocity, circulation, size and translational velocity of the rings are different. Therefore, for each pulsation frequency or piston velocity the vortex ring will be affected by different range of flow variables. To explain the physical mechanism for the vortex ring motion in a cross-flow, forces acting on the bulk of the ring fluid may be identified and calculated using the above analogy. Since we assume a solid body approximation, the procedure is a simplified engineering approach as a first order of analysis to provide qualitative physical explanation for the ring motion observed.

Pulsation of the jet ejected out into a uniform cross-flow results in a train of individual vortex rings which are set apart from each other. At low frequencies they are assumed to be noninterfering: therefore, each vortex ring may be analyzed individually. Ting & Tung (1965) used a spinning solid cylinder as a model for the dynamics of a fluid vortex core with uniform vorticity. They also used the Kutta–Joukowski theorem to calculate the forces on the vortex core. However, Caruthers (1991, private communication) has suggested a Rankine vortex model is kinematically inconsistent with the Kutta–Joukowski result and that a singular layer of vorticity on the surface of the circular cylinder should be added to the model in this case. Superimposing a constant vorticity within the cylinder (Rankine vortex) serves to transport the surface layer vorticity as a solid cylinder rotation of the initial distribution and its potential field. He suggested that the implied lift on the fluid within the circular cylinder obtained based on this assumption was only one half of the Kutta–Joukowski result for a solid body. On the other hand, Moulden (1991, private communication) has considered a different tilting mechanism of vortex rings in cross-flow. He suggested that the rearward segment of the ring must pass through the wake (see Figure 4.1) and so experience a larger vertical velocity component than the forward segment. Therefore, the ring will tilt. Even though there still exists a controversy about the tilting mechanism, the model of Ting & Tung will be used for this analysis of the tilting motion of the vortex ring in uniform cross-flow with the realization that the actual forces depend on the details of the actual core and layer vorticity distribution.

Figure 2.1 illustrates lift and drag forces acting on a spinning cylinder. Each segment of the vortex ring can be considered as if it were a segment of a circular spinning solid cylinder. The forces acting on the ring at any instance can be estimated by considering the circulation of the ring on an equivalent solid body and the cross-flow in a coordinate system moving with the vortex, as shown in Figure 2.2. The Kutta–Joukowski theorem can be used to determine the force normal to the resultant flow on the incremental segments of the ring. Since the ring is like a torus, there is a frontal segment in the uniform cross-flow as shown by the resultant velocity vector U_{R_1}, Figure 2.1.

Since the freestream flow is assumed to be a uniform cross-flow, the movement

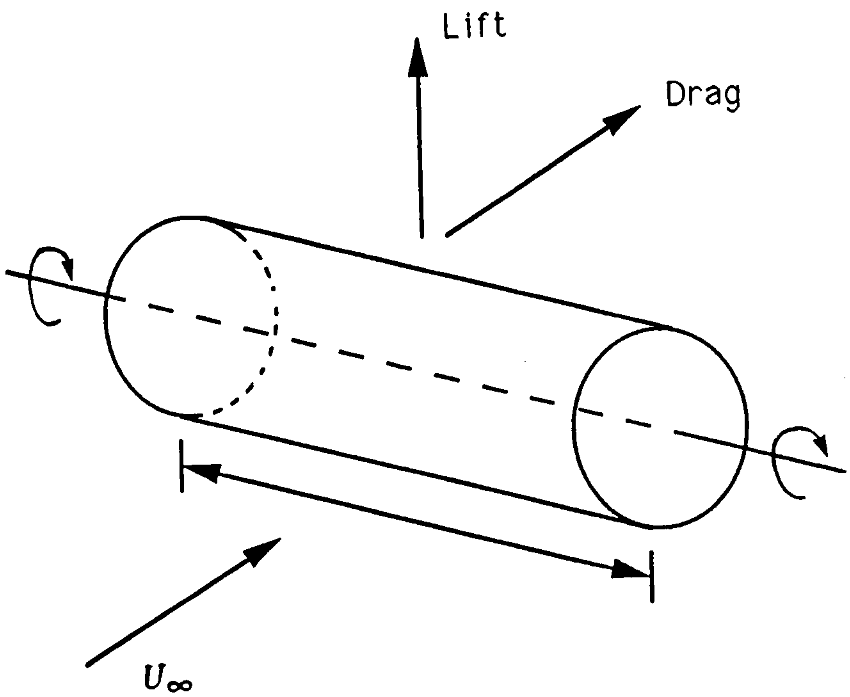

Figure 2.1 Lift and drag forces acting on a spinning cylinder

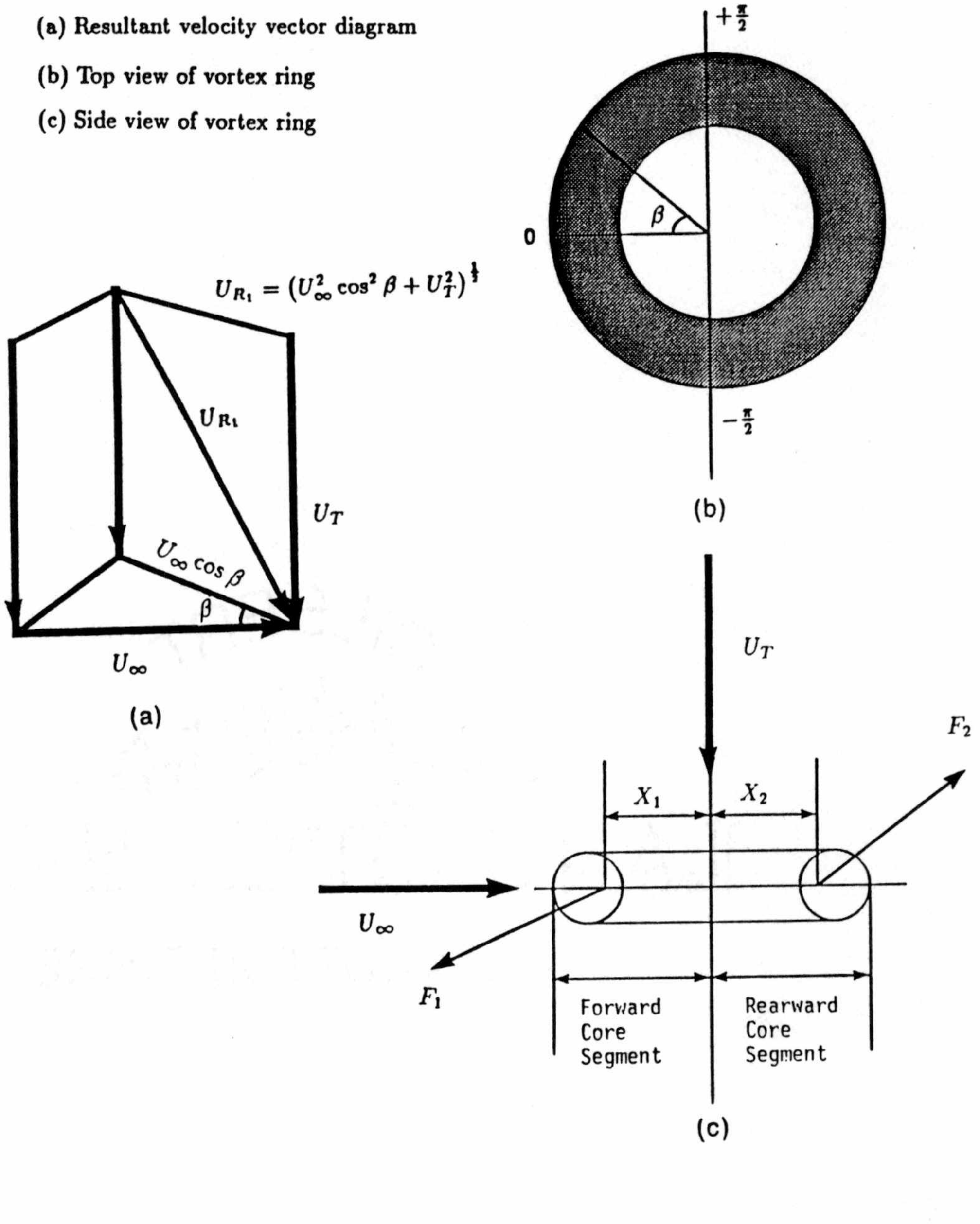

Figure 2.2 Notation for the simplified analysis of instantaneous instantaneous forces acting on the vortex ring in a frame moving with ring

of a vortex ring does not induce any variation in the vorticity distribution of the cross-flow and therefore, it does not affect the freestream flow. For this reason, the flowfield can be represented as the simple superposition of the steady cross-flow and that induced by the moving vortex rings. The schematic simulation for the motion of a vortex ring interacting with a uniform cross-flow is presented in Figure 2.2. The resultant velocity magnitude U_{R_1} on the forward section of the ring is given from Figure 2.2.

$$U_{R_1} = (U_\infty^2 \cos^2\beta + U_T^2)^{\frac{1}{2}}$$

where U_T is the magnitude of the translational velocity of the ring in the vertical direction and U_∞ is the magnitude of the uniform cross-flow velocity. For the forward portion of the vortex ring; force on an element is:

$$dF_1 = \rho U_T \Gamma R \left[\left(\frac{U_\infty}{U_T}\right)^2 \cos^2\beta + 1\right]^{\frac{1}{2}} d\beta$$

where β is the angle between uniform flow and the local segment of the ring in the plane of the ring, Figure 2.2. Total force is obtained by integration along the forward segment of the ring from $-\pi/2$ to $+\pi/2$.

$$F_1 = \rho U_T \Gamma R \int_{-\frac{\pi}{2}}^{\frac{\pi}{2}} \left[\left(\frac{U_\infty}{U_T}\right)^2 \cos^2\beta + 1\right]^{\frac{1}{2}} d\beta \qquad (2-1)$$

We can rewrite this as:

$$F_1 = B_1 \rho U_T \Gamma R$$

where

$$B_1 = \int_{-\frac{\pi}{2}}^{\frac{\pi}{2}} \left[\left(\frac{U_\infty}{U_T}\right)^2 \cos^2\beta + 1\right]^{\frac{1}{2}} d\beta$$
$$\equiv f\left(\frac{U_\infty}{U_T}, \beta\right)$$

where Γ is the circulation in the vortex ring of radius R. The rest of the ring is in an interfering flow field which is not readily known. In order to avoid accounting for the level of interference, a reducing coefficient K is introduced for the calculation of force on the rearward segment of the ring. For the rearward portion of the vortex ring, we cannot anticipate the resultant velocity vector being the same as before; except that for this case the leading portion provides some interference and we may select an effective resultant velocity. If we denote $K < 1$ as the reducing coefficient, then we can incorporate the interference effect in the evaluation of the force as follows:

$$dF_2 = \rho U_T \Gamma R \left[\left(K \frac{U_\infty}{U_T} \right)^2 \cos^2 \beta + 1 \right]^{\frac{1}{2}} d\beta.$$

Total force is calculated by integration along the rearward segment of the ring from $\pi/2$ to $3\pi/2$, Figure 2.2.

$$F_2 = \rho U_T \Gamma R \int_{\frac{\pi}{2}}^{3\frac{\pi}{2}} \left[\left(K \frac{U_\infty}{U_T} \right)^2 \cos^2 \beta + 1 \right]^{\frac{1}{2}} d\beta \qquad (2-2)$$

$$= B_2 \rho U_T \Gamma R$$

where

$$B_2 = \int_{\frac{\pi}{2}}^{3\frac{\pi}{2}} \left[\left(K \frac{U_\infty}{U_T} \right)^2 \cos^2 \beta + 1 \right]^{\frac{1}{2}} d\beta$$

$$\equiv f \left(\frac{U_\infty}{U_T}, K, \beta \right).$$

The locations X_1 and X_2, where the forces F_1 and F_2 are acting on, can be determined by a similar approach as above, resulting in:

$$X_1 = R\frac{\displaystyle\int_{-\frac{\pi}{2}}^{\frac{\pi}{2}} \cos\beta \left[\left(\frac{U_\infty}{U_T}\right)^2 \cos^2\beta + 1\right]^{\frac{1}{2}} d\beta}{\displaystyle\int_{-\frac{\pi}{2}}^{\frac{\pi}{2}} \left[\left(\frac{U_\infty}{U_T}\right)^2 \cos^2\beta + 1\right]^{\frac{1}{2}} d\beta} \qquad (2-3)$$

and

$$X_2 = R\frac{\displaystyle\int_{\frac{\pi}{2}}^{3\frac{\pi}{2}} \cos\beta \left[\left(K\frac{U_\infty}{U_T}\right)^2 \cos^2\beta + 1\right]^{\frac{1}{2}} d\beta}{\displaystyle\int_{\frac{\pi}{2}}^{3\frac{\pi}{2}} \left[\left(K\frac{U_\infty}{U_T}\right)^2 \cos^2\beta + 1\right]^{\frac{1}{2}} d\beta} \qquad (2-4)$$

where X_1 and X_2 are measured from the geometric center of the ring in the upstream and the downstream directions, respectively. It is obvious that as a result of the forces F_1 and F_2, there will be a moment applied on the ring. This moment changes as the orientation of the ring changes during its travel from the point of formation until it reaches the tunnel ceiling as it moves downstream. Video pictures and still photographs reveal that the orientation of the plane of the ring becomes inclined to the freestream as the ring leaves the jet orifice in a short time and short distance, as shown in the corresponding Figure 2.2. The ring moves into the cross-flow at an almost constant tilting angle. The initial turning is primarily due to the moment produced by the forces F_1 and F_2. As the ring rotates into the upstream the moment is significantly reduced. Hence, the ring can penetrate further without apparent additional rotation. This tilting of the ring keeps it rising, instead of reaching a maximum height in the cross-flow, as would a continuous jet. As a result of the induced velocity its penetration is significantly higher. From trajectory and the tilting of the vortex rings which are seen in flow visualizations, and the detailed velocity flowfield within the vortex ring, the value of reducing coefficient K can be identified by comparison of the calculated and observed results. The reducing coefficient K can be simply estimated from the velocity field measurements within the vortex ring such as Figure 4.11 (e) in Section 4. Since the average U-velocity component inside the ring is approximately 0.76 U_∞, K is evaluated to be about 0.76 inside the ring.

2.2 Properties of Vortex Rings

In this section, some properties of the vortex ring are considered. The basic parameters for vortex ring study are the circulation Γ, the translational velocity U_T, the ring diameter D and the core diameter $2a$. These important parameters are related to each other and determine the characteristics of a specific vortex rings. Inviscid classical and real viscous vortex ring theory will be described here.

2.2.1 Classical Vortex Ring

Lamb (1932) gives the following equations for inviscid vortex ring by assuming that the ratio of ring radius to core radius, R/a, is large.

$$U_T = \frac{\Gamma}{4\pi R}\left\{ln\left(\frac{8R}{a}\right) - \frac{1}{4}\right\} \qquad (2-5)$$

$$E = \frac{\Gamma^2 R\rho}{2}\left\{ln\left(\frac{8R}{a}\right) - \frac{7}{4}\right\} \qquad (2-6)$$

$$I = \pi\rho\Gamma R^2 \qquad (2-7)$$

where E represents the kinetic energy and I the linear momentum. The order of error is given by $o[a/R]$. This formula were extended by Fraenkel (1970, 1972), and Saffman (1975) to an arbitrary distribution of vorticity in the core.

$$U_T = \frac{\Gamma}{4\pi R}\left\{ln\left(\frac{8R}{a}\right) - \frac{1}{2} + A\right\} \qquad (2-8)$$

$$E = \frac{\Gamma^2 R\rho}{2}\left\{ln\left(\frac{8R}{a}\right) - 2 + A\right\} \qquad (2-9)$$

$$I = \pi\rho\Gamma R^2 \qquad (2-7)$$

where A is a constant which depends on the internal vorticity distribution. Saffman (1975) suggested A in the following form.

$$A = \int_0^a [\frac{\Gamma(s)}{\Gamma}]^2 \frac{ds}{s} \qquad (2-10)$$

The order of error in these expressions is $O[(a/R)^2 \cdot ln(R/a)]$. The expressions still hold when the vorticity in the core is diffused by viscosity.

2.2.2 Viscous Vortex Ring

As the vortex ring translates through the ambient flow, the vorticity diffuses from the core region and small amounts of ambient flow are entrained into the rear portion of the ring, mixing with the fluid exterior to the core. Subsequently, vorticity is convected into a wake region as shown in experiments conducted in this dissertation by some injected dye, resulting in a more lightly colored outer region compared to the core. The loss of vorticity from the vortex ring results in a decrease in ring circulation and, therefore, a decrease in translational velocity U_T with time.

Viscous diffusion of vorticity mainly dominates the vortex ring evolution at low Reynolds number. Tung and Ting(1967) derived an expression for the translational velocity of a thin core of viscous, rotational fluid embedded in a potential flow by using a matched asymptotic method.

$$U_T = \frac{\Gamma}{4\pi R}\left\{ ln\left(\frac{8R}{(4\nu t)^{0.5}}\right) - 0.558\right\} \qquad (2-11)$$

Equation (2–11) shows that the core radius grows due to viscous diffusion proportional to $(\nu t)^{0.5}$ and the translational velocity decrease as $-ln(\nu t)$. The ring strength is decreased as the core grows. Assuming the impulse remains constant, there is a slight increase in ring radius. Generally, viscous vortex rings in a real fluid have thick cores and measurements show a rate of decrease in velocity and increase in radius somewhere between that predicted by the extremely thin ($R/a \geq 10$) and thick core ($R/a \leq 3$) models.

2.3 Evaluation of Ring Circulation

It is one of the difficult problem of studying vortex ring dynamics and kinematics to accurately determine the circulation in the vortex ring since the velocity field should be instantaneously evaluated.

Once the translational velocity, the core and ring diameter are known, an estimate for the ring circulation can be obtained from the classical Kelvin formula (equation (2–5)). But, there are two difficulties to the estimation of the vortex ring circulation. One is to determine the correct core diameter, the other is related to the accuracy of equation (2–5) for real vortex rings, especially when some of the assumptions used for the derivation of this relationship may not be valid.

Before discussing how to measure the circulation, it is important to theoretically predict the initial circulation based upon the vorticity within the boundary layer at the jet orifice during the formation of each ring. The magnitude of ring circulation depends upon the amount of vorticity generated in the boundary layer, which means that the exit velocity and volume of ejected fluid influence the ring strength. These different features of the vortex ring depend on the mechanical system used to form it. For example, Taylor (1953) considered a vortex ring formed by giving an impulse to a circular disc and then dissolving it away. He determined the following relationships of parameters between the vortex ring and disc by equating the energy and momentum of the motion produced by the disc with those of a circular vortex ring.

$$U_T = 0.436 \cdot V \tag{2-12}$$

$$R = 0.816 \cdot c \tag{2-13}$$

where U_T and V represent the vortex ring and disc velocities, and R and c are the ring radius and disc radius, respectively. Since the rolling up of the vortex sheet does not change the circulation around the core, the circulation (Γ) around the ring is supposed to be the same as that around a circuit passing through the center of the disc, i.e.,

$$\Gamma = \frac{4Vc}{\pi} \tag{2-14}$$

By using equations (2–12) and (2–13), it can be rewritten as

$$\Gamma = 3.58 \cdot U_T R \tag{2-15}$$

The radius ratio between ring and core (R/a) can be obtained comparing equations (2–5) and (2–15). So that Taylor's theory gives

$$\frac{R}{a} = 5.38 \tag{2-16}$$

As mentioned before, two methods were adopted in the present study to produce vortex rings; one method used a piston-cylinder assembly, which is most commonly used for a single pulsation, the other method used a combination of a frequency generator and a solenoid valve for a continuous pulsation. A cylindrical vortex sheet is formed initially for both cases which then rolls up into a vortex ring. Energy and momentum are assumed to be conserved during roll-up and used to determine the velocity and size of the vortex ring.

2.3.1 Estimate of Initial Ring Circulation by Piston Movement

The prediction of the initial circulation in a vortex ring generated by a pulsed, piston-cylinder assembly, can be estimated based on a uniform cylindrical-slug model. For the movement of a piston of diameter D_p in a cylinder with a straight walled tube, the piston stroke can be defined as

$$L_p = \int_0^{T_p} U_p(t)dt = \overline{U}_p T_p \qquad (2-17)$$

where $\overline{U}_p$ is a mean velocity with respect to time and expressed as

$$\overline{U}_p = \frac{\int_0^{T_p} U_p(t)dt}{T_p} \qquad (2-18)$$

where T_p is the piston movement or ring formation time, $U_p(t)$ is the piston velocity profile.

In a half plane through the axis of symmetry the vorticity flux rate from the edge of the exit has the magnitude $U_p{}^2/2$, so that the initial circulation for a straight walled tube becomes

$$\Gamma_i = \frac{\int_0^{T_p} U_p(t)^2 dt}{2} \qquad (2-19)$$

The initial circulation for sharp-edged orifice with exit diameter different from piston diameter can be estimated by the same way. (Refer to Figure 4.5)

$$\Gamma_i = \frac{\int_0^{T_p} U_e(t)^2 dt}{2} \qquad (2-20)$$

where $U_e(t)$ is the exit velocity profile. The mean exit velocity is expressed as

$$\overline{U}_e = \overline{U}_p \cdot \frac{D_p}{D_e}^2$$

By assuming the constant velocity across the exit plane, the circulation can be simplified for a straight tube as

$$\Gamma_i = \frac{1}{2}\overline{U}_p{}^2 T_p = \frac{1}{2}\overline{U}_p L_p \qquad (2-21)$$

For a sharp-edged orifice,

$$\Gamma_i = \frac{1}{2}\overline{U}_e{}^2 T_p = \frac{1}{2}\overline{U}_p{}^2 \frac{D_p{}^2}{D_e} T_p \tag{2-22}$$

2.3.2 Estimate of Initial Ring Circulation by Frequency Generator

In this case, the vortex rings are produced by pulsating the continuous jet flow periodically. The prediction of initial circulation, therefore, can be made by assuming fully-developed flow in the pipe. The transverse velocity profile at the jet exit was measured, and found to have a form of a flat top with a boundary layer of thickness $\delta = 0.15R$ (R is an exit radius) at each frequency (below 10 Hz) for this study. The slug length corresponding to the piston stroke L_p in the piston experiment can be written

$$L_s = \overline{u} \cdot \frac{1}{f} \tag{2-23}$$

where

$$\overline{u} = \frac{4\dot{Q}}{\pi D_e{}^2} \tag{2-24}$$

where $\overline{u}$ is a mean velocity, $\dot{Q}$ is the mean flow rate, D_e is the exit diameter of the jet and f is frequency of the pulsations.

By analogy with the analysis of single pulsation, the vorticity flux rate from the edge of the exit has the magnitudes $\overline{u}^2/2$, so that the initial circulation is

$$\Gamma_i = C \int_0^T \overline{u}(t)^2 dt \tag{2-25}$$

or

$$\Gamma_i = \frac{1}{2} C \overline{u}^2 \frac{1}{f} \tag{2-26}$$

where T indicates the actual time taken during vortex ring formation.

Therefore,

$$\Gamma_i = 8C\left(\frac{\dot{Q}}{\pi D_e{}^2}\right)^2 \frac{1}{f} \tag{2-27}$$

where the mean flow rate $\dot{Q}$ is varied depending on pulsed frequency and found by integrating the velocity traces obtained from hot-film probe measurements with respect to area. C is the ratio of volume between vortex ring bubble and fluid actually ejected. It is seen that the initial circulation is dependent on the flow rate and frequency.

2.3.3 Comparisons of Circulation Measurements

Sallet and Widmayer (1974) calculated the total circulation Γ of vortex rings from the following relation,

$$\Gamma_c = (U_{max} - U_T)\pi d_c \tag{22-28}$$

where Γ_c is an effective core circulation which is different from the total circulation. d_c is the effective core diameter, defined as the distance between the points of maximum velocity on opposite sides of the ring, on a straight line intersecting the center of the vortex core. The relations between total circulation Γ and core circulation Γ_c and between d and d_c were estimated by resorting to the theory (Sallet and Widmayer, 1974). They compared their core model with the Hamel-Oseen solution of the viscous decay of a line vortex. It was found that the total circulation Γ and the solid body core diameter d are related to effective core circulation and effective core diameter as follows:

$$\Gamma_c = 0.715 \cdot \Gamma \tag{2-29}$$

and

$$d_c = \frac{d}{0.891} \tag{2-30}$$

The expression for translational velocity was given by

$$U_T = \frac{\Gamma_c}{4(0.715)\pi R}\left\{ln\left(\frac{8D}{0.891d_c}\right) - \frac{1}{2} + A\right\} \tag{2-31}$$

They determined that a value of $ln(2)$ for the constant, $A - 1/2$, gave good agreement between their predicted and measured translational velocities.

Didden (1979) attempted to determine vortex ring circulation from the flow condition at the nozzle. The circulation, which is derived from the boundary layer and rolls up into the vortex, was calculated by measuring the unsteady velocity field in the nozzle-exit plane during the rolling-up process of the ring using laser doppler velocimetry. The circulation of vortical fluid convected through the nozzle-exit plane was evaluated from these measurements. In addition to calculating the circulation in the region $x \geq 0$ (x is the downstream distance from the nozzle exit plane) by convective transport of vorticity through the plane $x = 0$ during the piston displacement, he also determined the circulation of the ring at a position $x = 3D_o$. The change of circulation $d\Gamma$ within the region $x \geq 0$ during the time interval dt is given by

$$d\Gamma = \int_F \omega dF \tag{2-32}$$

where the integration region F in the xy-plane contains all fluid that convects through the plane $x = 0$ during the interval dt. The vorticity flux is

$$\frac{d\Gamma}{dt} = \int_0^\infty \omega(x=0,y,t)\cdot u(x=0,y,t)dy \tag{2-33}$$

In order to evaluate equation (2–33) the vorticity flux through the exit plane at inside and outside nozzle should be considered separately:

$$\frac{d\Gamma}{dt} = \frac{d\Gamma_i}{dt} + \frac{d\Gamma_o}{dt} \tag{2-34}$$

The measured velocity profiles and equation (2–34) enable $d\Gamma/dt$ to be evaluated. Thus, the total circulation $\Gamma(t) = \Gamma_i + \Gamma_o$ of the fluid transported through the plane $x = 0$ results from integration of $d\Gamma/dt$. The important result in Didden's work is that he showed that the negative circulation produced at the outer wall is a significant and measurabe amount. He concluded that the following effects are essential for the vortex circulation which were not considered in the simplified slug model.

(i) The starting flow around the nozzle edge produces a large flow velocity $u \geq U_p$ near the edge, causing a large vorticity flux into the vortex ring, especially at small time t.

(ii) At larger t, the maximum velocity u_i in the exit cross-section remains larger than U_p because of the displacement effect of the boundary layer.

(iii) The net vorticity flux into the vortex ring is considerably diminished by the negative vorticity of the external boundary layer, which is produced by the flow of the rolling-up vortex at the outer nozzle wall.

Didden (1977) also published another paper which showed the determination of vortex circulation Γ_w by measuring the velocity $u(t, y = 0)$ and the translational velocity U_T of the vortex ring at a distance $x = 3D_o$ downstream from the nozzle. The circulation Γ_w within the closed curve C containing the vortex core (see Figure 2.3) is found by integrating the u-velocity along the x-axis and closing the curve C outside the x-axis at infinity,where u and v are zero:

$$\Gamma_w = \oint (udx + vdy) = \int_0^\infty u(x, y = 0)dx$$

$$= U_T \int_\infty^0 u(t, y = 0)dt \qquad (2-35)$$

The transformation $dx = U_T dt$ is valid, since the flow field of the vortex ring is approximately stationary in a vortex-fixed frame while it convects over the measuring point at $x = 3D_o$.

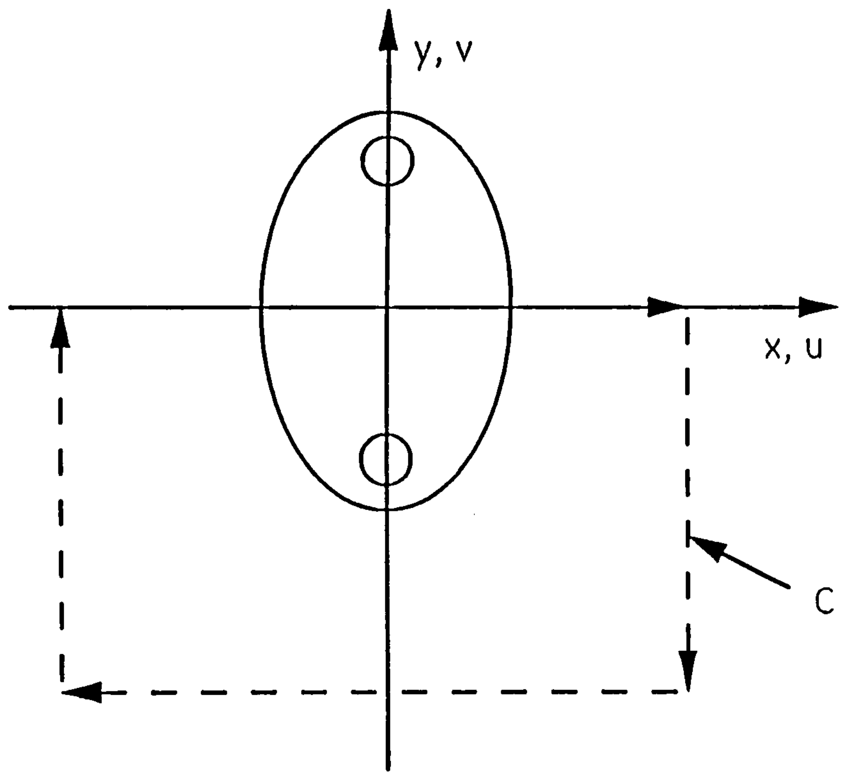

Figure 2.3 Integration curve for the determination of circulation

Sullivan et al. (1973) evaluated the circulation of vortex rings by two different methods. First, they calculated the circulation Γ from the line integral of the velocity for a path around and far outside of the core of the ring which is almost the same as Didden's work (1977). The second method was to calculate Γ from the vorticity distribution within the ring. These two calculations of circulation were within 3.4 % of each other. By numerically integrating their vorticity distribution, they obtained a value for A in the equation (2–8) of 0.136. This yields an $A - 1/2$ value of -0.364, which is contrast to Sallet and Widmayer's result of $ln(2)$.

Brasseur and Chang (1981) described a method in which kinematics is exploited to compute the total circulation of a vortex from relatively simple flow visualization experiments using potential flow theory. This method has one advantage that the total circulation is computed for an individual vortex at any point in its evolution. Other techniques, such as LDV and hot-wire anemometry, requires a repeatable production of vortices, precluding the possibility of calculating the strength of a single vortex as it evolves. The Biot-Savart law kinematically relates the velocity field to the vorticity field at each instant in time. The potential for a vortex filament loop of strength Γ can be derived from the Biot-Savart law

$$\phi(x) = \int\int \frac{\partial}{\partial n}\left(\frac{\Gamma}{4\pi r}\right) dA(\zeta) + \phi_i(x) \qquad (2-36)$$

where A is the surface bounded by the filament loop, $r = x - \zeta$ where ζ is the point at which the vorticity exists. ϕ_i is the potential field from the presence of the boundaries and must satisfy Laplace's equation, and therefore the potential field away from the vortex core is kinematically described by its strength and its geometrical orientation in the flow field. That is, from a knowledge of the potential field and the geometry of the vortex, it is possible to calculate the total circulation. Then from the size and shape of the bubble and the velocity of the vortex system, the total circulation of the vortex can be derived from the parameters which are related kinematically. They used a modified form of Kelvin's formula to determine the circulation of the ring.

$$U_T = \frac{\Gamma}{4\pi R}\left\{ln\left(\frac{8R}{a}\right) - \frac{1}{3}\right\} \qquad (2-37)$$

A different but less accurate comparison was also made to estimate the initial strengths of experimental vortex rings. They considered a slug of fluid of length L ejected from the orifice with velocity $U_e(z)$. The total circulation of this ejected fluid is given by

$$\Gamma_{ej} = \int_0^L U_e(z)dz \qquad (2-38)$$

Measuring the initial volume of the vortex bubble, the total circulation in a newly formed vortex ring (defined as the point where Γ peaks) can be estimated by multiplying Γ_{ej} by the ratio of bubble volume to the total volume of fluid ejected from the orifice. This method appears to be a simple method benefitting from the ease of flow visualization experiments. As the authors indicated, the calculation of circulation using this method should be compared to the results by LDV or hot-wire anemometry to fully evaluate the accuracy of their method. In the present study, the circulation value by this method will be compared with hot-film anemometry data.

Cerra and Smith (1983) utilized the hydrogen bubble technique to measure the velocity along a closed path around the core of a vortex ring. From the assumptions of classical theory for a vortex ring, the angular velocity $\dot{\theta}$ along a closed path at the edge and outside of the core was measured to determine the circulation. The mathematical expression for the circulation becomes

$$\Gamma = 2\pi a^2 \cdot \dot{\theta} \qquad (2-39)$$

Since $U_{rot} = a \cdot \dot{\theta}$, equation (2–39) can be written as

$$\Gamma = 2\pi a \cdot U_{rot} \qquad (2-40)$$

where a and $\dot{\theta}$ are the radius and angular velocity at the point of measurement with respect to the center of the core. U_{rot} indicates the rotational velocity at the measurement point. They used this method to determine the circulation. As Sallet and Widmayer (1974) indicated, this value represents the core circulation, not the total circulation. Thus their value was considered to underestimate the real circulation.

Also, the technique by Sallet and Widmayer (1974) is applied to calculate the effective core circulation and total circulation. Once the exact core center is known, the inner and outer edge of the core can be established. The velocity at the inner edge U_{ie} is the sum between rotational velocity U_{rot} and translational velocity U_T, and the outer edge velocity U_{oe} is the difference between U_{rot} and U_T. Therefore U_{rot} and U_T can be expressed as (Refer to Figure 4.9)

$$U_{rot} = \frac{1}{2}(U_{ie} + U_{oe}) \qquad (2-41)$$

$$U_T = \frac{1}{2}(U_{ie} - U_{oe}) \qquad (2-42)$$

The effective core circulation becomes

$$\Gamma_c = U_{rot} \cdot 2\pi a \qquad (2-43)$$

Sallet and Widmayer's theory, equations (2–29) and (2–30), was used to compare with total measured circulation obtained by integrating the velocity profiles in the present investigation.

In the study conducted in this dissertation, two different methods will be used to estimate the circulation of the vortex rings: (1) the initial ideal circulation by the simplified cylindrical-slug model and (2) integrating $\overline{W}$ velocity component obtained from hot-film measurements.

3. Experimental Apparatus and Procedures

As previously mentioned, two different techniques were used in the present study to generate the vortex rings in the cross-flow. One was to use a frequency generator with a solenoid valve for continuous jet pulsation. It was possible to investigate the effect of excitation on the motion of vortex rings by simply adjusting the range of frequency. On the contrary, there are some difficulties such as the good estimation of initial vortex strength in the jet pipe. In order to overcome this problem, the other device designed was based on a the piston-cylinder assembly which provided a discrete single pulsation. The piston-type facility has been the most popular way utilized by researchers to produce a single vortex ring. This study was conducted in the University of Tennessee Space Institute water tunnel which has excellent flow quality (Collins, 1982).

It is very difficult to accurately and quantitatively determine the circulation and core size of vortex rings because the velocity field on a vortex ring should be instantaneously evaluated. As reviewed in the Introduction, there have been several experimental methods developed to evaluate the vortex ring parameters such as ring diameter, translational velocity, circulation and core diameter. The ring diameter, core size and translational velocity are accurately evaluated using the following methods: flow visualization, hot-wire or hot-film anemometer, hydrogen bubble technique, and laser Doppler velocimeter. For the purpose of evaluating more accurate vortex ring parameters, a hot-film anemometry was adopted to support and complement the flow visualization techniques.

3.1 Description of Water Tunnel Facility

The schematic layout of the water tunnel facility is shown in Figure 3.1. The water tunnel is a closed-return type and is powered by a 25.4 *cm* diam-

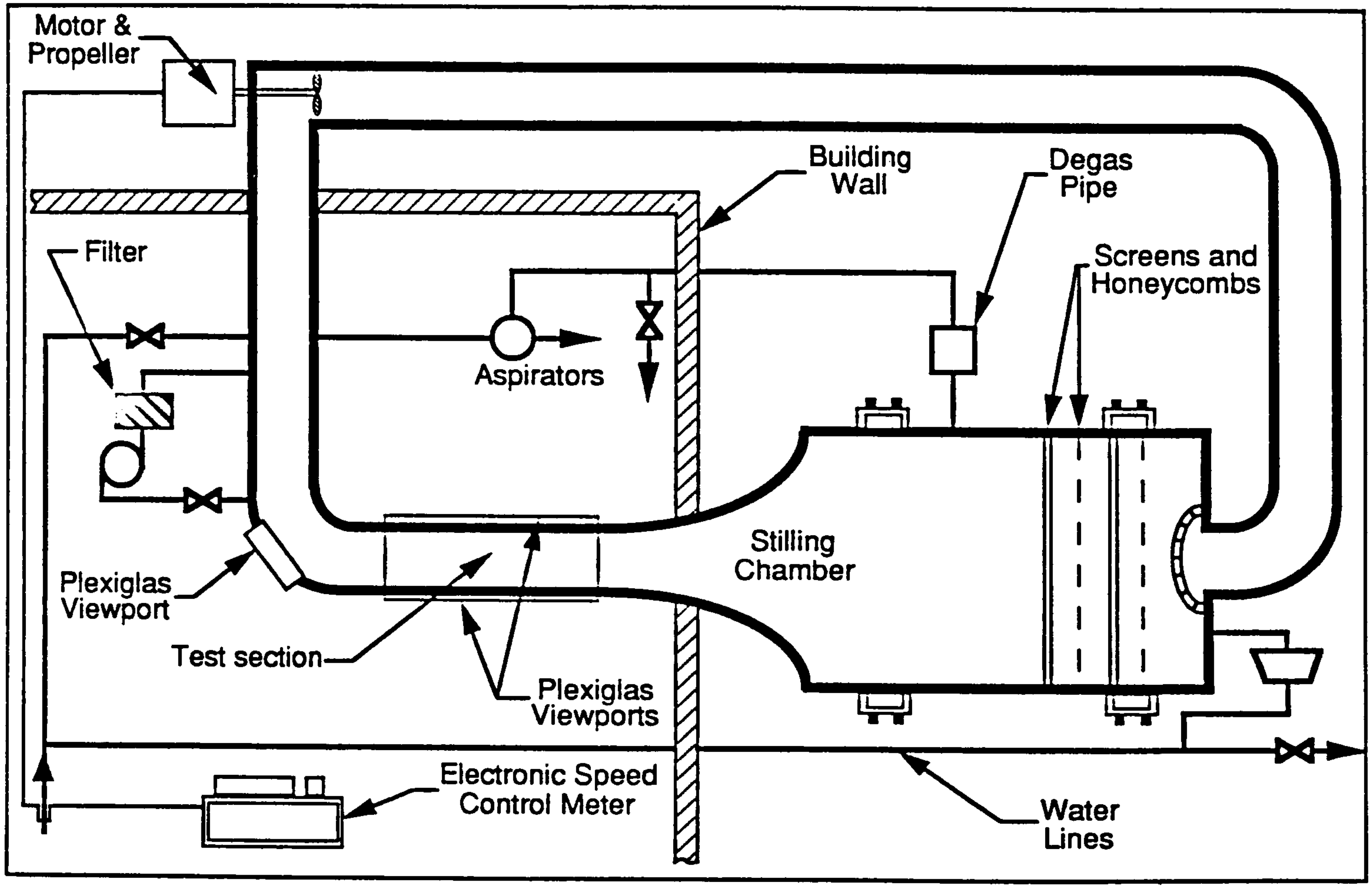

Figure 3.1 Schematic layout of water tunnel facility

eter two-bladed propeller which is connected to a one hp electric motor. The motor is mounted on a vibration-isolated foundation and is connected to a continuously variable speed transmission which allows the tunnel speed to be varied from 1.5 *cm/sec* to 60 *cm/sec*. This combination of motor and propeller is located at the second bend downstream of the test section. The fluctuations from the propeller are damped by the long return pipe connected to the stagnation chamber. Velocity fluctuations in the test section due to the propeller have been measured and extremely small. The dimensions of the test section are 30.5 *cm* high, 45.7 *cm* wide and 150 *cm* long (12 *in* x 18 *in* x 60 *in*). The test section walls are constructed of 0.5 *in* thick plexiglas for versatility in observing and photographing the flowfield. Also, these walls are designed to account for the growth of boundary layer at the freestream velocity of 15.2 *cm/sec*.

The stagnation (stilling) chamber is a cylindrical tank which has 150 *cm* diameter and 285 *cm* length. It contains four stainless steel screens and two aluminum honeycombs to reduce fluctuations. The length to diameter ratio of the honeycombs is 6. The turbulence intensity in the test section was designed to be 0.1%. The nozzle between the stagnation chamber and test section is a bell mouth type, which gradually and continuously changes from a circular to rectangular cross-section with a contraction ratio of 13.5. A filter is installed in the first downstream bend of the test section to maintain particle sizes less than 10 microns in the water.

The tunnel velocity field was calibrated by using a cylindrical hot-film probe to ensure uniform cross-flow. The probe was calibrated by using a specially constructed water channel (Appendix A). Then the calibrated probe was utilized to calibrate the water tunnel.

The tunnel is operated by a master control panel inside the building. The tunnel mean water speed is observed with a digital meter on the control panel that indicates the rotational shaft speed of the propeller.

3.2 Experimental Setup for Continuous Pulsation

Figure 3.2 shows the schematic of the experimental setup in the water tunnel. The jet was installed on a false floor of the test section which provided a known boundary layer at the jet location. The false floor was a surface-finished plate with an elliptic leading edge and it was located 19 mm above the tunnel floor and was 1500 mm long. The jet exit ($d_j = 12.7$ mm) was located 190 mm behind the leading edge. This allowed the laminar boundary layer thickness at the jet to be of the order of one jet diameter. The Reynolds number based on the jet diameter and steady jet velocity was $Re_{d_j} = 1.87 \times 10^3$. The tunnel floor and one side wall were marked with lines spaced at equal distance to be used with the flow visualization data collection of vortex rings size and trajectories.

Pulsation of the full jet flow was accomplished by incorporating a solenoid valve in-line in the jet water supply tube. This valve was driven by a frequency generator so that any frequency pulsation could be investigated. The valve did not respond uniformly at frequencies of 20 Hz and above. The solenoid valve was approximately 20 diameters upstream of the jet exit. This ensured a uniform pipe flow at the jet exit.

The motion of vortex rings was studied for several different area-averaged jet exit velocity to cross-flow velocity ratios, $\overline{U}_j/U_\infty \simeq 1.5$ to 6.7. The jet equivalent velocity was 14.88 *cm/sec* which is a velocity without pulsation in the pipe. Since the pulsed jet penetrated deep into the cross-flow at the low jet flow rate of 18.85 cm^3/sec (0.3 *GPM*), the variations in $\overline{U}_j/U_\infty$ were obtained by the changes

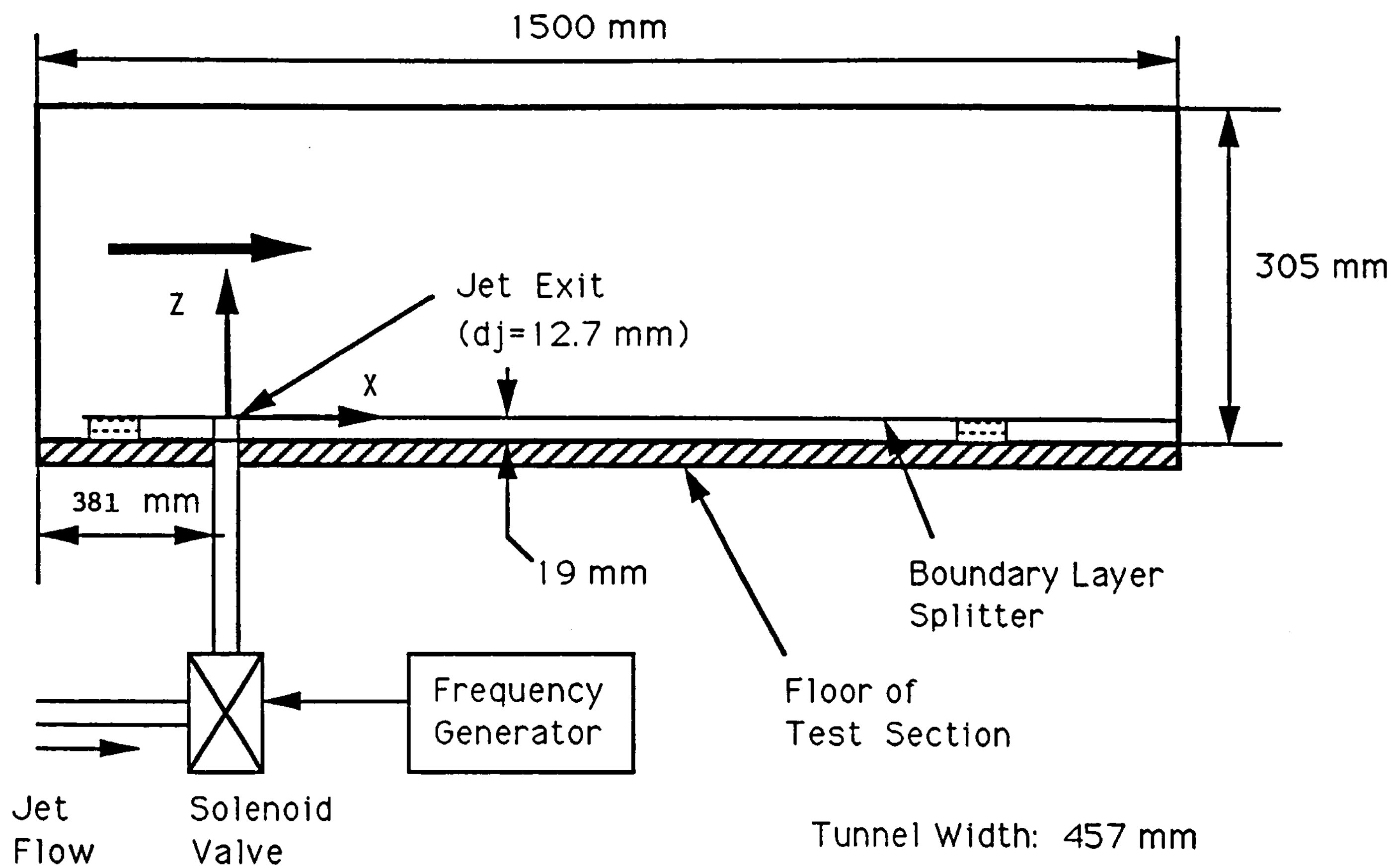

Figure 3.2 Experimental setup of water tunnel for continuous pulsation

in the cross-flow velocity U_∞. The jet equivalent velocity in the pipe should be distinguished from the jet exit velocity ($\overline{U}_e$) caused by the pulsation in the same pipe. This jet exit velocity was close to the initial translational velocity of the vortex ring. Figure 3.3 illustrates the exit velocity profiles with flat hat-top configuration at pulse frequencies 1 Hz and 3 Hz.

Typical velocity (voltage) traces, at the jet exit, for different frequencies are presented in Figure 3.4 for continuous and discrete pulsations. The velocity trace characteristics determine actual vortex ring formation in the same way as the piston velocity in a single pulse has considerable effect. In the continuous pulsation, as the frequency is increased the maximum velocity(impulse) is considerably reduced. This means that at high frequencies the circulation of the ring is considerably decreased with maintaining steady flow rate. The effects of piston velocity profile in single pulsation will be discussed in the next section. A theoretical, continuously pulsed velocity profile should be a square wave.

3.3 Experimental Setup for Single Pulsation

A schematic of the experimental setup and test section dimension is illustrated in Figure 3.5. The vortex ring generator was installed just below the floor of the test section. It consisted of a piston/cylinder assembly, an air cylinder and a potentiometer. The details of the geometry of the vortex ring generator will be described in the next section. The jet exit (d_j = 12.7 mm) was located on the centerline 190 mm from the leading edge of the test section (381 mm from the entrance of the test section). The jet issued perpendicular to both the floor and the cross-flow. Transparent plexiglas was used on the front side wall of the test section for observation.

The motion and trajectory of the vortex rings were studied at several differ-

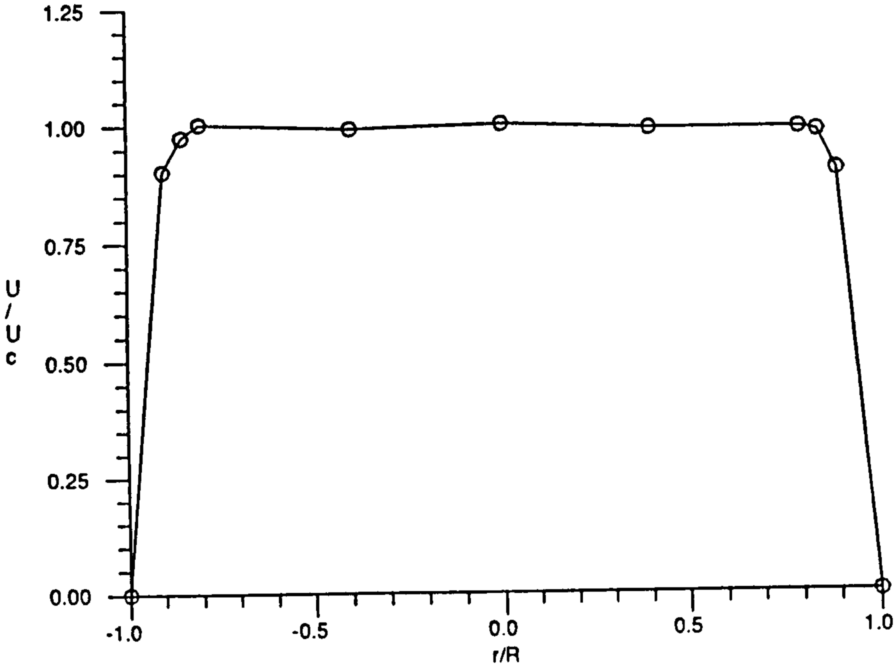

(a) Exit velocity profile at $f = 1Hz$

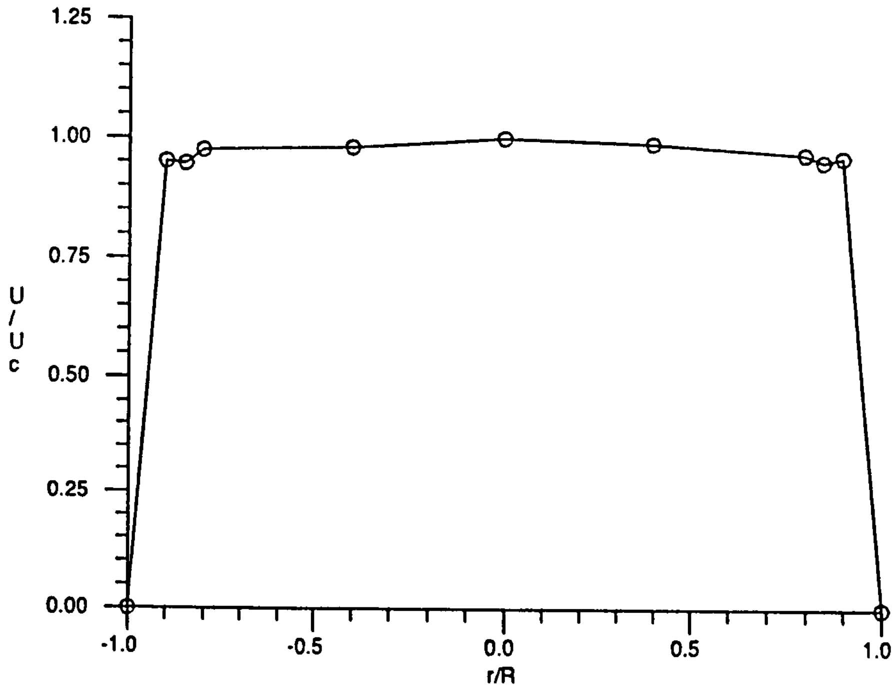

(b) Exit velocity profile at $f = 3Hz$

Figure 3.3 Exit velocity profiles at different frequencies

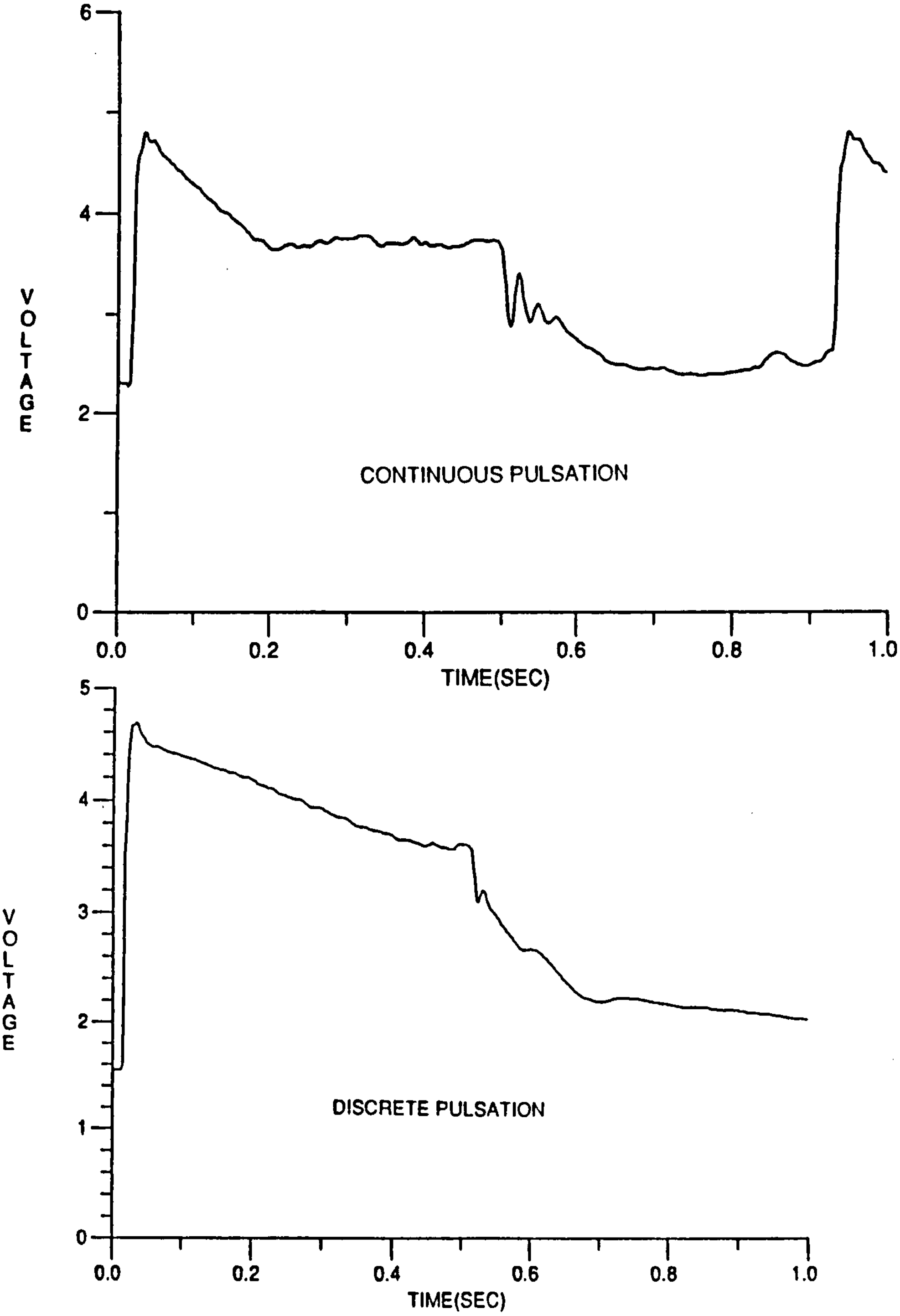

(a) 1 Hz

Figure 3.4 Typical pulsation profiles at the exit

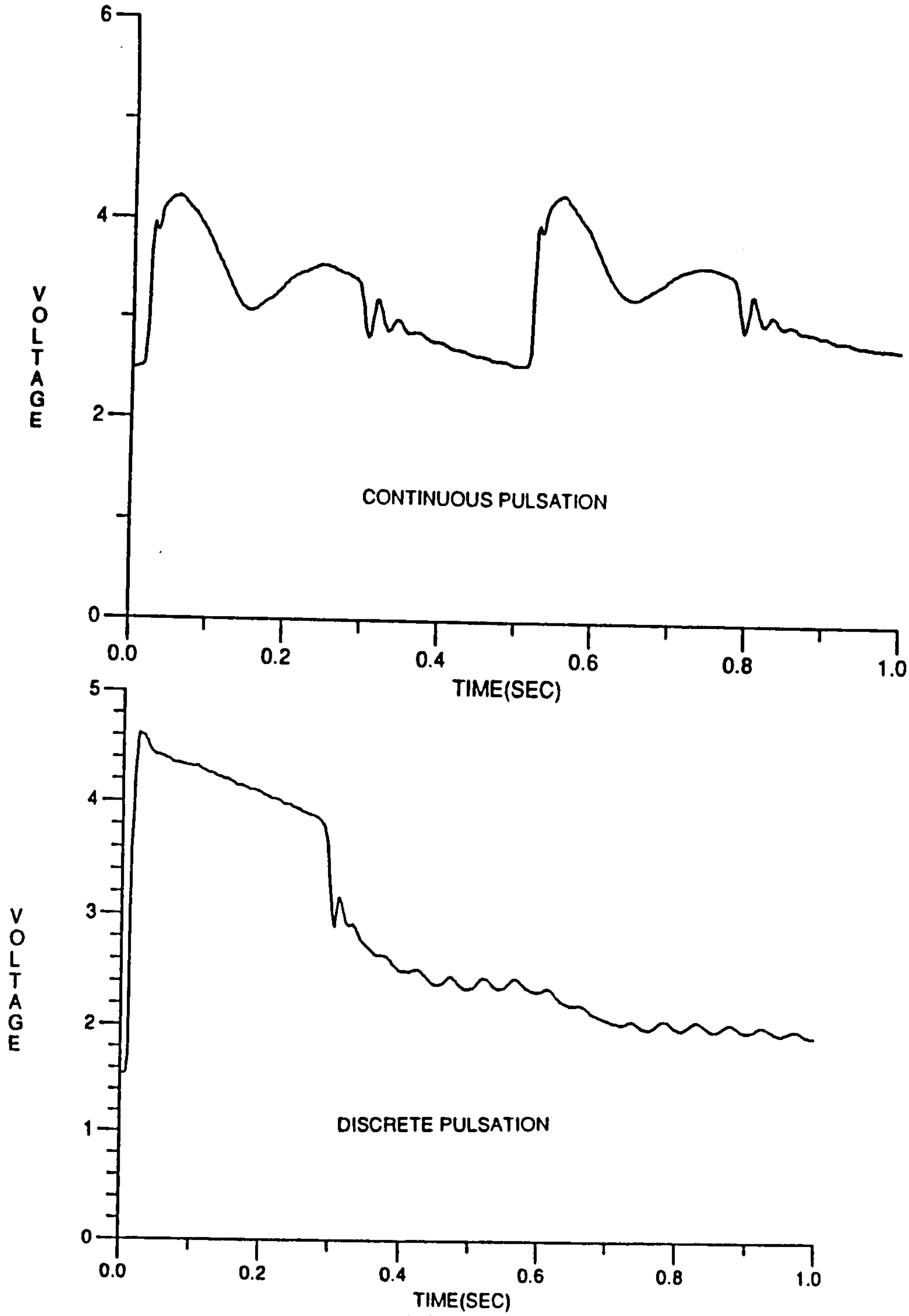

(b) 2 Hz

Figure 3.4 Continued

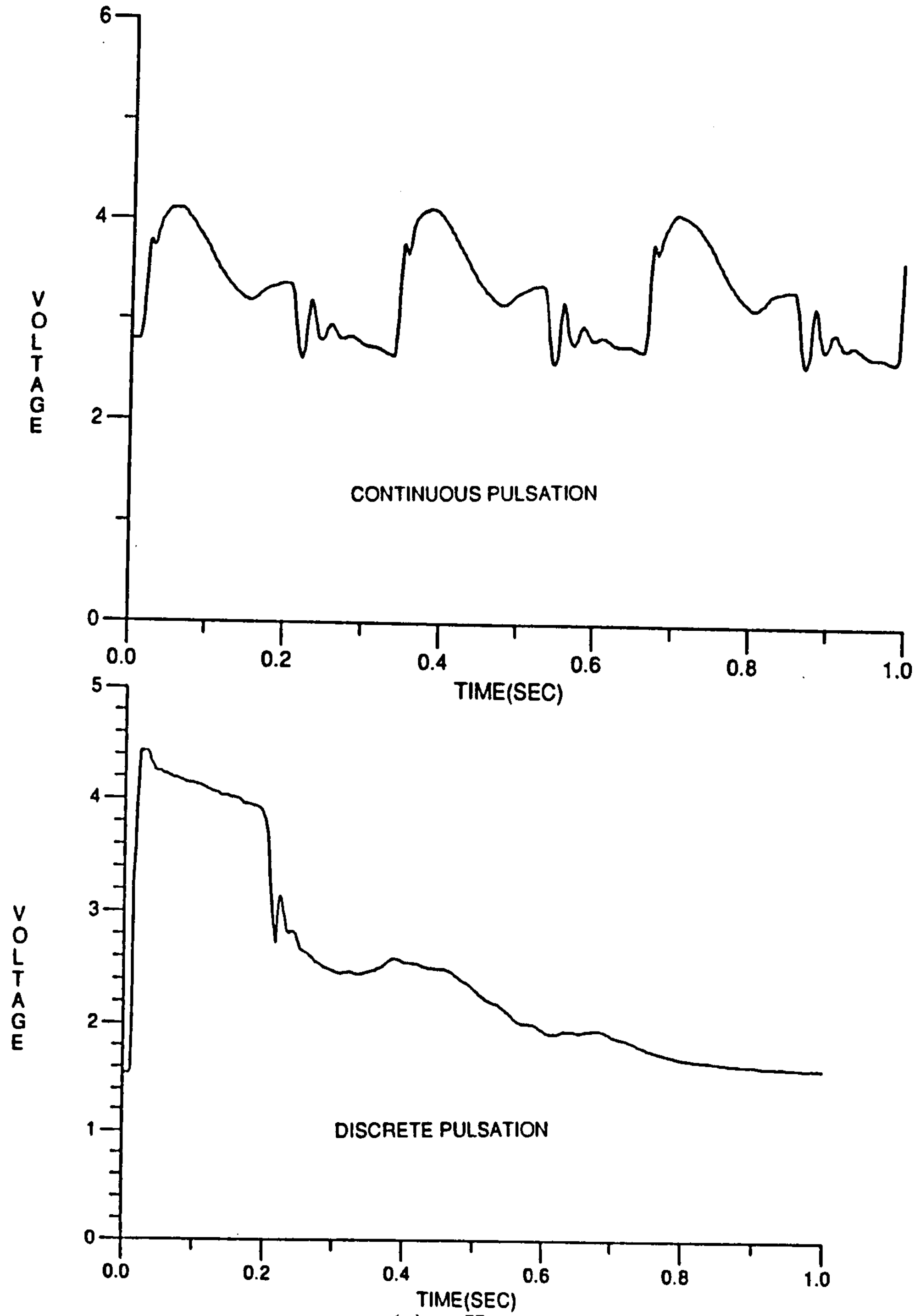

(c) 3 Hz

Figure 3.4 Continued

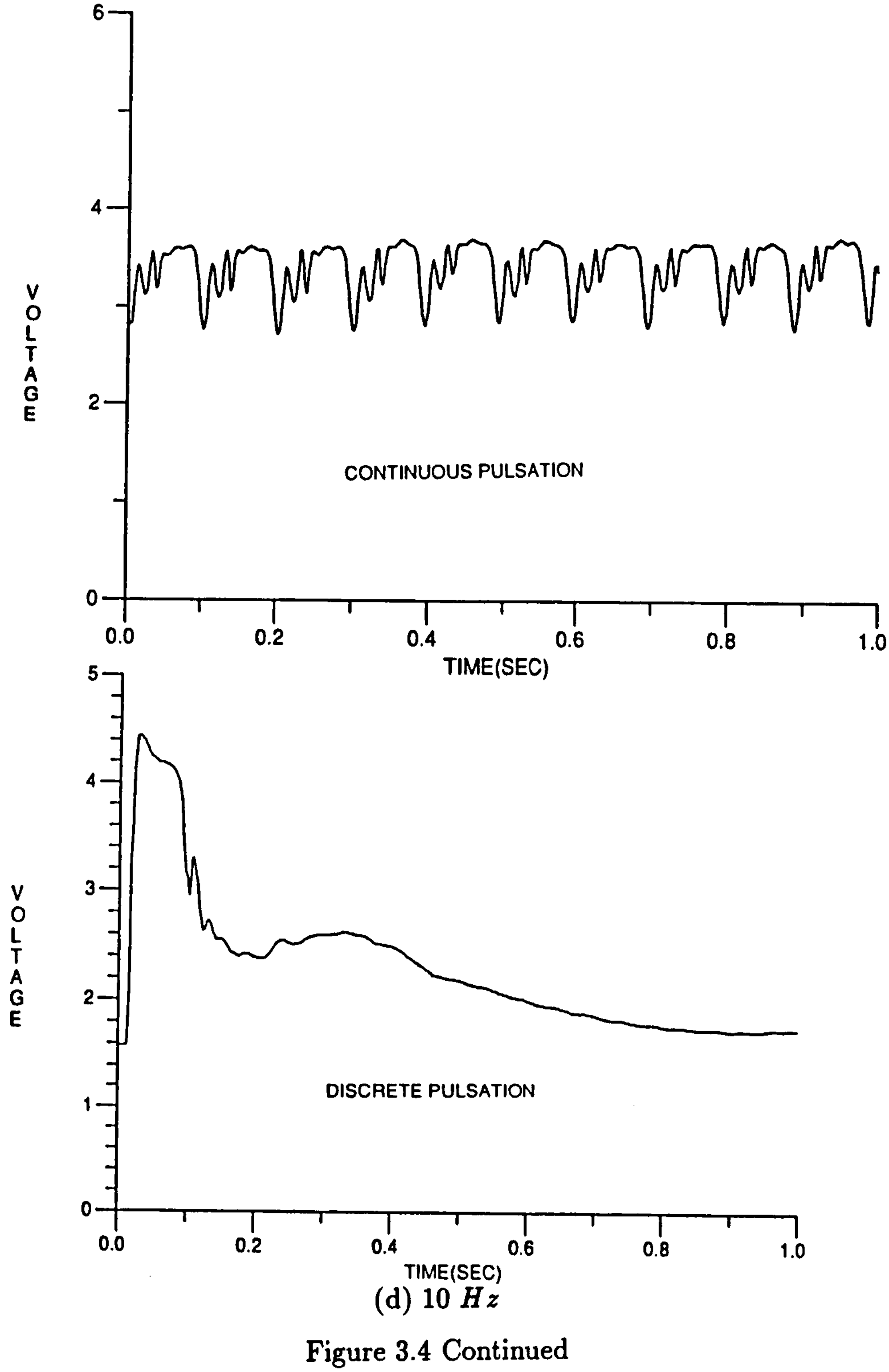

(d) 10 Hz

Figure 3.4 Continued

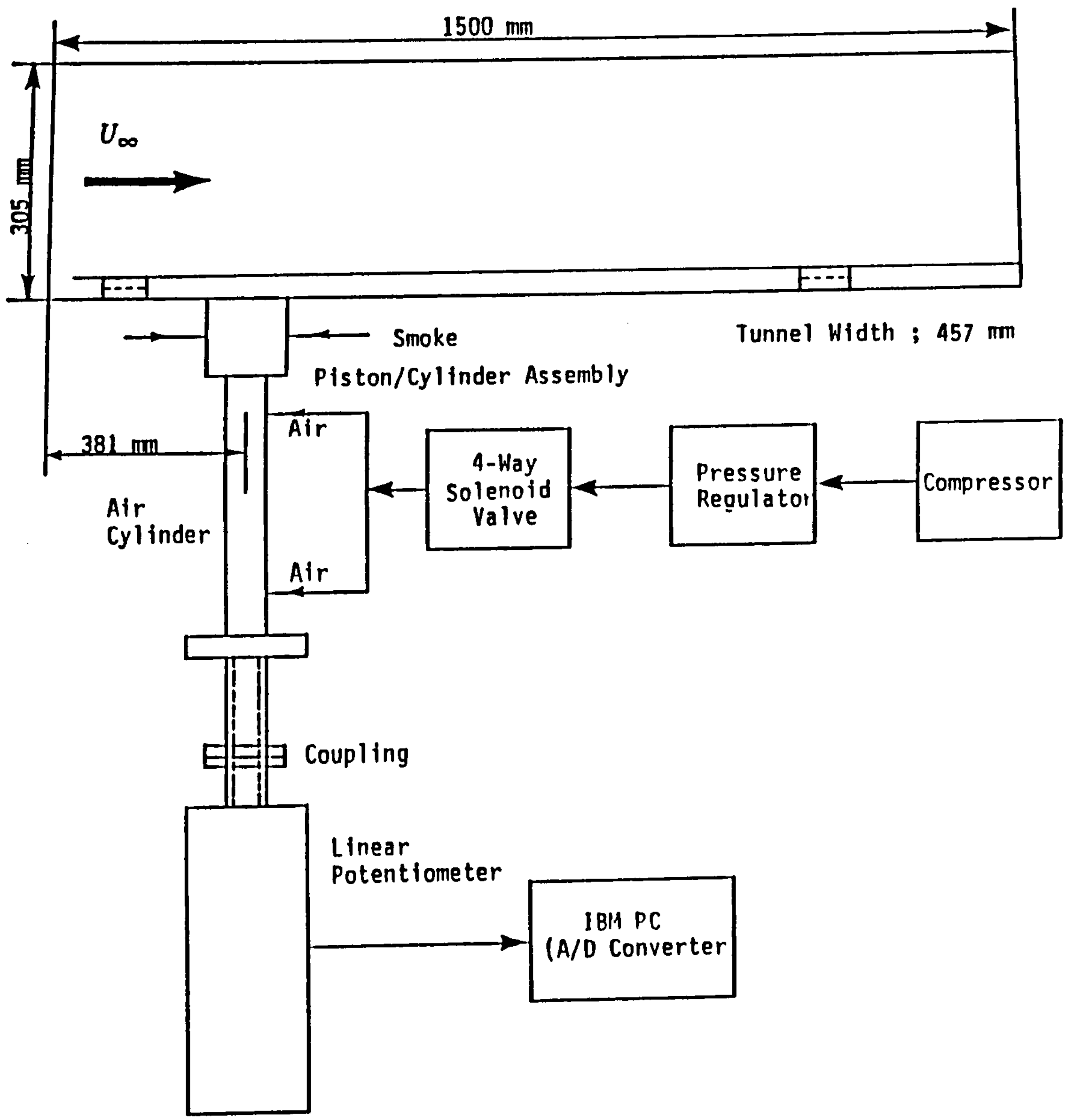

Figure 3.5 Experimental setup and dimensions for single pulsation

ent piston velocity (air pressure) to cross-flow velocity ratios. The variations of $\overline{U}_p/U_\infty$ were obtained by changing both piston velocity and cross-flow velocity. The different piston velocities were easily obtained by changing the supplying air pressure. It ranged from 30 *psi* to 90 *psi*. At lower pressures than 30 *psi*, the piston did not work very well due to large resistance between the O-ring and the cylinder wall.

3.4 Ring Generator for Single Pulsation

The vortex ring is generated by the impulsive motion of a piston in a circular cylinder. The same exit diameter as that of the continuous pulsation experiment was provided to compare the flow features. Figure 3.6 shows the schematic diagram of the piston/cylinder assembly producing the vortex rings. Two pistons were made of copper; one is a straight-walled tube with a constant diameter of 12.7 mm, the other is a sharp-edged orifice with the same exit diameter and 25.4 mm piston diameter. They have flat heads to be flush with the surface of the test section. All parts were machined to excellent tolerances (± 0.001 *inch*). The piston stroke was held constant at 38.1 mm (1.5 in.) in this experiment. However, this piston stroke can be varied by changing the piston shaft length. The air cylinder containing a 9.525 mm (0.375 in.) diameter piston was utilized to actuate the piston for the vortex ring generator. It has double shaft on both ends of its air piston. One was connected to the piston shaft of the ring generator and the other one to the shaft of a linear potentiometer. For smoke visualization, four 3.175 mm diameter holes were drilled along the circumference of the cylinder at 90 degree intervals. These holes are located just above the piston bottom dead center (BDC). A dynamic silicone-rubber O-ring was built into the piston to prevent the leakage between piston and cylinder wall and to keep a smooth piston motion.

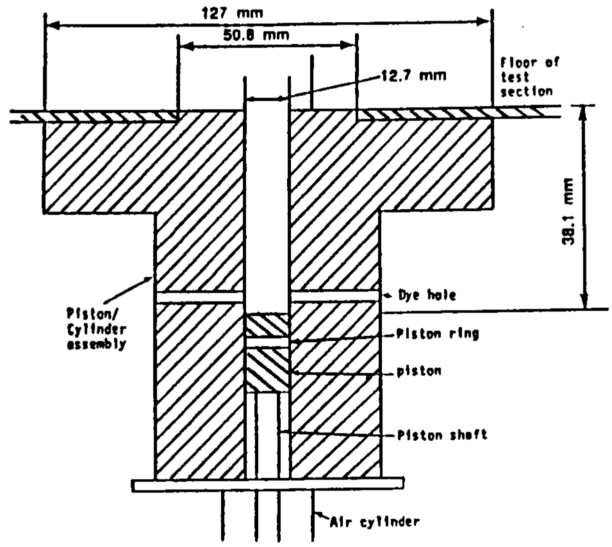

(a) straight walled tube

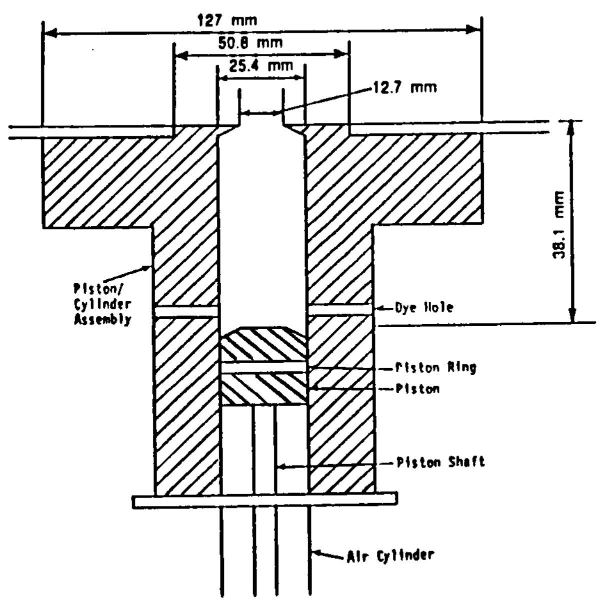

(b) sharp-edged orifice

Figure 3.6 Schematic diagram of the piston/cylinder assemblies

The impulse necessary to produce the vortex rings was obtained from the compressed air. The air flow from the compressor was controlled by a four way solenoid valve (ASCO model 8342C3) which can be energized momentarily by an electric pulse. The piston was forced by supplying air via the solenoid valve from a compressed air reservoir. This solenoid valve had a very short open/close time interval (10 msec). The compressed air pressure was maintained constant by a pressure regulator. The solenoid valve pulses air to the air cylinder, and the piston in the vortex ring generator suddenly moves, displacing water from the jet tube. The piston was near the top of its stroke in the air cylinder, it returned to its starting position by supplying air through another air hole on the cylinder. Under given conditions, valve time duration can be easily adjusted to within a fraction of a millisecond by controlling compressed air pressure with the solenoid. At the end of generation process of the vortex ring, the top of the piston is aligned with the floor of the test section.

The history of the piston motion has a considerable effect on the circulation and the formation process of the vortex ring. For the purpose of recording the profile of the piston velocity in time in detail, an electrical control circuit was constructed. Figure 3.7 represents the control unit indicating how it measured the details of the piston velocity history. There were two photocells in the path of the air piston shaft to detect its motion at the beginning and end of its travel. Photocell 1 was positioned such that it was tripped by the start of the piston motion. This photocell provided the starting signal for the time counter in an IBM PC. Photocell 2 was located 38.1 mm (1.5 in.) away from the photocell 1 so that it provides the stopping signal for time counter. Since the piston stroke was held constant at 38.1 mm in this experiment, as soon as the piston reached the top of its stroke, the counter was stopped. Therefore, the control circuit can provide

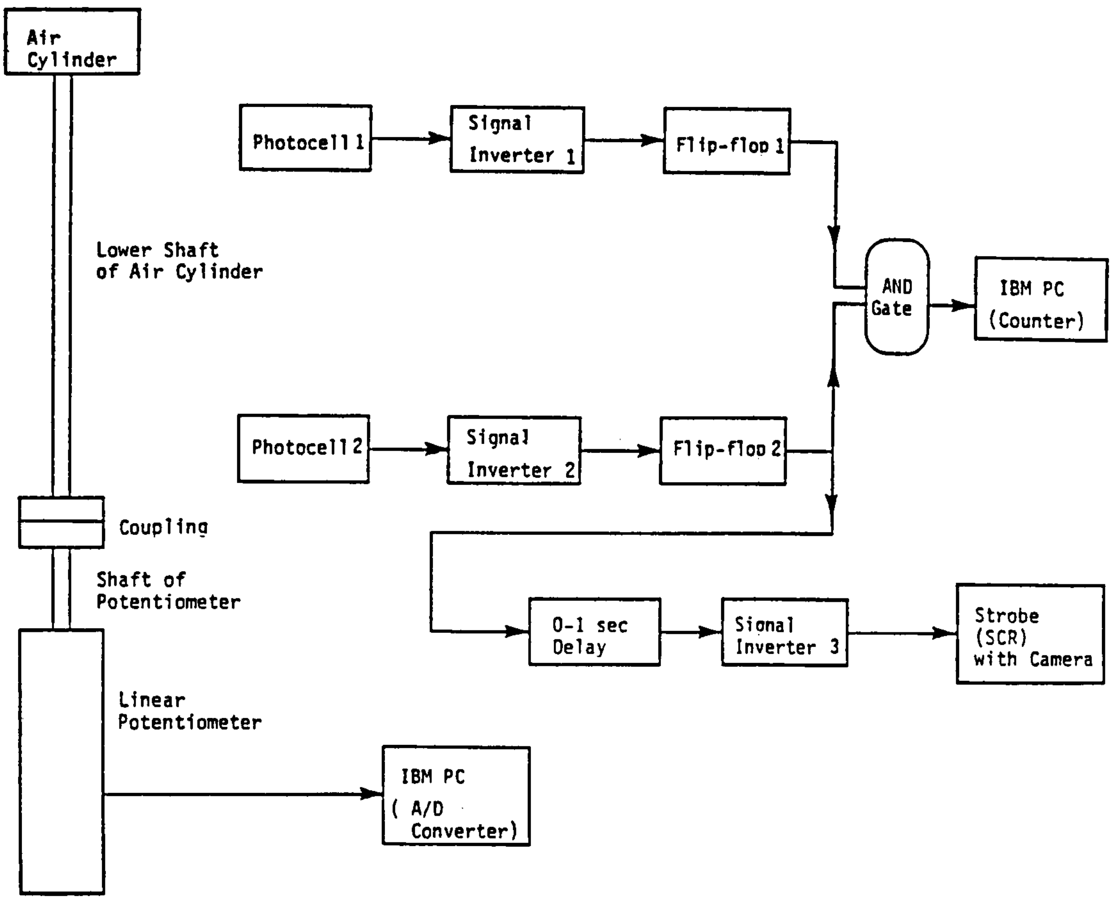

Figure 3.7 Electronic control unit to measure the piston velocity

a single pulse of a specified time duration (T_p) of piston motion and read the instantaneous position during this time duration. Another pulse from a flip-flop circuit was passed through an adjustable delay circuit for synchronization with a stroboscope and a camera. Also, a linear resistance potentiometer was utilized as a position sensor to monitor the displacement-time characteristics by coupling with the lower shaft of the air cylinder. Displacement was recorded as a function of time during each experiment. The output of the potentiometer enters the IBM PC through an analogue to digital (A/D) converter to identify the piston motion.

Some typical piston displacement vs time curves are given in Figure 3-8 (a) & (b) for both of the geometry conditions. Figure 3.8 represents the piston position as a function of time. These trajectories can be approximated by parabolic curves. The actual travel distance of the piston was 38.1 mm, but the position data at the beginning and end of the stroke were not recorded for a short time because of the sensing limitation of the photocells. The lost portion of the curve was easily obtained by extrapolation. Figure 3.9 (a) & (b) represents the history of the piston velocity at the corresponding displacement vs time curves corresponding to Figure 3.8 (a) & (b). The piston velocity is nonlinearly increased with more acceleration at the final part of piston motion shown as in Figure 3.9. This piston velocity was obtained by numerically differentiating the piston displacement. An extremely short deceleration phase at the end of the piston motion was obtained. The acceleration rates are varied depending on the supplied air pressure. The stroke periods ranged from 17 msec to 76 msec. The average velocity of the piston ranged from 46.2 cm/sec to 85.6 cm/sec for a sharp-edged orifice and from 81.8 cm/sec to 200.2 cm/sec for the straight tube exit. The mean jet exit velocity for the straight tube cylinder is the same as the piston velocity by a simple geometric relation. The resulting Reynolds number range based on piston velocity

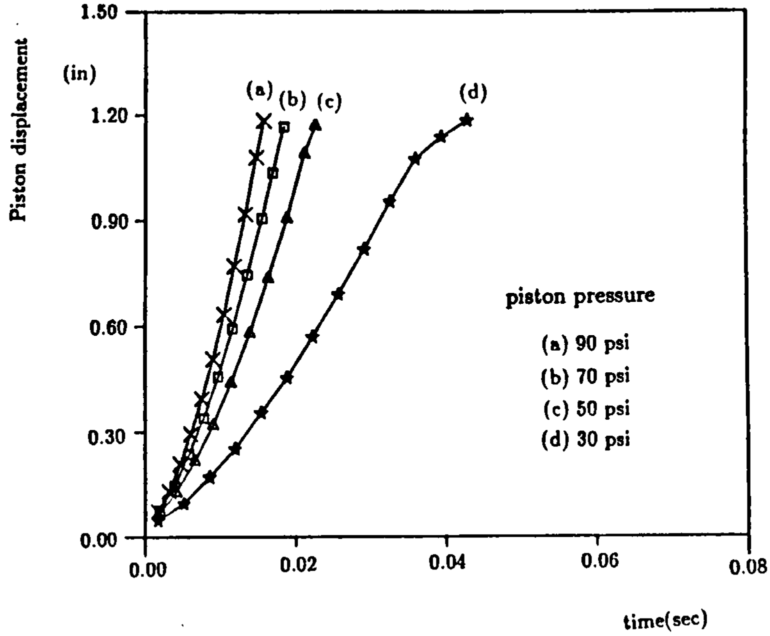

Typical displacement vs time for piston movement with straight tube type exit.

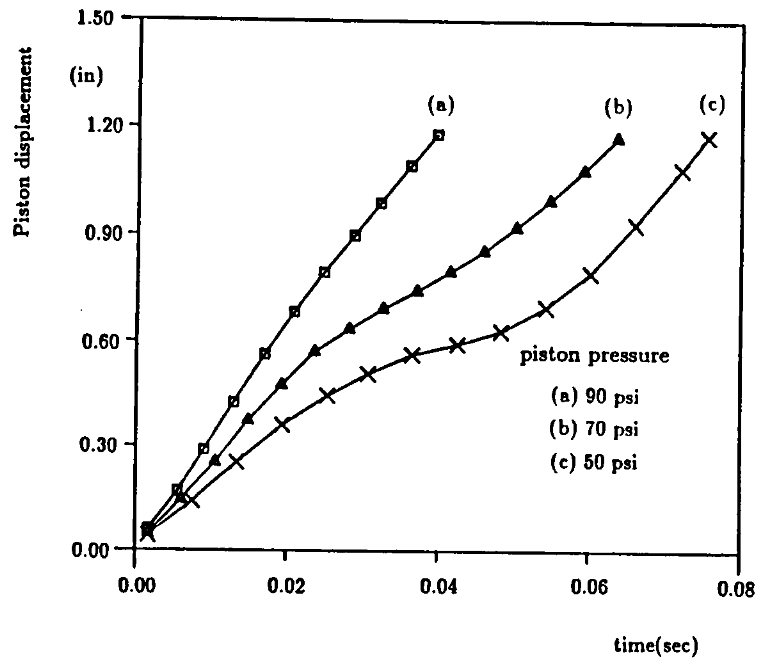

Typical displacement vs time for piston movement with sharp-edged orifice type exit.

Figure 3.8 Typical piston displacement vs time curve

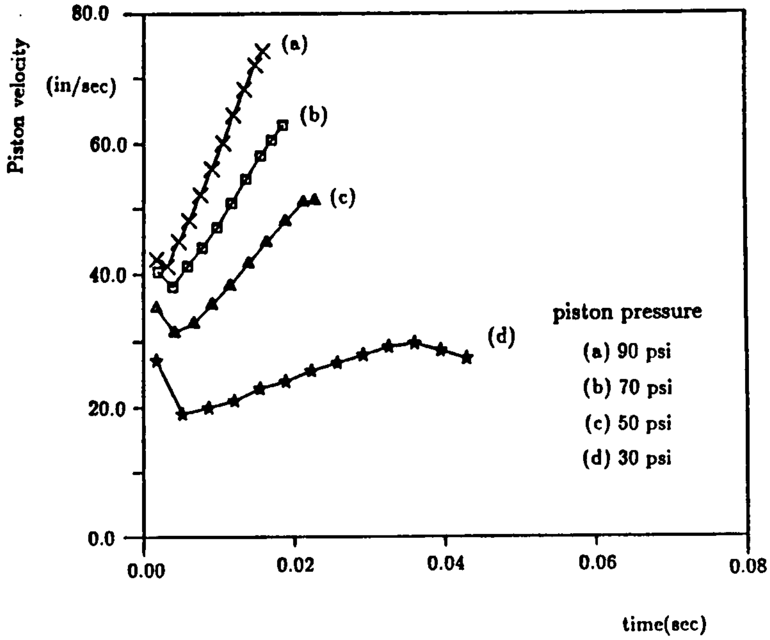

Typical piston velocity profile vs time for piston movement with straight tube type exit.

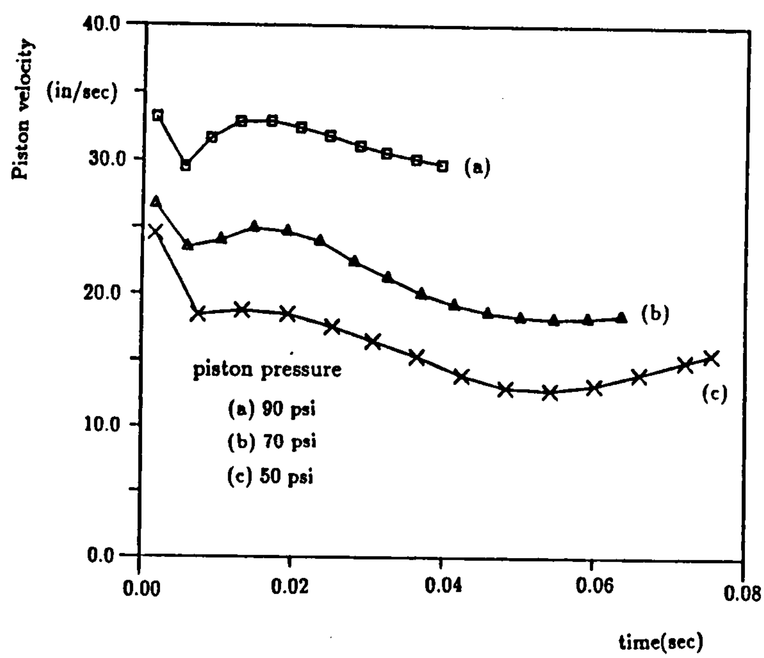

Typical piston velocity profile vs time for piston movement with sharp-edged orifice type exit.

Figure 3.9 Typical piston velocity vs time curve and diameter was between 1.5×10^4 and 4.0×10^4. In the present experiment, this range of Reynolds number flow produced a laminar vortex ring (Glezer, 1989). A photographic technique based on different exposure times was used to measure the translational velocity, the diameter and the trajectory of the vortex rings in cross-flow.

3.5 Hot Film Anemometry and Data Acquisition

Hot-film anemometry was used to study the velocity field of vortex rings in cross-flow. A single hot-film probe was utilized with anemometers operated in the constant-temperature mode to measure mean velocities in the three-dimensional flow field. The Constant Temperature Anemometry (CTA) system is comprised of TSI hot-film probes, a TSI model IFA 100 Intelligent Flow Analyzer, a Scientific Solution's Lab Master 16 channel A/D converter, a 1 MHz low band pass filter and IBM pc with 20 mega byte hard disk. An oscilloscope was connected to the control box to observe the voltage traces obtained from measurements within the flow field. A switch and power supply were also incorporated to coordinate the discrete pulsations of the jet.

Fig. 3.10 represents a schematic diagram for the thermal anemometer and data acquisition system. The voltage signals from the hot-film probe were sent into the IFA Intelligent Flow Analyzer which is connected to the Lab Master A/D converter. The signals pass through the 1 MHz band pass filter to eliminate noise. The signals were digitized and temporarily stored on a hard disk. The data were sent to a VAX 11/785 computer for storage and evaluation to obtain the velocity components from the calibration results.

An overheat ratio of 1.04 was used for the constant-temperature mode in this study. This value was selected to reduce the influence of free convection from the

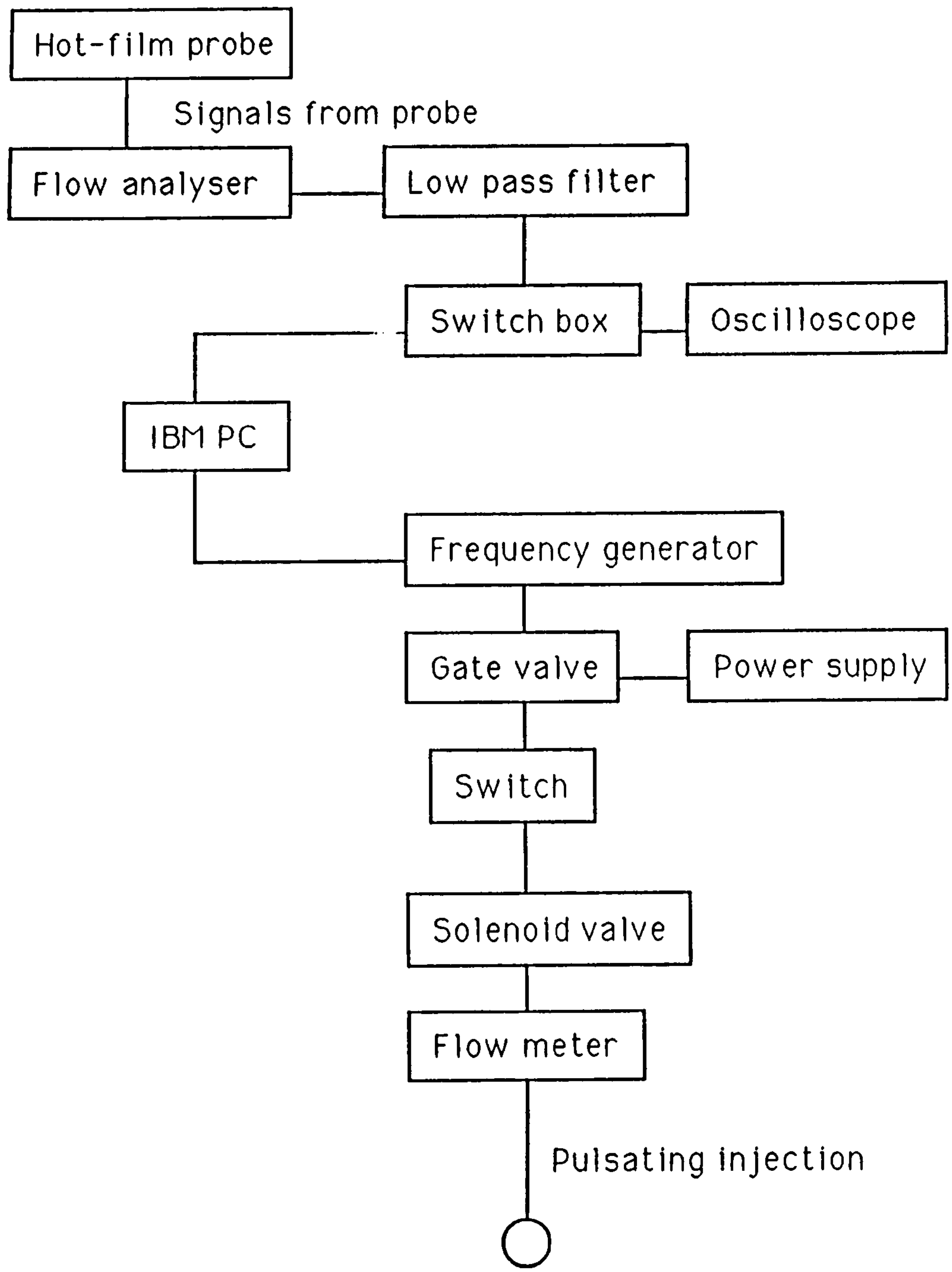

Figure 3.10 Schematic diagram for thermal anemometer and data acquisition system

probe affecting the lower limit of the velocity at which the probe can be accurately operated. The probe lifetime is also improved by using this relatively low overheat ratio.

In the following sections, a probe calibration will be described with a discussion of directional characteristics of a hot-film probe. Also, general expression for the effective cooling velocity of a probe in the three-dimensional flow field will be derived for the interpretation of the anemometer output signal.

3.5.1 Probe Calibrations

A single probe (TSI model 1212-60W) was calibrated by recording its output voltages versus known velocities. In order to determine the yaw sensitivity, yaw factor was calculated by measuring the output at different yaw angles. For this purpose, a circular calibration water channel has been constructed. The calibration was conducted at several different ranges of temperatures. Details of the calibration facility and procedures are described in Appendix A.

3.5.2 Output Signal Analysis in the Three-Dimensional Flow Field

The proper interpretation of hot-wire/film anemometer signals can be followed by the accurate description of the directional responses of the individual probe. This directional responses is commonly described in terms of an 'effective cooling velocity' which refers to the dependence of the heat transfer rate from the probe to the flow field. The most conventional relationship, the cosine law, notes that only the normal component of the velocity across the wire contributes to the cooling. In this case, the effective velocity is proportional to the cosine of the yaw angle, and there is no effect due to the pitch, i.e. rotation about the axis of the wire. Many investigators introduced improved cooling laws that account for cooling by the parallel component of velocity (Hinze (1959), Webster (1962), Fujita and Kovasznay (1962), Bruun (1971) and Drubka et al. (1977)).

Hinze (1959) introduced a yaw factor correction for the cosine cooling law which has been most commonly used. He noted that the yaw factor increases as the velocity reduces in the range from 0.1 to 0.3. On the other hand, Webster (1962) proposed a value of 0.2 and argued that there is no systematic dependence of the yaw factor on the sensor aspect ratio. Champagne et al. (1967) have performed heat transfer measurements on the normal and slanted probes in subsonic air and found that directional effects observed in yaw are normally attributed to heat transfer phenomena in the yawed flow around the sensor. Directional effects observed in pitch are necessarily caused by the curvature of the sensor and aerodynamic disturbances generated by the wire mounting prongs and the probe shaft. Irwin (1971) tried to determine the yaw factor k for the slanted wire. He also investigated the variations when some of the wires were plated at the ends, where they are fastened to the prongs. He noted that the yaw factor k seems to be independent of the yaw angle ϕ and has a value of about 0.12 for wires with plated ends ($l/d = 185$), and with unplated ends ($l/d = 240$). The yaw factor k seems to decrease with increasing velocity but it is difficult to be certain of this from the work by Bruun (1971) because of the large scatter of the data.

Jorgensen (1971) studied the directional characteristics for yaw and pitch angle effects. He suggested an equation of the following form to account for the support interference.

$$U_{eff}^2 = U_N^2 + k_1^2 U_T^2 + k_2^2 U_{BN}^2 \qquad (3-1)$$

where U_{eff} is the effective cooling velocity, U_N the normal velocity component to the sensor and lying in the plane of supports, U_{BN} the binormal velocity component to the sensor and supports. k_1 and k_2 indicate the yaw and pitch factors, respectively. Fig. 3.11 shows the probe-fixed coordinate system and the velocity components at the sensor. Equation (3–1) can be reduced to the following expressions.

For the case of zero pitch angle,

$$U_{eff}(\phi)^2 = U(0)^2(\cos^2\phi + {k_1}^2\sin^2\phi) \qquad (3-2)$$

For the case of zero yaw angle,

$$U_{eff}(\psi)^2 = U(0)^2(\cos^2\psi + {k_2}^2\sin^2\psi) \qquad (3-3)$$

Equations (3–2) and (3–3) are identical forms that Hinze (1959) and Dahm (1969) proposed for directional sensitivity and aerodynamic disturbance effects.

The output signal analysis in the general three-dimensional flow field is described in Appendix B. The mean velocity components are given as follows in terms of the mean cooling effective velocity at two different rotational directions.

$$\overline{U}^2 = \frac{1}{{k_2}^2 - {k_1}^2}({\overline{U}_{eff}}^2(\theta = 90°) - {\overline{U}_{eff}}^2(\theta = 0°)) \qquad (3-4)$$

$$\overline{W}^2 = \frac{1}{{k_2}^2 - {k_1}^2}({k_2}^2{\overline{U}_{eff}}^2(\theta = 0°) - {k_1}^2{\overline{U}_{eff}}^2(\theta = 90°)) \qquad (3-5)$$

3.6 Flow Visualization Techniques

Two types of flow visualization techniques were utilized for water tunnel experiment to complement each other for complete description and analysis of the flow details. The techniques unveiled the global flow features of vortex rings in cross-flow. The flow was visualized using a common dye technique. The dye was a mixture of commercial food coloring, alcohol, and evaporated milk with a specific

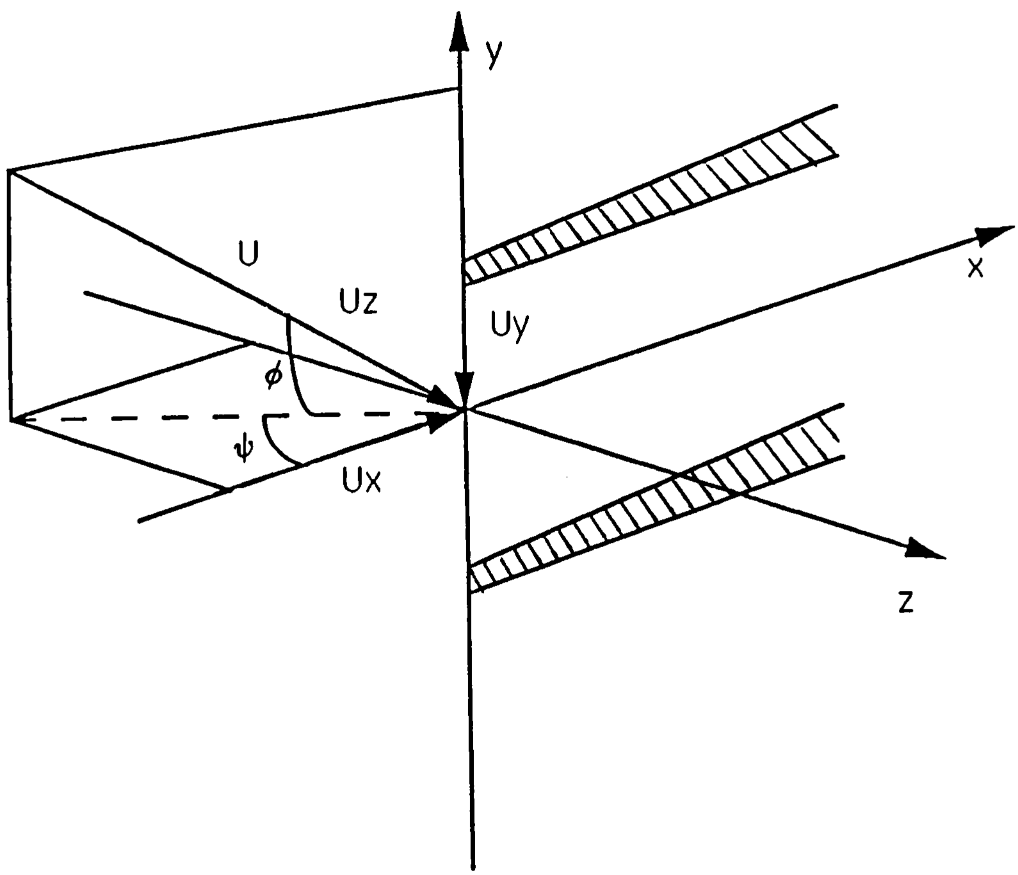

Figure 3.11 Probe-fixed coordinate system and velocity components

gravity of one. Internal dye ports were built into the jet exit region to allow flow visualization with minimal disturbance into the local flow and therefore the vortex rings were colored.

A laser sheet technique was applied to provide a sectional view of the vortex rings. An Argon ion laser light source with maximum power output of 2 watts was used for the laser sheet visualization. A 45° inclined mirror and a 4 mm cylindrical lens were utilized to reflect and produce a plane laser light sheet as shown in Figure 3.12. Rhodamine 6G fluorescent dye was supplied in small concentration through four holes around the nozzle to coordinate the pulsing fluid. The movement of the lens resulted in rotation of the laser sheet plane. Sectional views of the vortex ring were obtained to analyze the detailed structure of the ring and its wake.

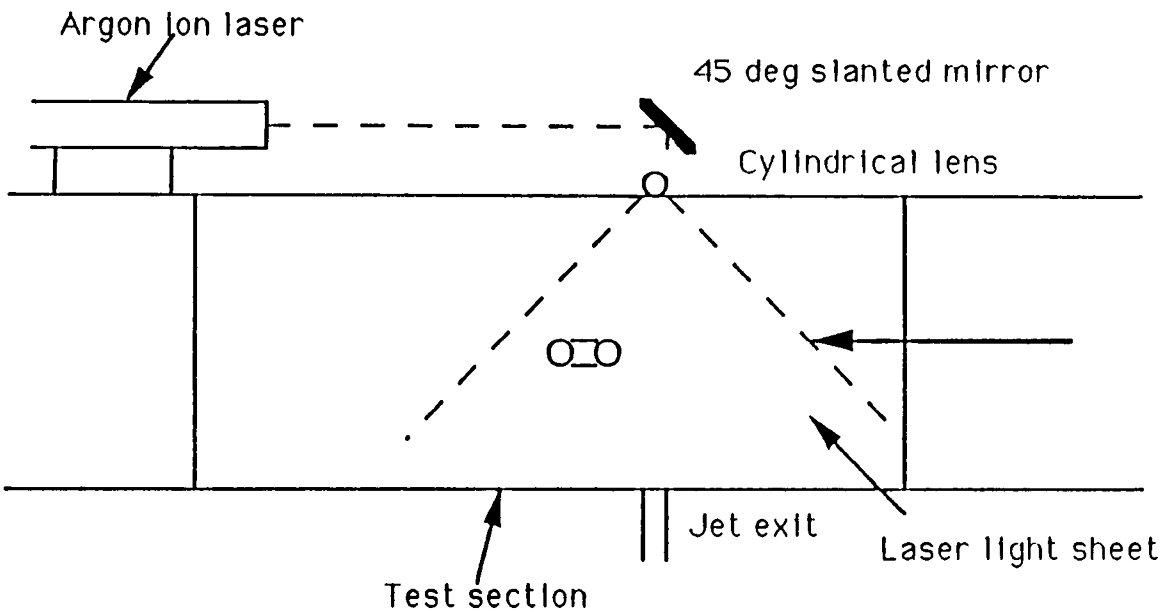

Figure 3.12 A layout for laser sheet flow visualization

4. Experimental Results and Discussion

4.1 Continuous Pulsation

Figure 4.1 shows some photographs which reveal several fundamental vortex ring features observed in the present study such as the size, tilting and trajectory of the vortex rings while moving in the cross-flow. The direction of the cross-flow was from right to left in the photographs. From these observation it was evident that the vortex rings, under some range of parameters in this study, move as unit blob of fluid with little change in their general shape. This indicates that the vortex rings maintain stable laminar flow at relatively low pulsation frequencies.

The tilted shapes and wake structures of the vortex ring were clearly identified using laser-induced fluorescence (LIF) flow visualization as shown in Figure 4.2. Also, relevant features of the flow field around a vortex ring in uniform cross-flow are schematically drawn in Figure 4.3. The core of the vortex ring is identified as the regime of highly concentrated vorticity where the velocity varies linearly with the distance from its center. Also, a wake region, where a small amount of the ring fluid and vorticity is left, exists behind the ring. It was found that the wake region has very small effect on the motion of the vortex ring, which is in agreement with Maxworthy(1974).

As the pulsation frequency increased in this experiment, two separate physical phenomena were seen to affect the vortex rings and their trajectories. First, the circulation strength within each ring was reduced, which directly resulted in the reduction of its induced translational velocity. This makes the cross-flow momentum overcome each ring easily and deflects it into the downstream. Second, the distance between the sequential rings reduces as the frequency increases. This results in interactions between the rings, such that the vortex rings quickly coa-

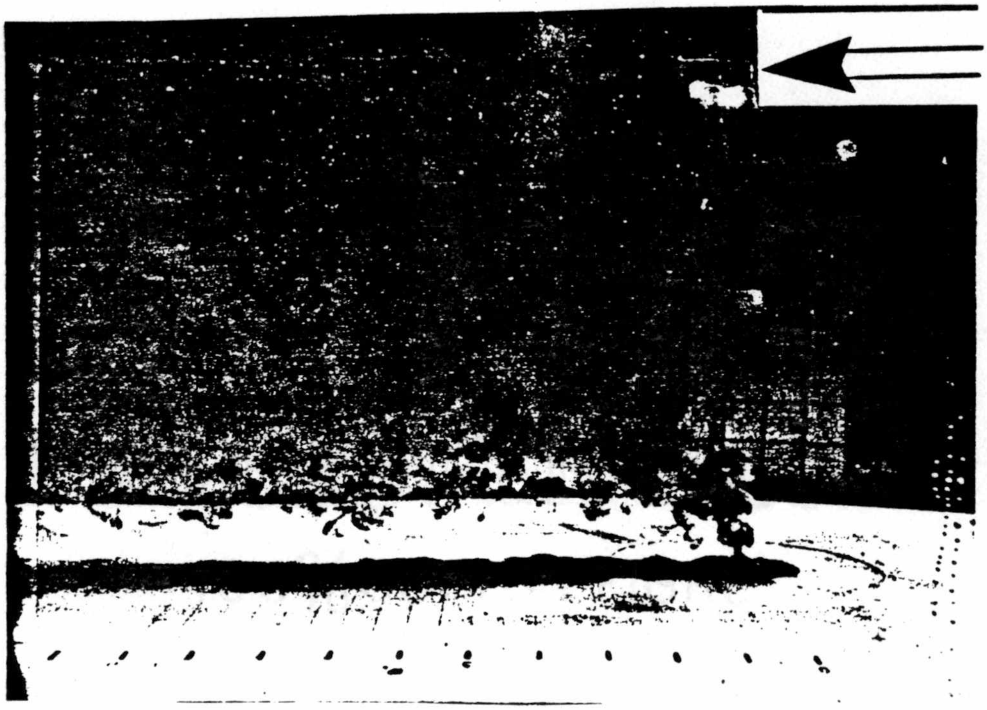

(a) Pulsed at 1 Hz

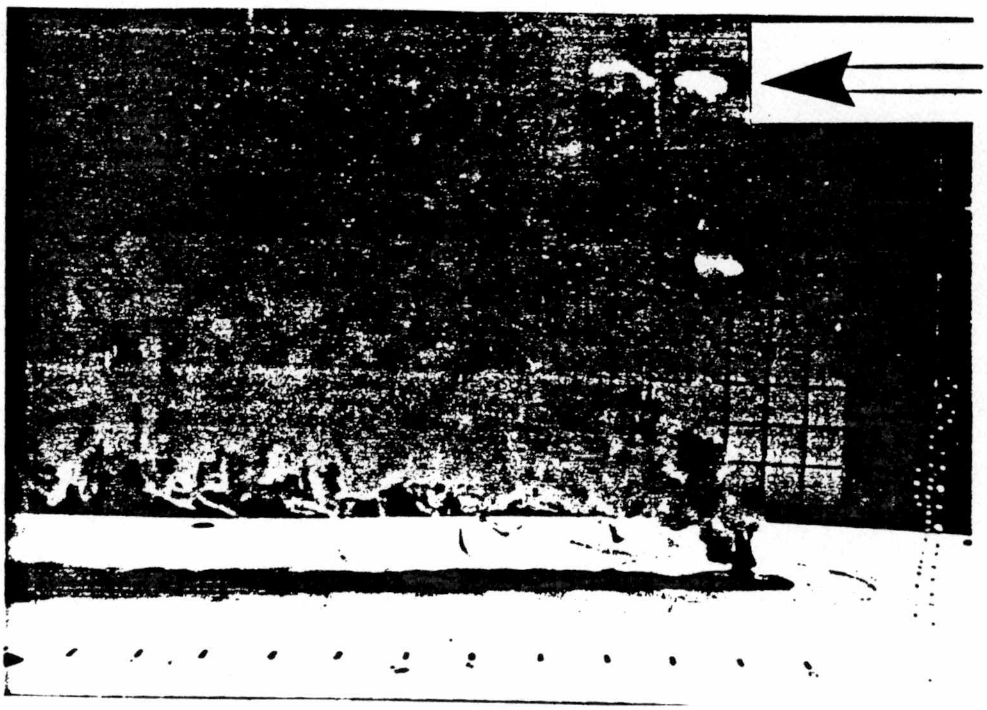

(b) Pulsed at 2 Hz

Figure 4.1 Typical photographs of vortex rings in cross-flow for various pulsations for $\frac{\overline{U}_j}{U_\infty} = 1.5$, $Re_{dj} = 1870$

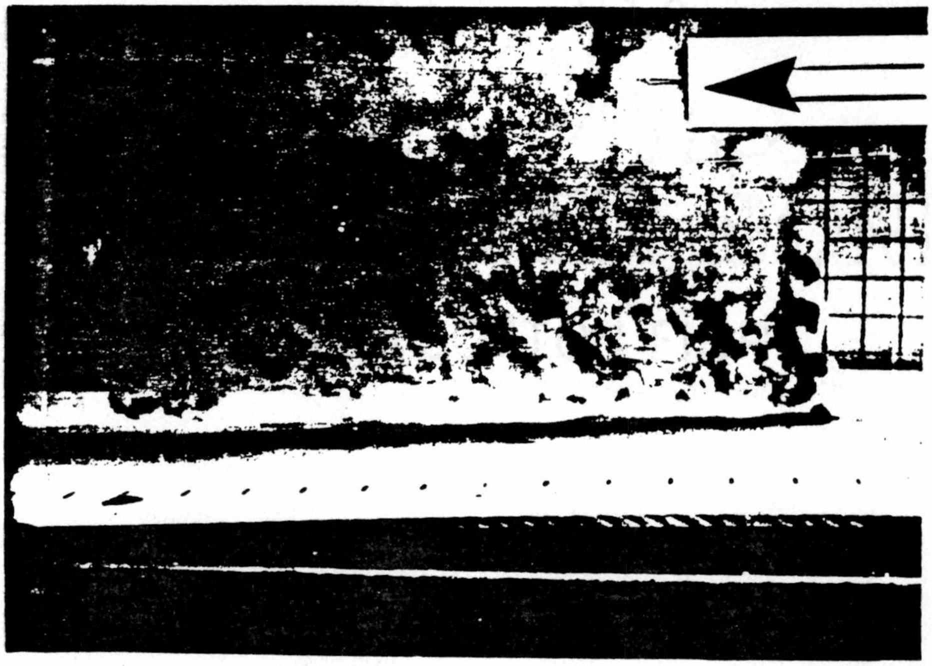

(c) Pulsed at 10 Hz

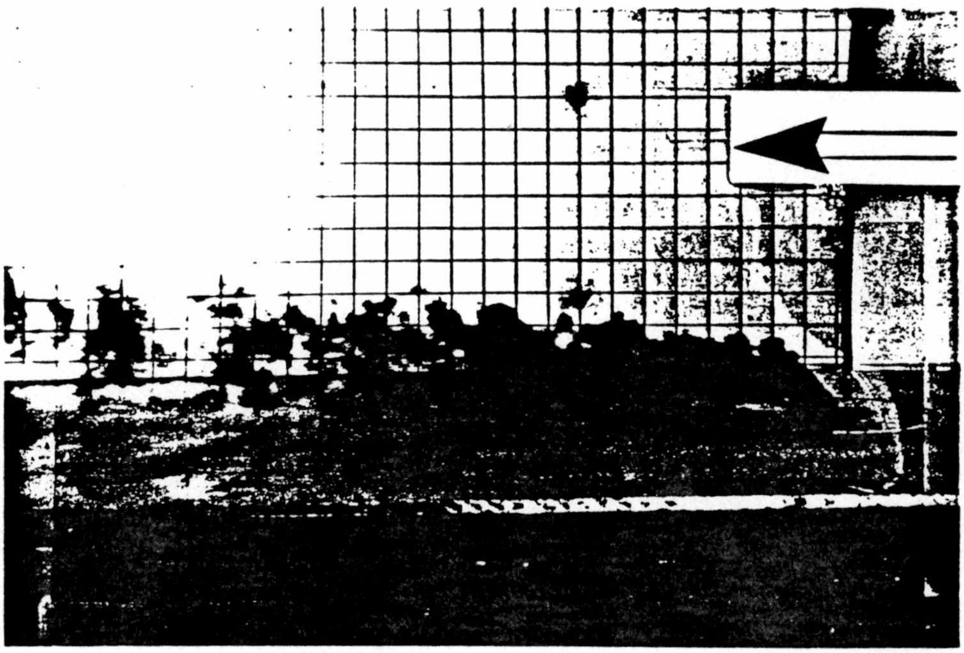

(d) Steady jet

Figure 4.1 Continued

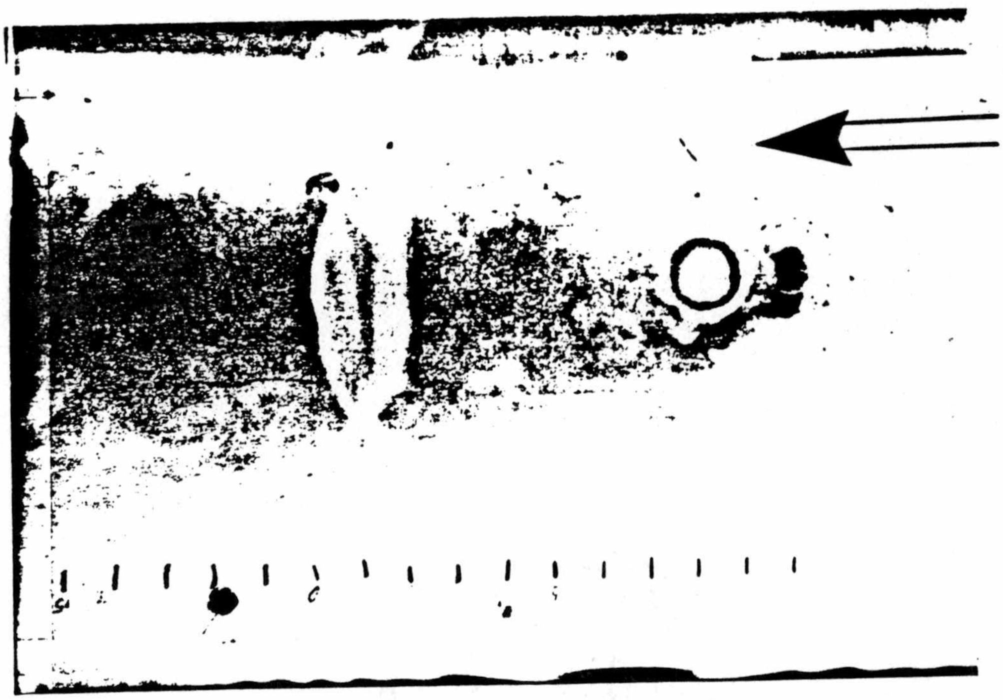

(e) Top view of a ring at 1 Hz pulsation

Figure 4.1 Continued

(a) 1 Hz

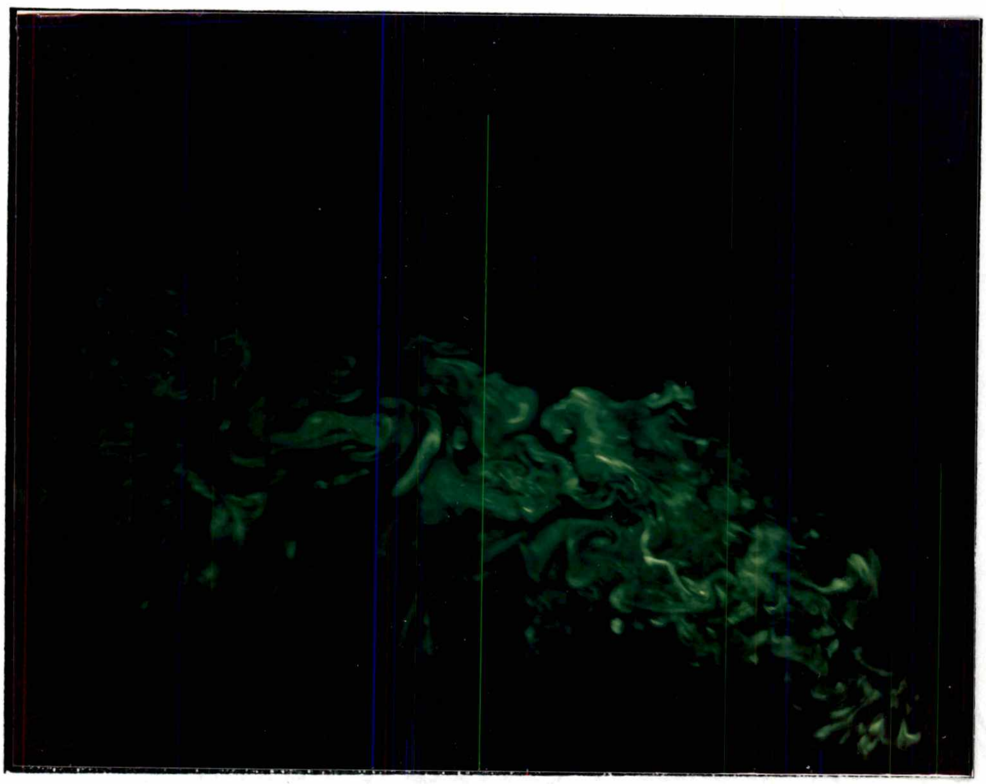

(b) 10 Hz

Figure 4.2 Detail structure of ring in cross-flow by LIF

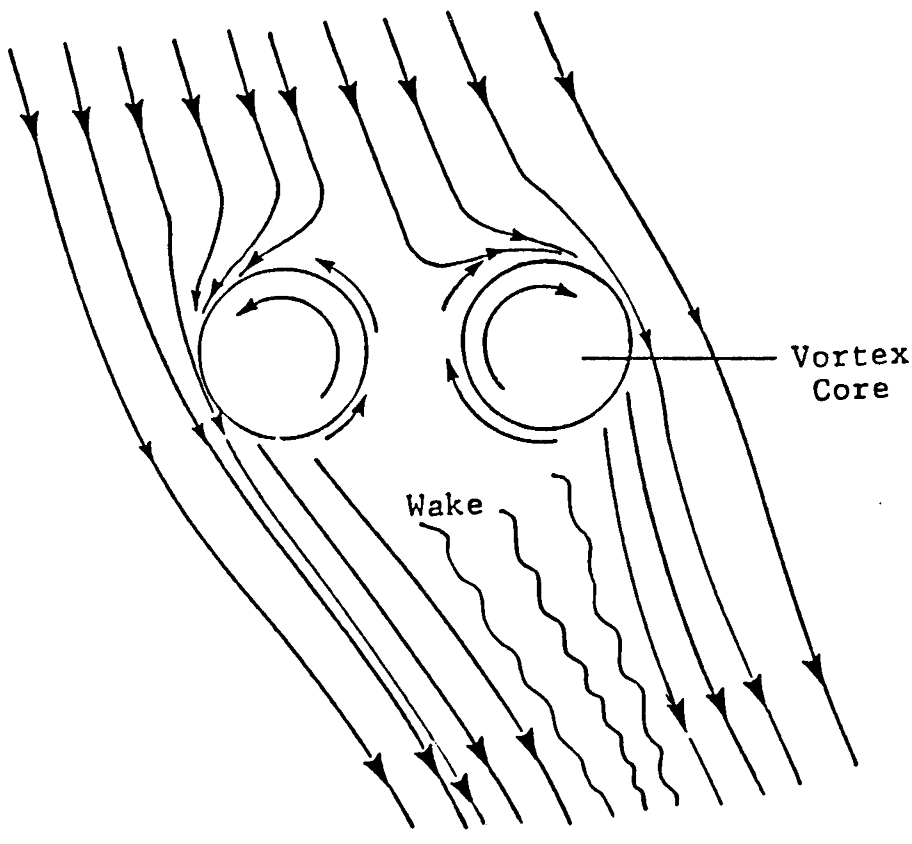

Figure 4.3 Sectional view of cross-flow and vortex ring structure in a frame moving with the ring

lesce. In this case, when two sequential vortex rings are close to each other, the vortex diameter of the forward vortex ring increases with decreasing vortex ring velocity; the diameter of the rearward vortex ring decreases while its vortex ring velocity increases. Since this interaction is present during the initial development of the individual rings, the rings are not fully-formed as they are turned into the downstream direction. Therefore, it appears that the flow geometry, including the trajectory, at 10 Hz jet pulse is similar to the steady jet case; see Figure 4.1.

In what follows, simplified measurements of normalized ring geometry are first presented. The ring diameters were measured at many points along the ring trajectory, for various pulsation frequencies, and for different jet to the cross-flow velocity ratios. Figure 4.4 shows the variations of vortex ring diameter as the ring moves into the cross-flow. In this figure, D' is the diameter of a vortex ring to the outermost closed streamline. Vortex ring diameter nonlinearly increases, in a slightly different manner from a vortex ring moving in still fluid, as the ring moves up toward the ceiling of the water tunnel. It seems that there is a transition point from larger ring growth rate to smaller growth rate. This indicates that, relatively far downstream, the growth rate of the vortex ring diameter is decreased due to the effect of the cross-flow velocity. Arnold (1974) carried out experiments with a vortex ring produced against the flow of a water stream in a long flume. He reported a reversed nonlinear growth rate as the vortex ring moves downstream over a longer distance. The experimental results illustrated that ring growth rate is further increased after an initial linear portion. A considerable increase in ring diameter was observed in experiments based on continuous pulsation, compared to single pulsation experiments using a piston/cylinder assembly. For high $\overline{U}_j/U_\infty$, the data on Figure 4.4 compare very favorably with the results of Maxworthy(1977) obtained by using piston movement, with different piston length to diameter ratios.

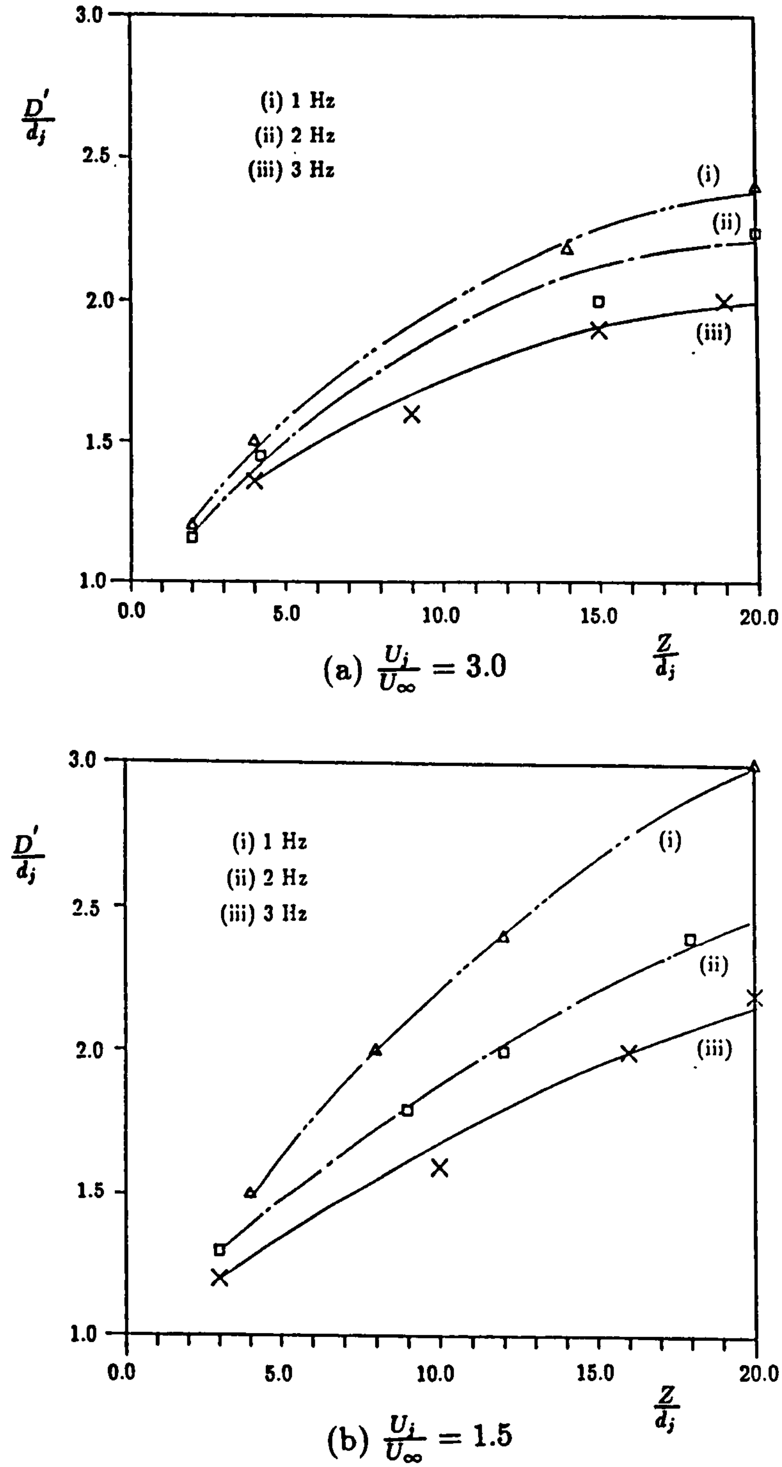

Figure 4.4 Variations of ring diameter for various frequencies

Since one of the most difficult measurements is to evaluate the exact ring core size, the following simple technique was introduced at the initial stage of the present study to estimate the diameter and the core size of the rings. Given the assumption that vorticity moves with the fluid in an incompressible flow, it was shown by assuming inviscid flow that (Walker et al., 1985)

$$R(t)a^2(t) = C \qquad (4-1)$$

where C is a constant related to the initial volume of the core of the ring. If $R(t)$ and $a(t)$ are identified at a point where they can be easily and accurately determined, the constant value of C is calculated based on equation (4-1). A typical value of constant C, in this experiment, was 0.064 cm^3/sec for $\overline{U}_j/U\infty =$ 1.5 with pulsation of 1 Hz. From side view photographs, the core radius (a) at arbitrary point in the downstream where $R(t)$ is measured, can be determined. At the instant the vortex ring is formed near the orifice, the size of the vortex core is relatively large. It occupies almost one half of the ring radius, at the initial stage of formation. The core of the vortex ring from the continuous pulsating jet is relatively thicker than that in a single pulsating jet due to lower translational velocity and lower jet exit velocity. On the other hand, the translational velocity can be measured at that point, and the circulation can be estimated by using the equation for translational velocity (4-2) for a vortex ring provided below. Detailed quantitative analysis will be discussed in Section 4.3 in terms of hot-film measurements.

Direct measurement of circulation Γ is very complicated and has been discussed by several authors (Sullivan(1973), Maxworthy(1974), and Didden(1979)). For simplified calculation, we may assume that the circulation in the vortex ring remains constant beyond the point where the vortex ring has traveled a few jet diameters beyond the exit point. Therefore, this study presents that a consistent approach to determine the circulation from measurements of the ring geometry and the induced velocity. A more accurate method will also be used to determine the circulation and presented later in this dissertation to see how it compares to the simplified analysis.

The translational velocity of a vortex ring is generated by effects induced by the elements of the ring on each other. The translational velocity of a vortex ring depends on the details of the vortex ring such as core size (a), ring size (R) and circulation distribution (Γ). This is typically calculated using the Biot–Savart law and has been evaluated as:

$$U_T = \frac{\Gamma}{4\pi R}\left\{ ln\frac{8R}{a} + A - \frac{1}{2}\right\}. \qquad (4-2)$$

This relation can be rewritten using equation (4-1):

$$U_T = \frac{\Gamma}{8\pi R}\left\{ ln\frac{64R^3}{C} + 2A - 1\right\} \qquad (4-3)$$

where Γ is circulation in the ring, a is the core radius, R is the ring radius, and A is an empirical value dependent on time from the formation of the vortex ring. Since it takes about 35 seconds for the vorticity to diffuse to the center of the ring at similar Reynolds number range, viscous effects can be neglected which occur during a few seconds of ring formation in this experiment (Kambe and Oshima, 1975).

Since the expression for the translational velocity of a vortex ring was derived for a free, isolated vortex ring, this relation would seem least appropriate where the vortex rings are close together, such as occurs at the cases with relatively high pulsation frequencies in the present study. This expression would be applicable for vortices least involved in vortex ring coalescence, where the diameter of the vortex ring and the distance between sequential vortex rings remain relatively constant with elapse time as the vortex rings move downstream.

Actually, Widnall(1973) has shown that the results using this relation for $A = 1/4$ for a viscous vortex ring will be accurate to within 20%. As a result, in the present study, this relation is used to identify ring circulation at a point where U_T, R and a are obtained from the experiments. Then we can use the circulation obtained from this calculation to find the translational velocity at other points of the vortex ring trajectory where it cannot be readily measured. Based on the knowledge of U_T along the path taken by the vortex ring, we may use equations (2-1)–(2-4) to predict the dynamic characteristics of the vortex ring in uniform cross-flow.

4.2 Single Pulsation

As mentioned in Section 3, two different types of exit geometries were introduced in the single pulsation experiments. As soon as the fluid puffs up, the different vortex ring dimensions appear in the vicinity of two different types of exits, as shown in Figure 4.5. In the ranges of operational parameters for the present experiment, it was observed that the cross-flow does not affect the initial formation of a vortex ring. Experimental results show the fact that as the vortex rings moved into the cross-flow, the ring growth for a straight walled tube was slightly larger than that for a sharp–edged orifice. As shown in Table 4.1 and 4.2, the exit velocity and consequently, translational velocity and circulation of a vortex ring produced by a sharp–edged orifice is much greater than for a vortex ring from a straight walled tube, for the same piston velocity.

Vortex rings formed at the exit of sharp–edged orifice entrained less fluid than those ejected from a straight tube exit. This appears to be due to an increased

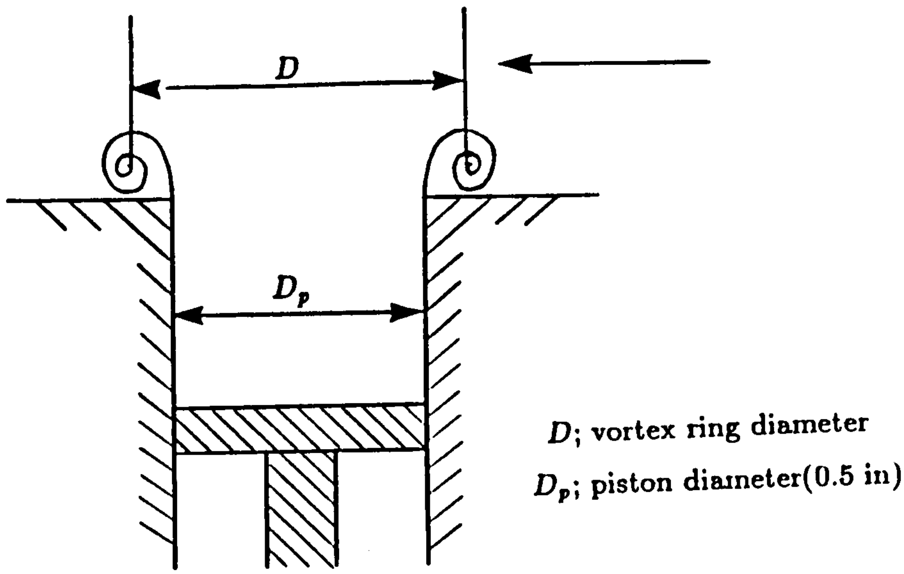

(a) Straight tube

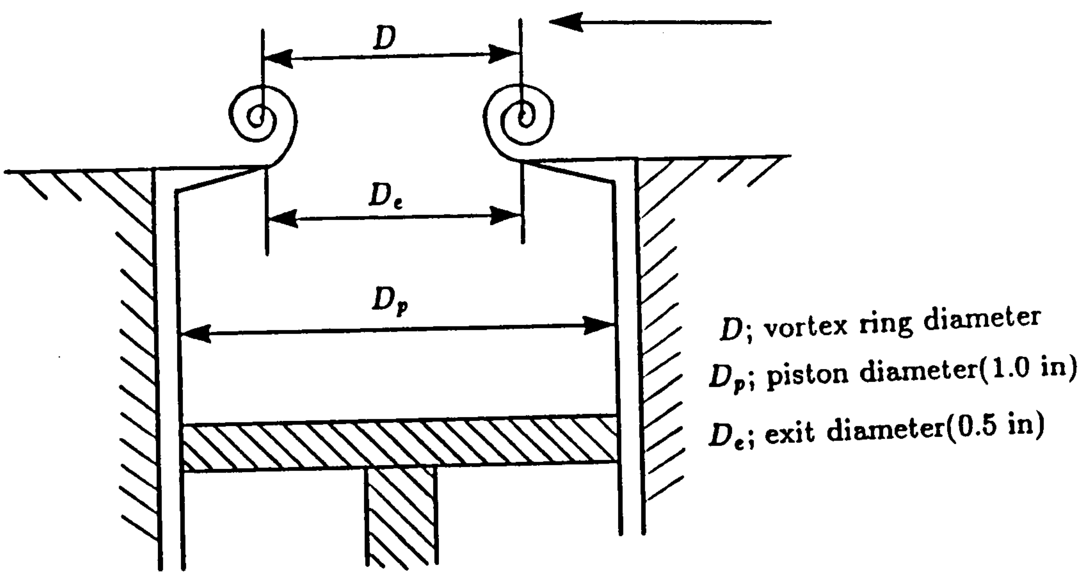

(b) Sharp-edged orifice

Figure 4.5 Ring formation at different exit conditions

Table 4.1 Time duration and piston velocity measurements

	Sharp-edged Orifice		Straight Tube	
Piston Pressure (psi)	Time Duration (sec)	Piston Velocity (in/sec)	Time Duration (sec)	Piston Velocity (in/sec)
30			0.044	32.2
50	0.078	18.2	0.023	61.7
70	0.064	22.2	0.020	70.9
90	0.042	33.8	0.018	78.8

Table 4.2 Exit velocity results at each condition

	Sharp-edged Orifice	Straight Tube
Piston Pressure (psi)	Exit Velocity (in/sec)	Exit Velocity (in/sec)
30		32.2
50	72.8	61.7
70	88.8	70.9
90	135.2	78.8

detachment of secondary vorticity, of the opposite sense from the outside wall by the boundary layer formed by the entrained flow, passing over the floor surface, for a sharp–edged case. The ring growth appeared to be independent of piston velocity and/or exit Reynolds number over the range of parameters in this experiment for both of the geometries.

There were three significant results with respect to vortex ring penetration in the cross-flow. First, as the piston velocity increases, the penetration level increases for the same cross-flow velocity. Second, at the same piston velocity, the penetration height of the vortex ring from the sharp–edged orifice is much deeper than than that of straight tube, as shown in Figure 4.6 (a). Third, for the same exit velocity which is obtained by different piston pressures and piston velocities, the penetration level does not vary significantly as presented in Figure 4.6 (b). However, it is slightly deeper for the sharp-edged orifice than for the straight walled tube. This is due to faster translational velocity associated with a little smaller ring and, at least theoretically, the same circulation in the case of a sharp-edged orifice.

4.3 Quantitative Analysis

Most of the research in vortex rings are based upon flow visualization, and are therefore, to some extent, descriptive and subjective. There have been relatively few quantitative studies to measure the detailed structure of the ring (Refer to Section 1. Introduction). As discussed in Section 2, the circulation, vorticity distribution, core size and translational velocity can be determined throughout the ring from measurements of the velocity components. Also, the stability and entrainment will be dependent on the detailed structure of the ring.

As observed in the flow visualization of the present study, some characteristics

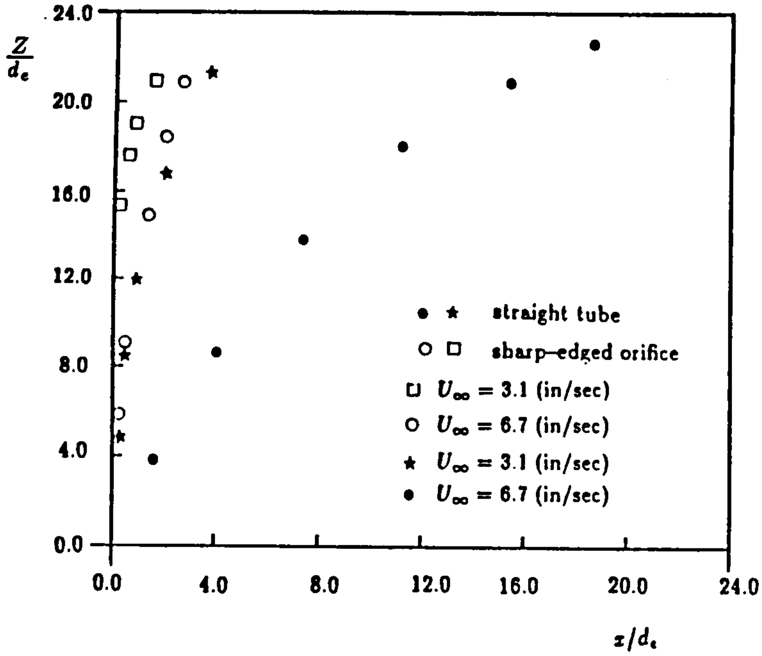

(a) Penetration trajectories of vortex rings in the cross-flow at the same piston velocity $U_p = 33.5$ (in/sec) for different exit geometries using vortex ring generator(piston/cylinder assembly).

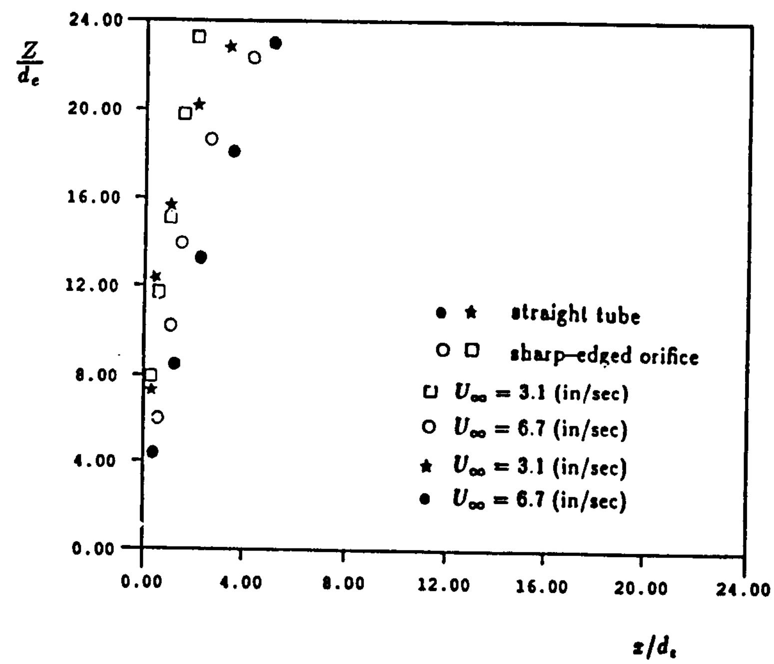

(b) Penetration trajectories of vortex rings in the cross-flow at the same exit velocity $U_j = 72.0$ (in/sec) for different exit geometries using vortex ring generator

Figure 4.6 Penetration trajectories of vortex rings for various piston pressures of a the vortex ring in cross-flow (for example, tilted motion of the ring, the ring trajectory and the growth of ring) are interesting phenomena which may be important factors even in terms of fluid mixing. In order to understand and confirm some of the above-mentioned specific features, it was necessary to investigate the quantitative characteristics. In this section, the results of hot-film measurements are discussed.

To illustrate the present, quantitative measurements, a typical vortex ring in the cross-flow case was selected with a velocity ratio, $\overline{U}_j/U_\infty = 3.0$, and frequency, $f = 1\ Hz$. The velocity field ($\overline{W}$ and $\overline{U}$) of the ring in cross-flow was measured at three different downstream locations ($Z = 3d_j$, $7d_j$ and $10d_j$). The mean pulsating velocity($\overline{u}$) at $f = 1Hz$ was 12.63 cm/sec which corresponds to the velocity ratio, $\overline{u}/U_\infty = 2.4$ in this case. A single hot-film was used to measure two velocity components, $\overline{W}$ and $\overline{U}$, at a fixed point as the vortex ring pass by the measuring point. Two velocity components are measured by rotating the plane of the prong through 90°. The first probe position selected was parallel to the cross-flow ($\theta = 0°$) and the other probe position was perpendicular to the cross-flow ($\theta = 90°$) in the $Y - Z$ plane.

An uncertainty analysis was made to estimate measurement uncertainties of the hot-film measurements, Appendix C. These include an error analysis of the mean jet velocity, sensor operating temperature, corrected effective cooling velocity, time-averaged mean velocities in the vortex ring, translational velocity, circulation, core and ring sizes of the ring.

It was already observed from flow visualization that at $Z = 3d_j$ the vortex ring was fully-formed and slightly tilted forward, into the cross-flow. In order to quantitatively investigate how far from the exit a fully-formed vortex ring is produced, traces of point-wise velocity versus time histories were obtained at twelve different locations (from the exit to $Z = 4d_j$) along the jet exit centerline. The data shown in Figure 4.7 indicate that the ring is basically fully-formed at $Z = 3d_j$ downstream from the exit. Up to $Z = 2d_j$, the velocity traces look like jet flow movement without forming a real vortex ring. The velocity traces between $2d_j$ and $3d_j$ are interpreted in this study as showing the formation processes of a vortex ring. When a fully-formed vortex ring is passed through the hot-film probe, the velocity profile became symmetric about a peak velocity, e.g. at $Z = 3d_j$, as shown in Figure 4.7. After the ring passed downstream of $Z = 3d_j$, no change of its configuration in a continuing formation process was not observed. Whitehead (1968) numerically investigated the vortex ring formation process up to five exit diameters. He suggested that $2d_j$ is enough distance to obtain a fully-formed vortex ring. Sallet and Widmayer (1974) observed by photographic study that the rings are formed within about $2.5d_j$ from the vortex generator. They also noted that the early development of fully-formed vortex rings seems to be independent not only of the piston speed but also holds true for vortices formed with different piston velocity profiles.

Table 4.3 presents some comparative data on vortex ring formation. In Table 4.3, Reynolds number is defined as $Re_j = \overline{u}R_j/\nu$, where R_j is the exit radius, $\overline{u}$ is exit flow velocity and ν is the kinematic viscosity of the medium used. Whitehead (1968) used the peak pulsating velocity, while the mean pulsating velocity was selected as $\overline{u}$ in Sallet and Widmayer's (1974) and the present study. It appears that there is no significant effect of cross-flow on vortex ring formation under the present experimental range.

The procedure by which the tilted angle of the vortex ring was measured is as followings. First, the time difference between the peak velocities at the front

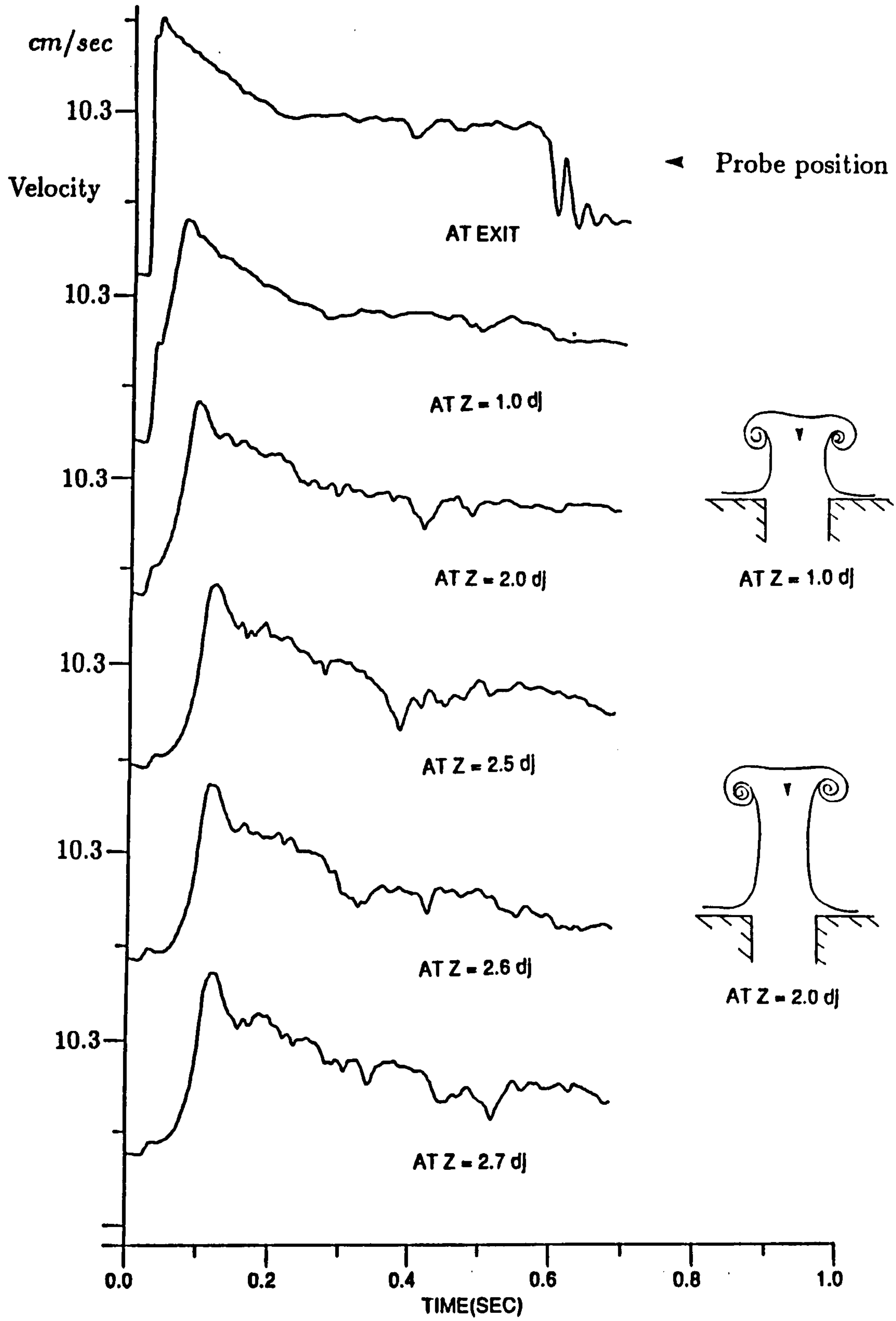

Figure 4.7 Sequence of traces showing fully-formed vortex ring

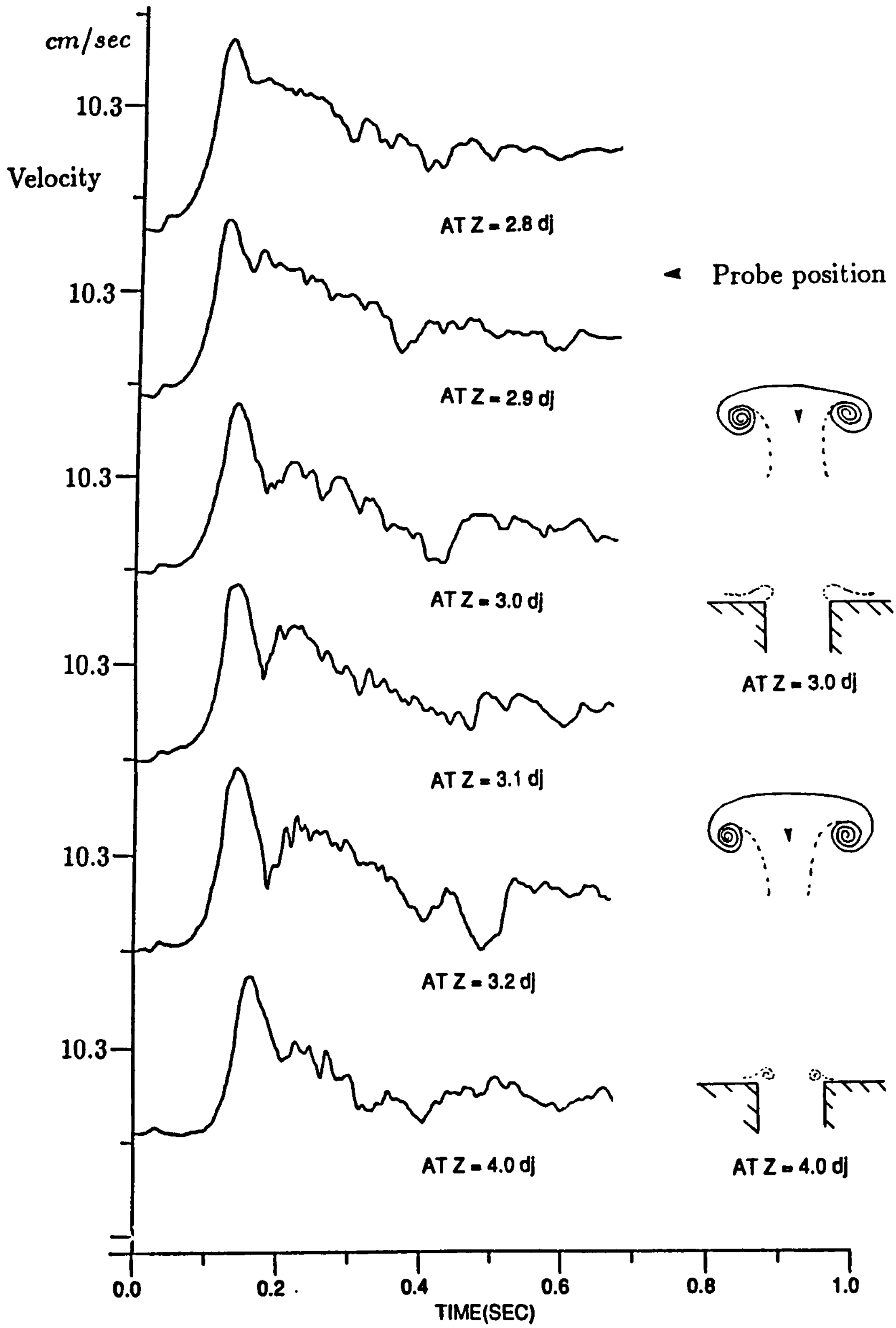

Figure 4.7 Continued

Table 4.3

Comparison of data on distance required for vortex ring formation

	Ring formation distance	**Re$_{\mathbf{ex}}$**	**Medium**
Whitehead (1968)	$2.0d_j$	533	*Computation*
Sallet et al. (1974)	$2.5d_j$	8010 − 12250	*Experiment in air*
This study	$3.0d_j$	800	*Experiment in water*

inner edge and rear inner edge of the ring is measured, and then the tilted vertical distance can be calculated based on the instantaneous translational velocity at that point. The horizontal distance between the front inner edge and the rear inner edge is obtained from the velocity traces. Then, the tilted angle can be calculated by the ratio of vertical and horizontal distances. The tilted angle measured by this method was 2.6° at $Z = 3d_j$. The center position of the ring was $X = 0.40d_j$ at $Z = 3d_j$, which means the ring moved slightly toward the streamwise direction due to the cross-flow.

The coordinates for the velocities in the tilted vortex ring are represented in Figure 4.8. Since the actual direction of the translational and rotational velocities are defined in Figure 4.8, and tilted with respect to the mean velocities in the laboratory-coordinate system, the tilt angle between the directions of mean vertical velocity and of translational velocity should be considered to calculate the translational and rotational velocity.

Some typical velocity-time traces along the radial positions at $Z = 3d_j$ are presented in Figure 4.9. These velocity-time traces were obtained by using a $\theta =$ 0° hot-film probe. Figure 4.9(c) shows a typical velocity-time trace when the center of the vortex ring pass by the hot-film probe. The dip is caused by the rotational motion of the ring core. Figure 4.9(e) and (h) indicate the velocity peak at the inner edge of each ring core. Figure 4.10 schematically represents ten radial positions $X = const.$ corresponding to each location shown in Figure 4.9.

In the relatively far downstream, $Z = 7d_j$, and $Z = 10d_j$, the characteristic features of a vortex ring are very similar to those at $Z = 3d_j$ except more movement in the streamwise direction. For example, the X-coordinates of the ring center at $Z = 7d_j$ and $Z = 10d_j$ are $X = 1.24d_j$ and $X = 1.78d_j$ from the exit centerline,

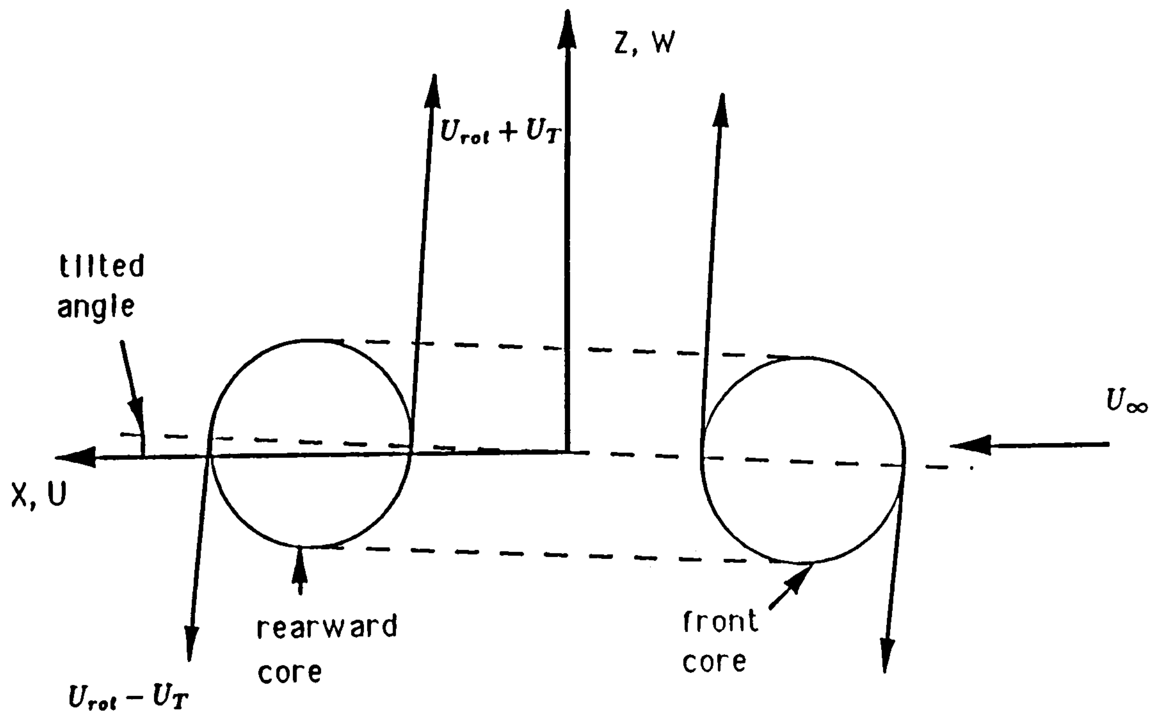

Figure 4.8 Coordinate system of a tilted vortex ring

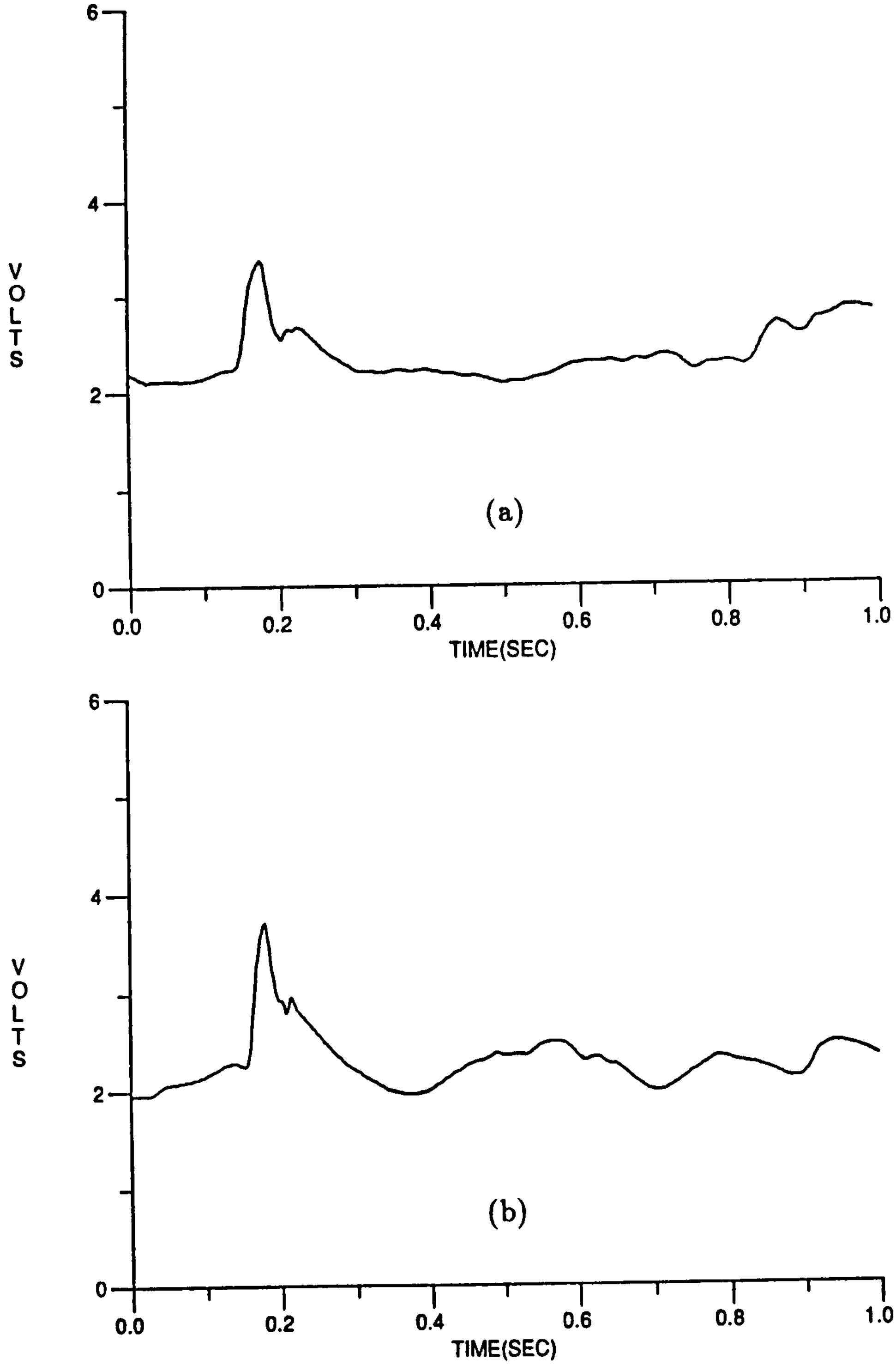

Figure 4.9 Some typical velocity (voltage) traces at $Z = 3d_j$, see locations shown in Figure 4.10 for corresponding stations

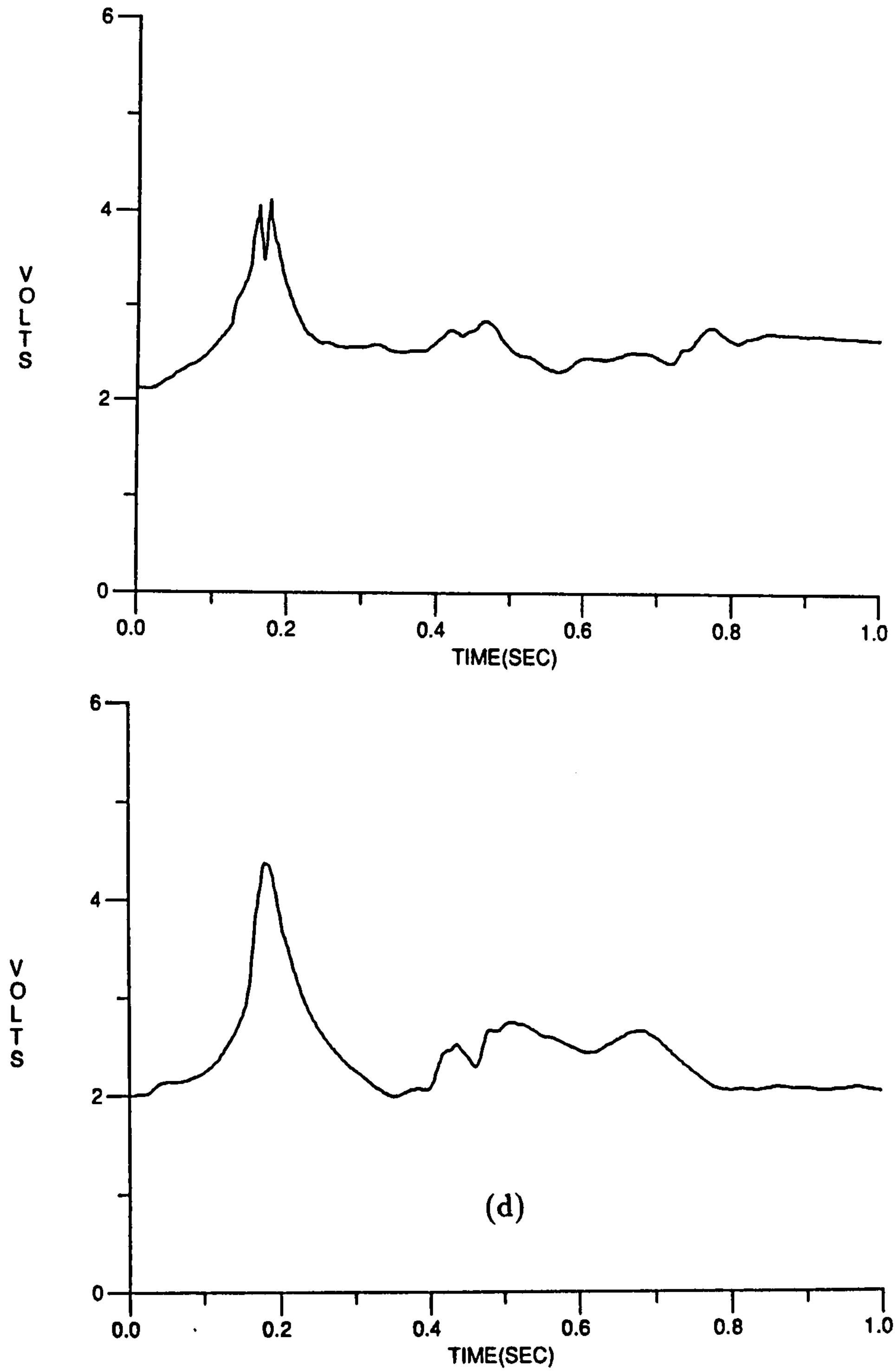

Figure 4.9 Continued

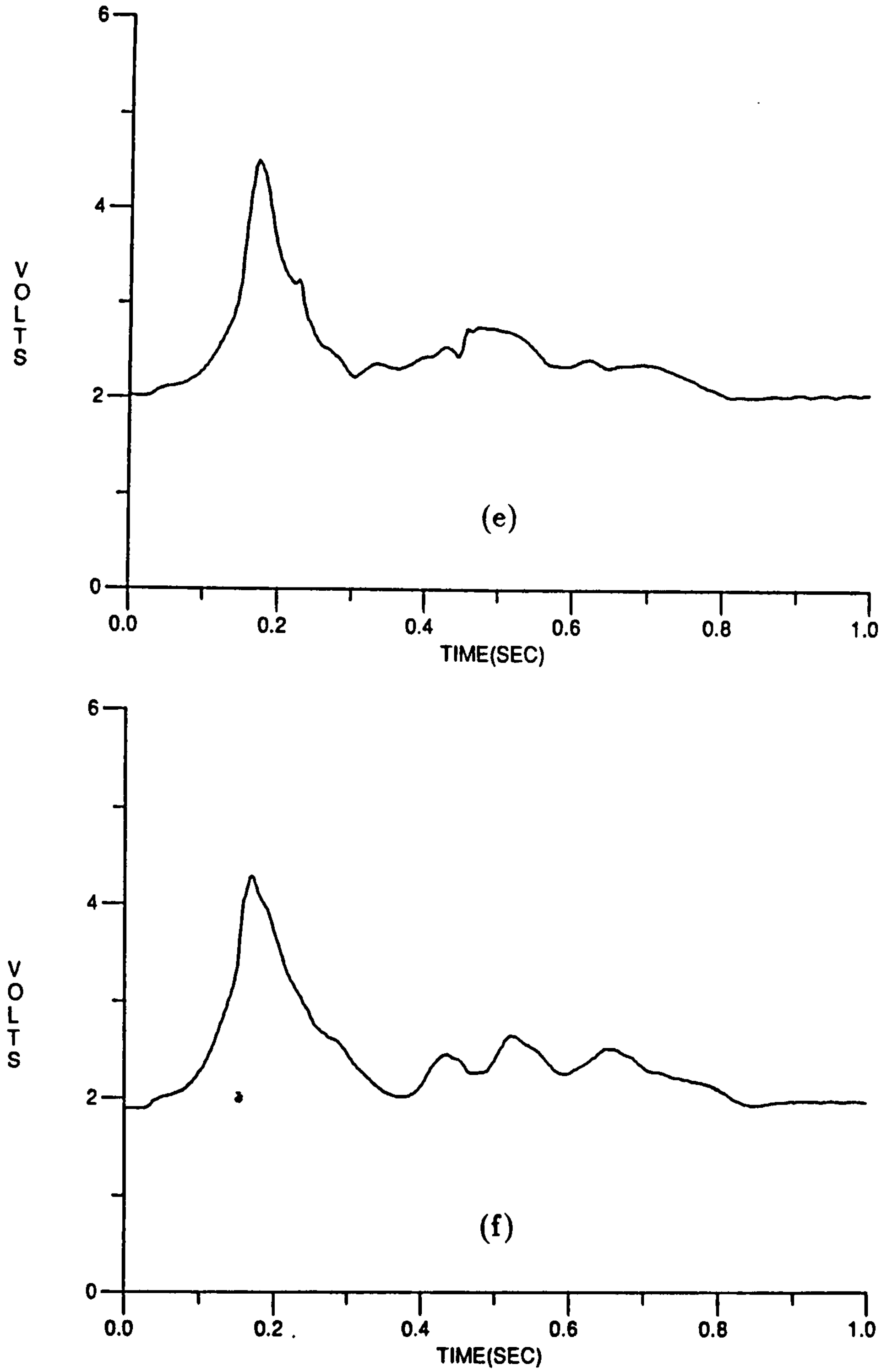

Figure 4.9 Continued

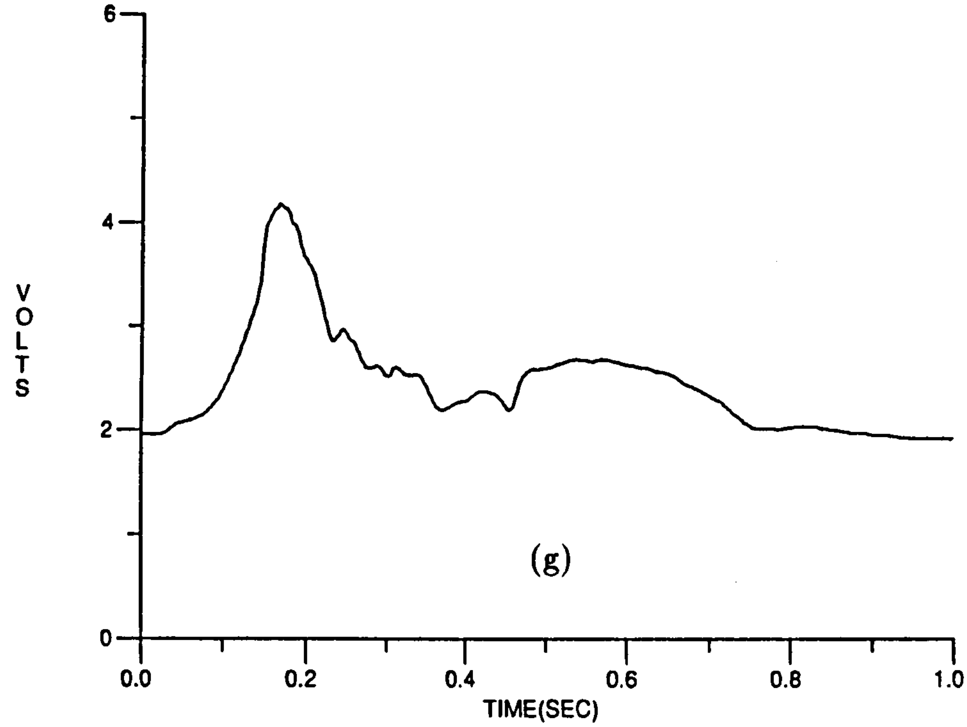

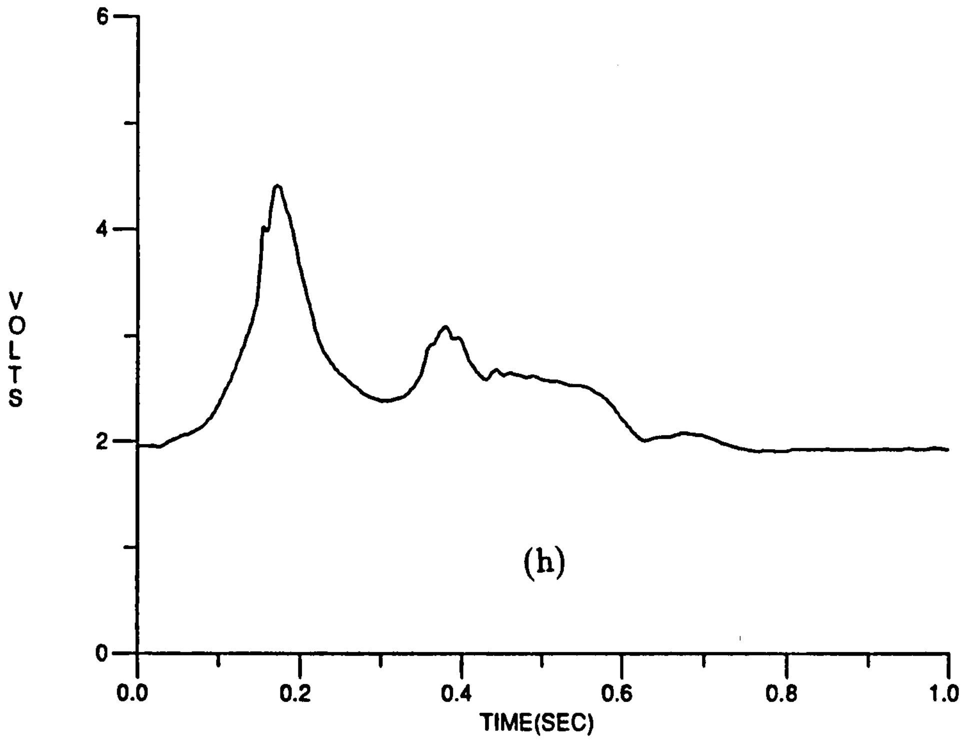

Figure 4.9 Continued

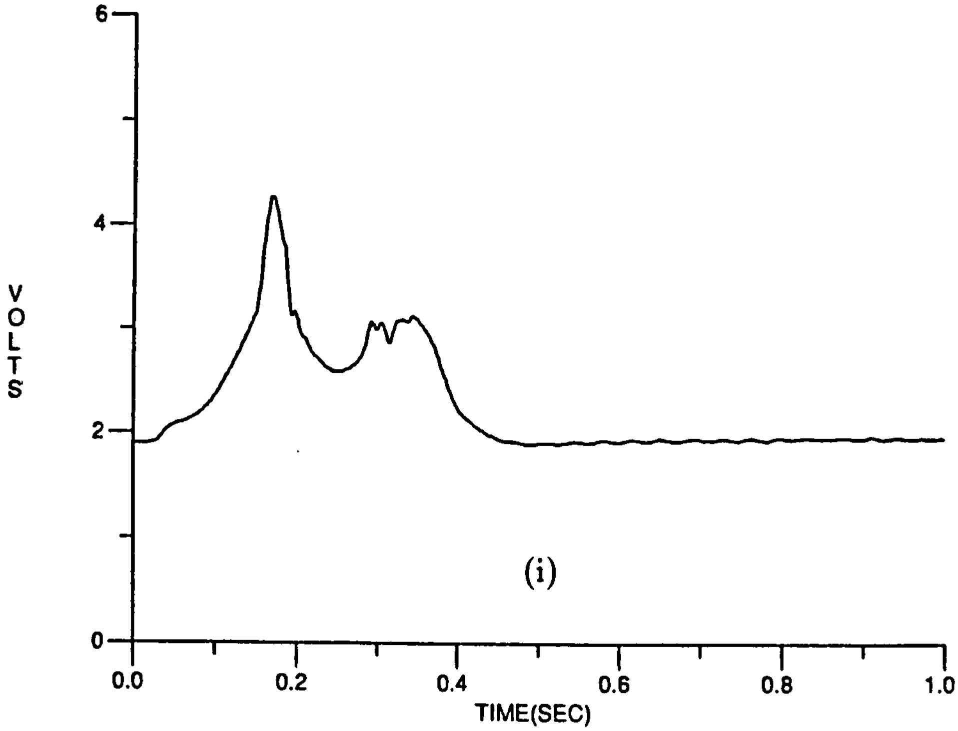

(i)

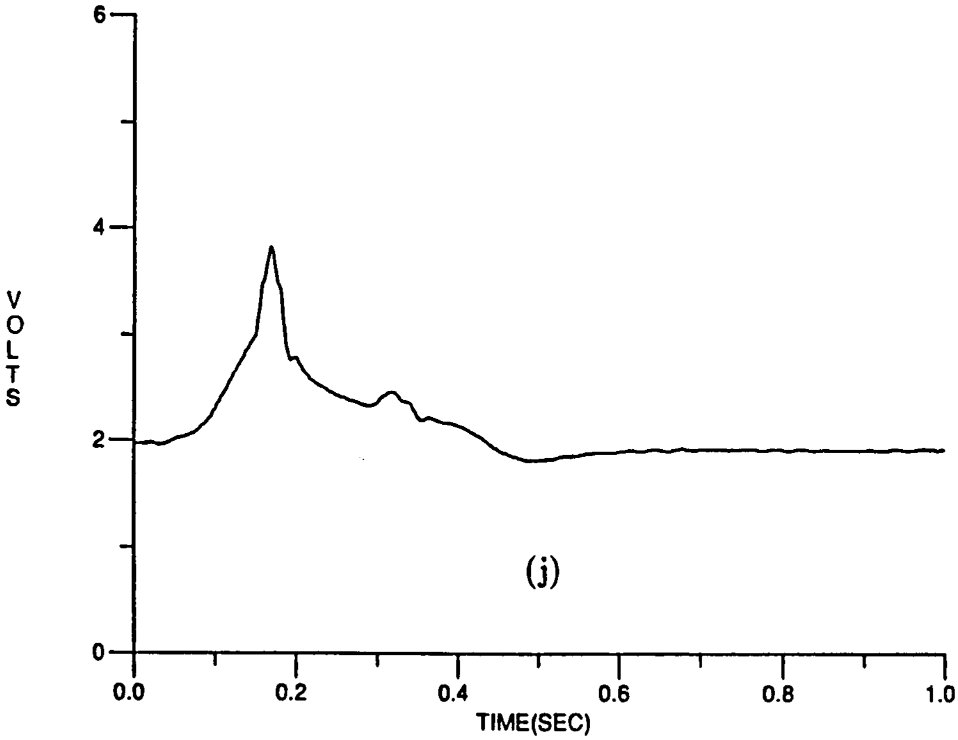

(j)

Figure 4.9 Continued

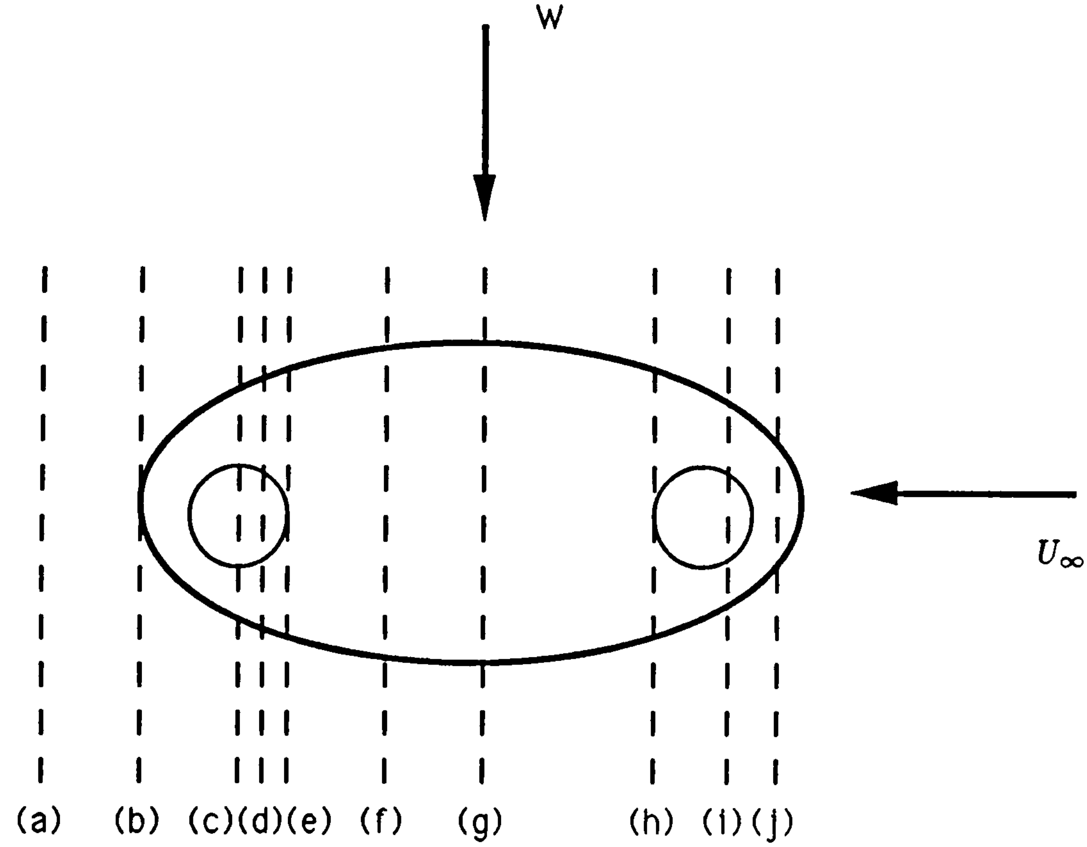

Figure 4.10 Ring sections indicating the locations of traces in Figure 4.9

respectively.

The test was repeated from four to eight times at each of three downstream locations to ensure the repeatability of the results and to obtain the averaged data in the analysis. Hot-film measurements at $Z = 10\ d_j$ were much more difficult to conduct than at $Z = 3\ d_j$ due to the varied ring trajectory from run to run. It was already mentioned before that some data scattering were observed relatively far downstream in the flow visualization results. It appears that this data scatter might be due mainly to slightly non-uniform pulsations developed by the combination of solenoid valve and frequency generator. Therefore, great care was specially taken at these points measurement.

As mentioned earlier, the $\overline{W}$ and $\overline{U}$ velocity components were used to analyze the detailed quantitative data. First, the total circulation can be found by measuring $\overline{W}$ as a function of Z along the vortex ring centerline and integrating the area under the curve. Second, the core diameter can be measured by the $\overline{U}$ profile along the core centerline at $X = R$. Third, in order to construct the axial velocity profile along $Z = 0$ the peak values of $\overline{W}$ were taken at various radial locations.

Figure 4.11 represents some typical non-dimensional velocity profiles $\overline{W}/U_T$ and $\overline{U}/U_T$ versus the non-dimensional coordinate Z/D (D is a ring diameter) which is corresponding to the time that a vortex ring passes through the probe at $Z = 3d_j$. As mentioned above, the ring was surveyed along nine radial positions. Here, the distribution of each velocity component is transformed to the steady coordinate system by converting t-coordinate to Z-coordinate using $Z = U_T \cdot t$, where U_T is the instantaneous translational velocity of the ring at a measuring point. The time t was measured with an interval of 0.00167 sec, which means that there

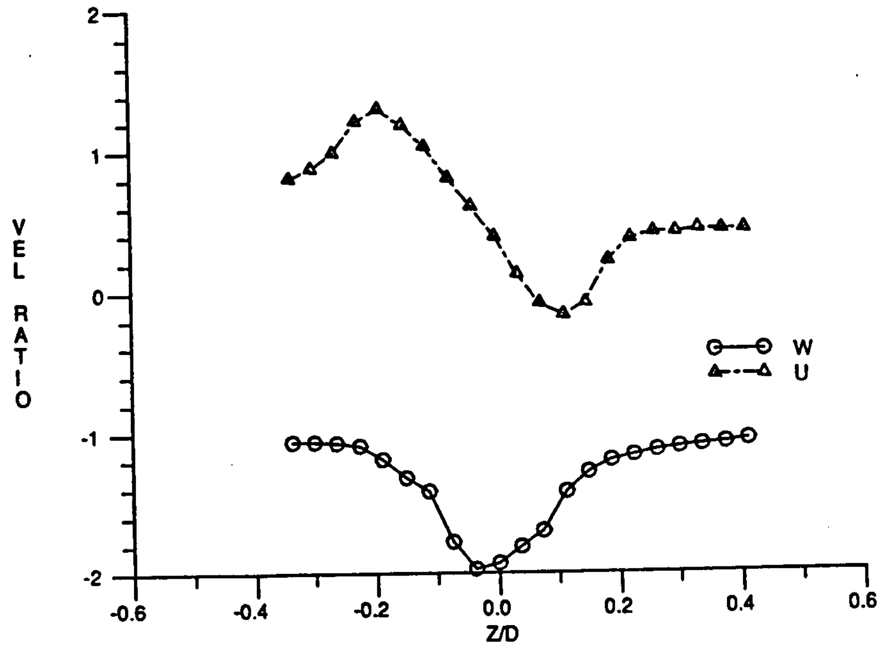

(a) $X = 1.276\ R$

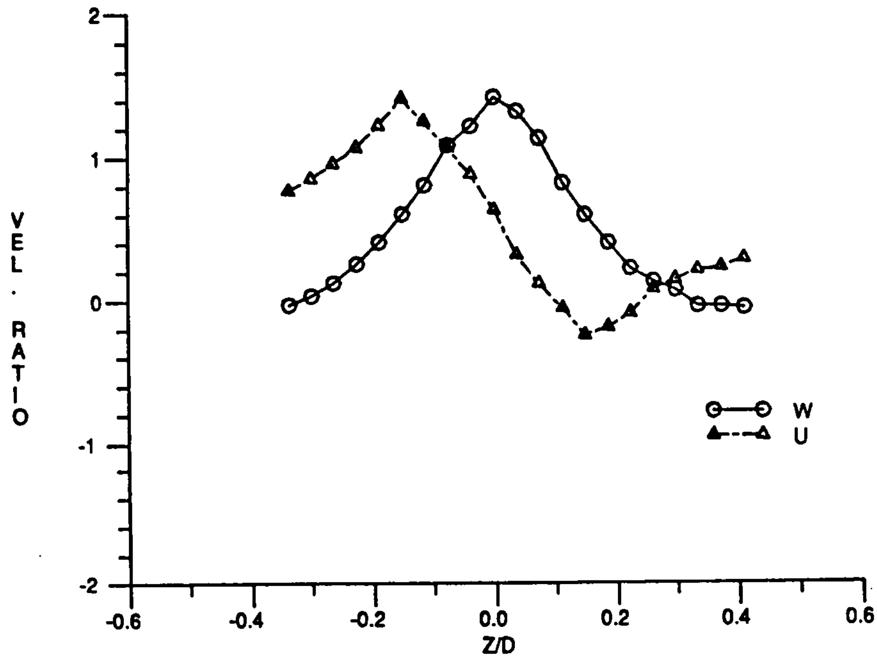

(b) $X = 0.944\ R$

Figure 4.11 Typical velocity flowfield within a ring at $Z = 3d_j$

(a) through (i) are schematically explained in Figure 4.11 (j)

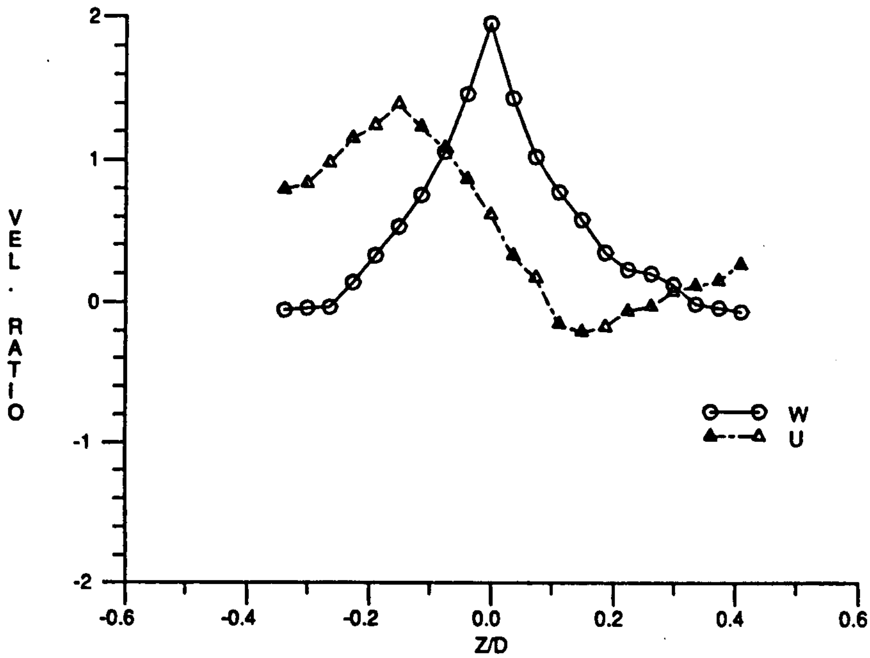

(c) $X = 0.722\ R$

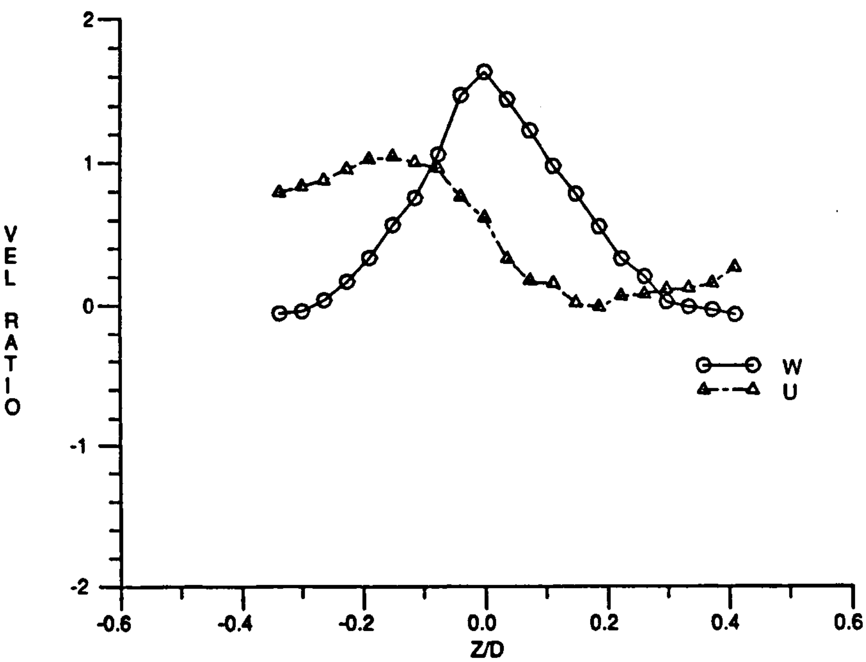

(d) $X = 0.276\ R$

Figure 4.11 Continued

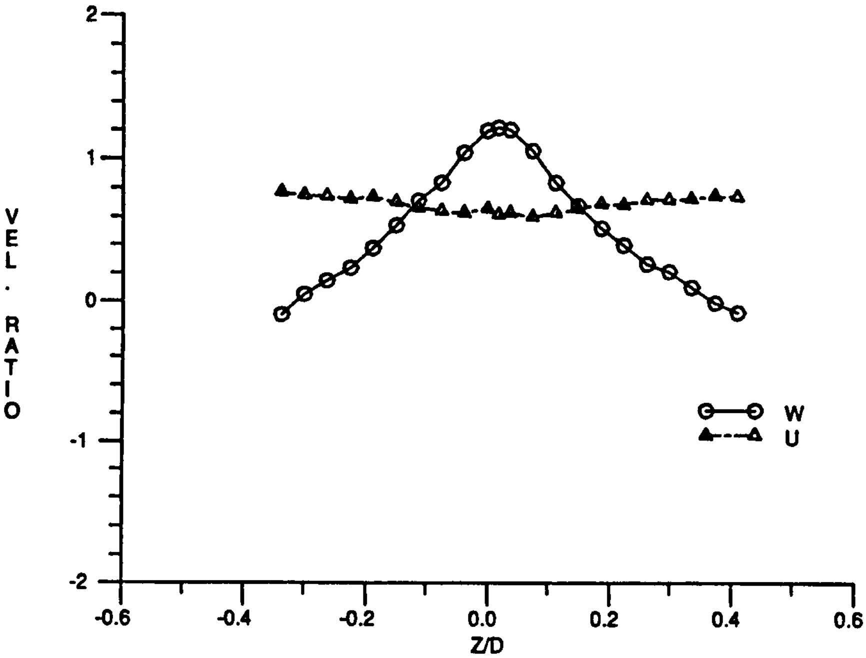

(e) $X = 0$

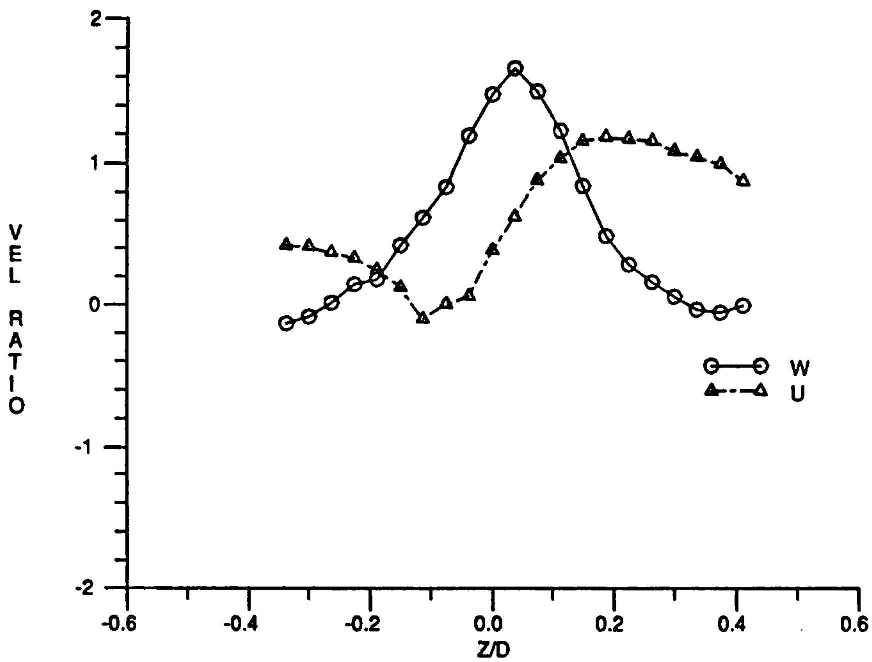

(f) $X = -0.349\ R$

Figure 4.11 Continued

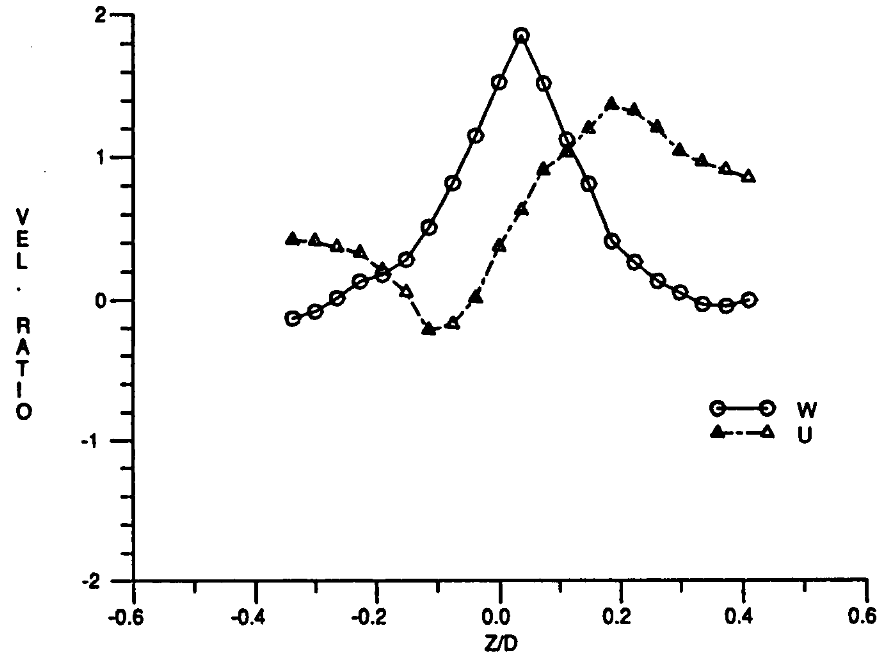

(g) $X = -0.698\ R$

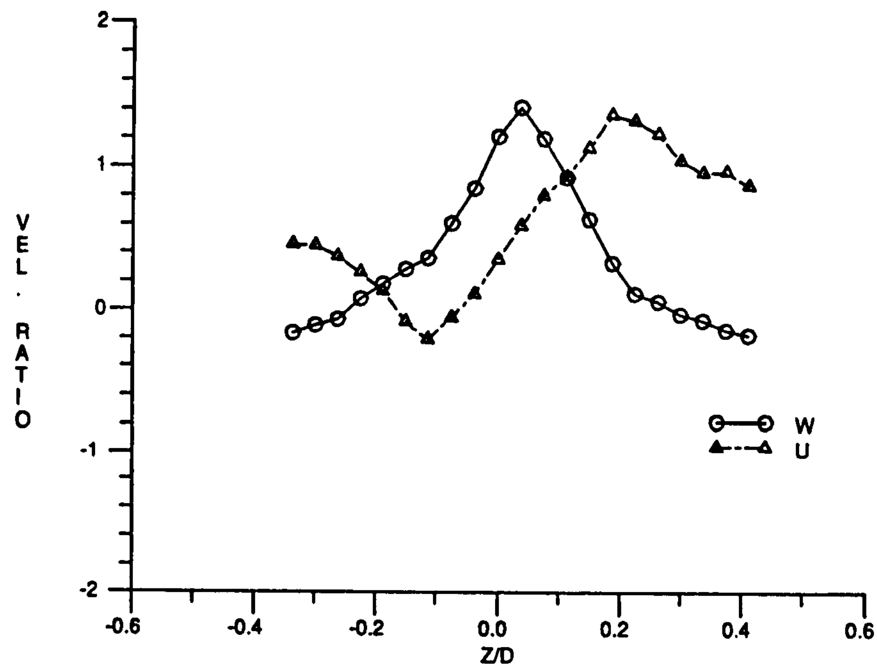

(h) $X = -0.888\ R$

Figure 4.11 Continued

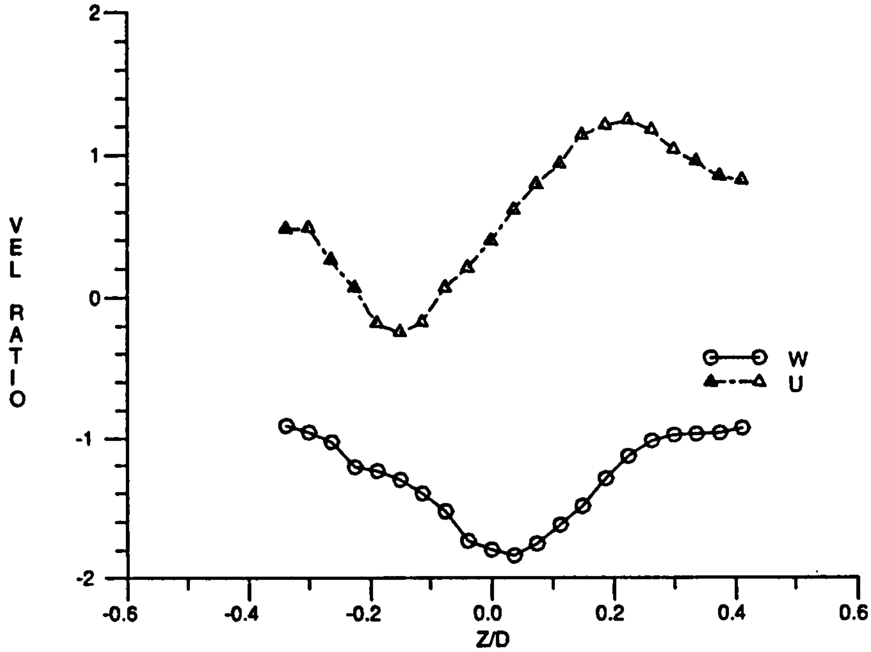

(i) $X = -1.285\ R$

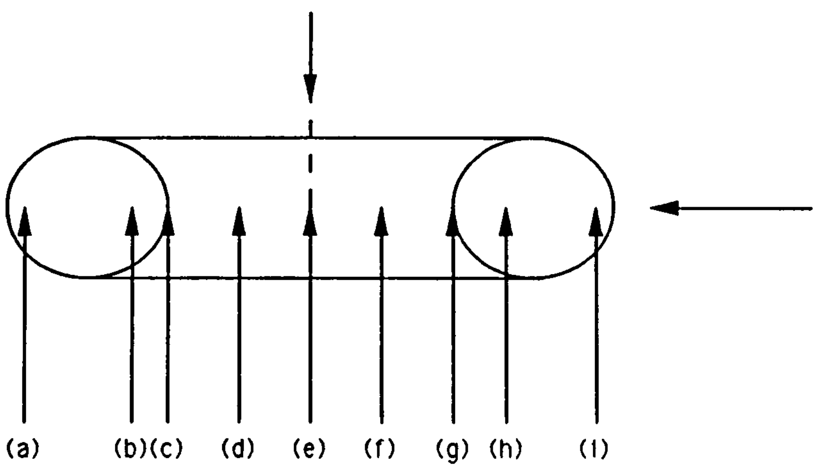

Tilting is neglected in this diagram and
(a) through (i) represent the radial positions
that probe is located.

(j)

Figure 4.11 Continued

are about 600 data points during a 1 *sec* pulsation. The translational velocity U_T and the ring diameter D at that measuring point were selected as characteristic parameters. The above assumption of steady approximation indicates that the properties of the vortex ring are not significantly changed by the cross-flow and/or wakes during the time that a vortex ring passes by a measuring point. Since the hot-film probe cannot detect the negative velocity component, the negative velocity profiles in Figure 4.11 are resolved by flow visualization. The non-dimensional velocity profiles for each velocity component at $Z = 7d_j$ and $Z = 10d_j$ are similar to those at $Z = 3d_j$, except having different characteristic parameters.

Figure 4.12 shows a typical distribution of nondimensionalized axial(vertical) velocity, $\overline{W}/U_T$, versus X/R along the radial coordinates, $Z = 3d_j$, downstream location. The velocity profile can be easily constructed by the peak velocities obtained from the velocity components of Figure 4.11. In Figure 4.12, it is found that the ring is almost symmetric indicating the same ratio between core radius and ring radius at both upstream and downstream edges.

In order to determine the translational velocity, core diameter, ring diameter and circulation, several different ways can be adopted. Locations of vortex ring core centers were very carefully determined from traces like those of Figure 4.9(c). Near the core center, the probe was moved in small intervals of 0.0156 *cm* to be able to detect the core center position as accurately as possible. For example, the core diameter at $Z = 3d_j$ was repeatable to within a maximum ± 4 % as presented in Appendix C. Then, the inner edge and outer edge of the core were determined from the inner peak velocity point such as Figure 4.9 (d). The core radius between the position of peak velocity and core center was decided by assuming that the core is exactly circular in shape by having circular streamlines. It was confirmed that the core diameter obtained from the above method is equivalent to the distance

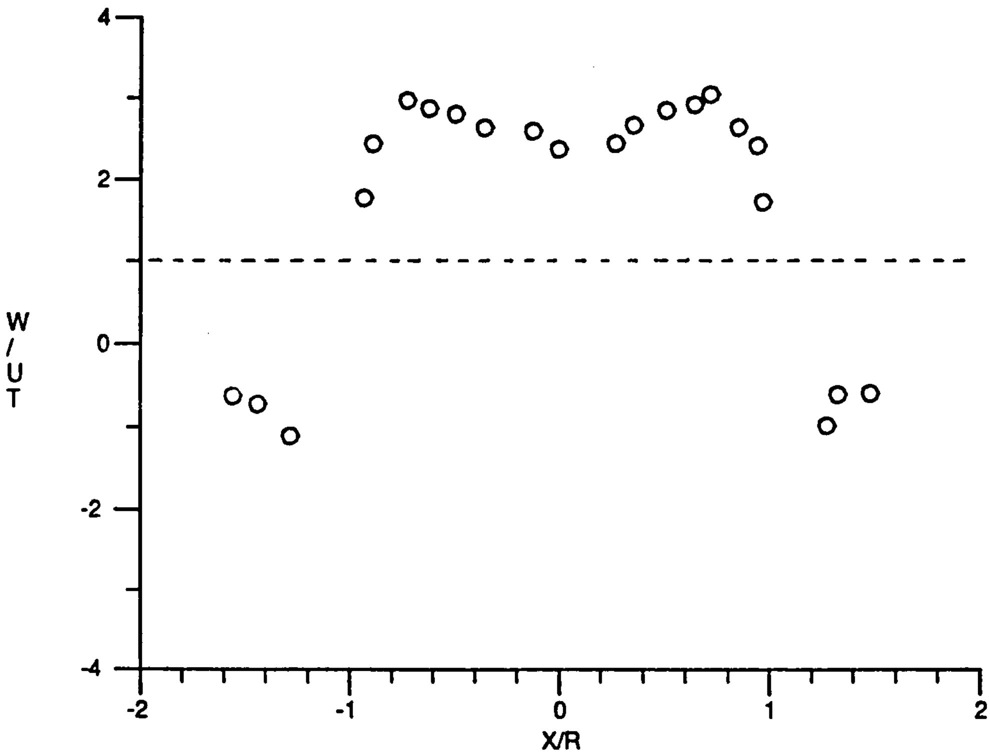

Figure 4.12 Axial velocity component along the radial distance at $Z = 3d_j$

between peak velocities of Figure 4.11 (h). The peak velocity at the inner edge, U_{ie}, is the sum of rotational velocity U_{rot} and the translational velocity U_T. Also, the outer edge velocity, U_{oe}, is the difference between U_{rot} and U_T. Therefore, the translational velocity and rotational velocity can be calculated using equations (2-39) and (2-40). The effective core circulation can be calculated from core rotational velocity by using equation (2-41). The total measured circulation were evaluated by integrating the velocity profiles $\overline{W}$ as a function of Z along the vortex ring centerline. Hence, we can calculate the amount of vorticity contained within the core in this case. Γ_c/Γ_m was estimated to be about 65.5 % at downstream locations.

Table 4.4 presents a summary of quantitative data obtained from hot-film experiments at three different downstream locations for $f = 1Hz$ pulsation. The Reynolds number based upon the ideal circulation, Re_{Γ_i}, was 3970 in this case. Γ_i indicates the initial ideal circulation calculated using the simplified slug model which is a predicted value. Γ_i was computed by using the following relation with the exit velocity profile of Figure 3.4 (a).

$$\Gamma_i = \frac{1}{2}\int_0^T \overline{u}^2(t)dt \qquad (4-4)$$

where $\overline{u}(t)$ is the mean pulsating velocity of the fluid ejected through the exit. Γ_m is the total measured circulation obtained from velocity profiles $\overline{W}$, as mentioned above, and Γ_c is the effective core circulation due to the rotational velocity of vortex core. The amount of measured circulation almost linearly decreased as the ring moved downstream.

We need to discuss here the relationships between measured core circulation and measured total circulation. Also, it is significant to highlight the discrepancy between the measured circulation and ideal circulation using a simple slug model.

Table 4.4

Quantitative data summary of vortex ring characteristics at $f = 1\ Hz$

Z	$3d_j$	$7d_j$	$10d_j$
Ring radius R, cm	1.080	1.250	1.397
Translational velocity $U_T, cm/sec$	9.635	9.162	8.471
Radius ratio a/R	0.294	0.279	0.268
Measured circulation $\Gamma_m, cm^2/sec$	38.526	35.183	33.631
Core circulation $\Gamma_c, cm^2/sec$	25.896	23.326	21.615
Ideal circulation $\Gamma_i, cm^2/sec$	39.879	39.879	39.879
Mean pulsating velocity $\overline{u}, cm/sec$	12.630	12.630	12.630
Reynolds number $Re = \frac{\Gamma_i}{\nu}$	3970	3970	3970
Tilting angle	2.6°	3.2°	3.3°
$ln(\frac{8R}{a}) - \frac{1}{4}$ in inviscid equation	3.054	3.106	3.146
Non-dimensional velocity $\tilde{U}$	3.610	4.411	4.919
X-coordinate of ring center	$0.40d_j$	$1.24d_j$	$1.78d_j$

Maxworthy (1977) noted that only about 50 % of the total circulation is contained within the core at high Re_M based on the exit velocity and exit diameter. This is contrasted with the present study and the theoretical result of Sallet and Widmayer (1974) who obtained 65.5 % and 71.5 % of concentration within the core, respectively. Maxworthy (1977) also found that the total measured amount of vorticity that appears downstream is very close to that predicted by a simple slug model at high Reynolds number (between 10^4 and 10^5). However, Didden (1977), using Laser Doppler Velocimeter data, observed that Γ_i underestimates the total measured circulation by 30 % to 60 % at low Reynolds numbers until $Re_M = 6.6 \times 10^3$. In this case, the piston velocity profiles were utilized to calculate Γ_i in equation (4-4). This also indicates that the simple slug model cannot be a good parameter to describe the formation process. Finally, it can be seen that the above relationships between core and measured circulations depend on a given piston motion and/or pulsed frequency and exit geometry. In Didden's experimental work, the measured circulation is much larger than the ideal circulation using the simple slug model. Didden (1979) explained in detail the factors that can increase the circulation above the ideal value as follows; one is due to a much larger velocity, than the exit velocity, near the sharp corner at the nozzle exit for short times, the other is due to the accelerated core flow for constant piston velocity by a thicker internal boundary layer. In the present study, the total measured circulation was very close to the ideal circulation using the slug model. At $Z = 10\ d_j$, it deviated only 15.67 % from the ideal quantity.

The mean pulsating velocity was calculated from the trace of velocity vs time, see Figure 3.4 (a). Since only the time period of the peaked area is responsible for generating a vortex ring, peaked area (velocity vs time) was utilized to calculate mean pulsating velocity. In general, the growth of ring diameter agrees well with data obtained from visual observations, Figure 4.4, using dye flow visualization. It is found that the ratio between the core and ring radius was almost constant as the ring moves downstream. This fact conflicts with equation (4-1) which says that $R(t) \cdot a^2(t)$ is constant under the fact that the vorticity moves with the fluid in an incompressible flow and inviscid flow.

The tilting angle slightly increased as the ring moves downstream, however, it was observed that the tilting angle of a ring was tending to be restored to the horizontal orientation far downstream (near the free surface) even though it was not quantitatively confirmed by a hot-film probe experiment. The average maximum tilting angle was estimated to be approximately 3° to 4° during the vortex ring movement in the cross-flow. In order to confirm that the expression for translational velocity by inviscid theory, equation (2-6), is comparable to the quantity from real vortex ring measurements, a non-dimensional velocity was introduced as.

$$\tilde{U} = \frac{U_T 4\pi R}{\Gamma_m} \qquad (4-5)$$

The above equation is equivalent to $ln(8R/a) - 1/4$ in the inviscid equation. Under the present experimental range, the deviations from the real value was reasonably small. This makes sure that the results using the equation (2-6) for $A = 1/4$ for a viscous vortex ring is accurate within to 30 %.

4.4 Experimental Ring Trajectories

Figure 4.13 shows the trajectories of the vortex rings at various frequencies for different jet to cross-flow velocity ratios. Trajectories at high frequencies were not predicted due to the difficulty in measuring the ring diameters. These vortex ring trajectory data exhibit two fundamental results. First, the penetration level at low frequency is much higher than at high frequency for the same velocity

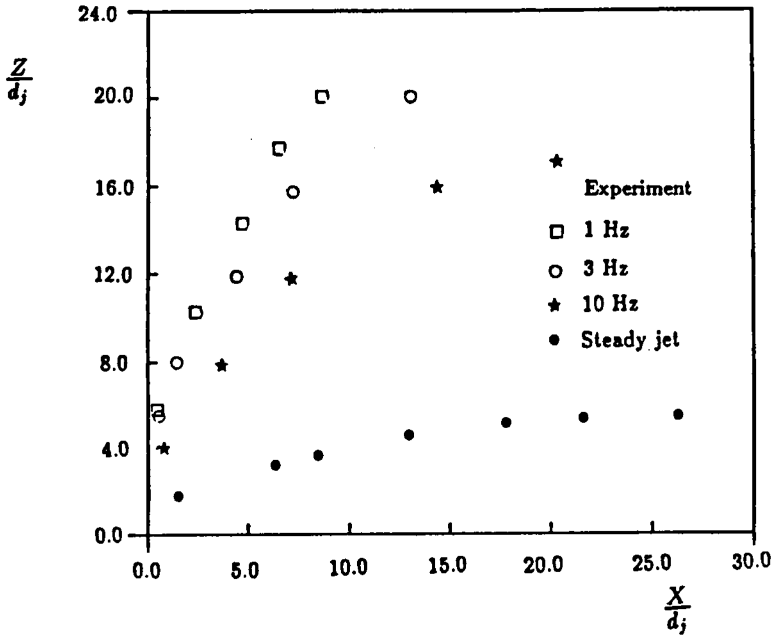

(a) $\frac{\overline{U}_j}{U_\infty} = 1.5$

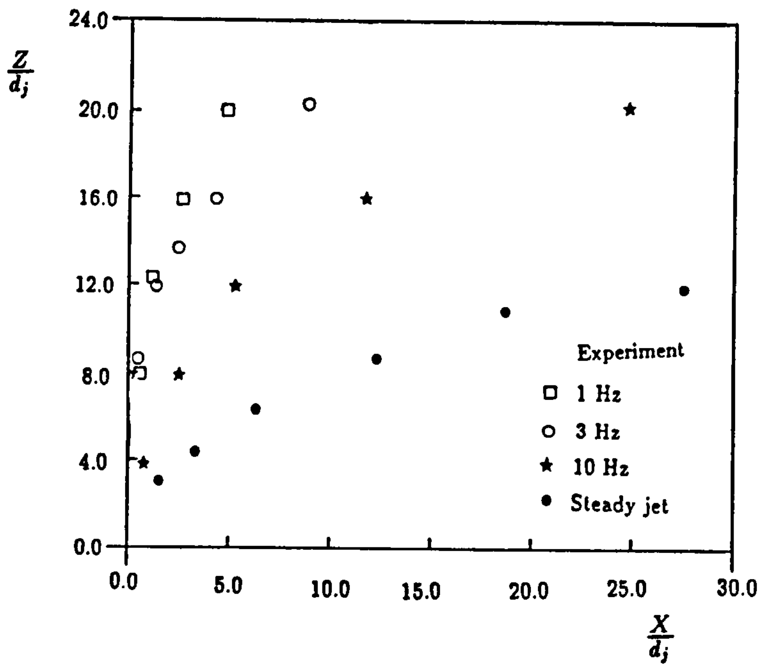

(b) $\frac{\overline{U}_j}{U_\infty} = 3.0$

Figure 4.13 Penetration Trajectories of vortex rings in the cross-flow for various pulsating frequencies ratio. Second, as the cross-flow velocity increases (at the same jet velocity) the penetration height decreases for the same frequency ratio.

4.5 Dimensional Analysis for Trajectories

If the data for the different velocity ratios ($\overline{U}_j/U_\infty$) are collapsed on to a single line, simple power law relations describing the steady and pulsating jet trajectories in the cross-flow can be easily determined. This approach is composed of the combination of dimensional analysis and fundamental physical arguments about the characteristics of each jet flow. First of all, an appropriate length scale associated with the jet flow characteristics needs to be defined.

4.5.1 Steady Jet Trajectory

Trajectories of centerline velocity points for steady flow were also shown in Figure 4.13. The jet motion in a cross-flow depends primarily on its initial momentum flux ($\overline{U}_j^2$), and the cross flow momentum flux (U_∞^2). An effective velocity ratio can be described as the square root of the ratio of momentum fluxes

$$R = \left[\int_{Aj} \rho_j \overline{U}_j^2 ds / \rho_\infty U_\infty^2 A_j \right]^{1/2} \qquad (4-6)$$

If the ideal state is assumed, equation (4-6) may be reduced simply to the ratio of the jet to cross-flow velocities, $R = \overline{U}_j/U_\infty$. It may be expressed as a function of the following independent parameters.

$$g(\overline{U}_j, d_j, U_\infty, \nu, X, Z, t) = 0 \qquad (4-7)$$

Dimensional analysis yields

$$g\left(\frac{\overline{U}_j^2}{U_\infty^2}, \frac{Z}{d_j}, \frac{\overline{U}_j d_j}{\nu}, \frac{X}{d_j}\right) = 0 \qquad (4-8)$$

For steady jets, the effect of Reynolds number on the jet trajectory is negligible (Haniu and Ramaprian, 1989).

Therefore, the penetration height will be a function of the following two dimensionless parameters.

$$\frac{Z}{d_j} = F[\left(\frac{\overline{U}_j^2}{U_\infty^2}\right), \left(\frac{X}{d_j}\right)] \qquad (4-9)$$

Haniu and Ramaprian (1989) introduced a momentum length scale l_m defined as

$$l_m = (\frac{\overline{U}_j^2}{U_\infty^2})d_j \qquad (4-10)$$

The experimental results for the trajectories of different velocity ratios can be represented in logarithmic scales. In the current study all the data approximately collapsed on the curve based on the scaled coordinates.

$$\frac{Z}{l_m} = a(\frac{X}{l_m})^b \qquad (4-11)$$

where $a = 0.92$ and $b = 0.57$.

4.5.2 Pulsating Jet Trajectory

In the present study, the dependent parameter of major importance is the penetration of the vortex ring in the vertical direction. As for the steady case, it can be described by the following function.

$$g\left(\overline{U}_j, d_j, U_\infty, U_T, \nu, Z, X, t, f, l_d\right) = 0 \qquad (4-12)$$

where f is a pulsating frequency, l_d is the separation distance between adjacent vortex rings. Dimensional analysis gives

$$g\left(\frac{U_\infty^2}{\overline{U}_j^2}, \frac{f l_d}{U_T}, \frac{\overline{U}_j d_j}{\nu}, \frac{Z}{d_j}, \frac{X}{d_j}\right) = 0 \qquad (4-13)$$

in which the Strouhal number is defined as

$$St \equiv \frac{f \cdot l_d}{U_T} \qquad (4-14)$$

For pulsed jets, such as in current study, the Reynolds number based on the pulsation velocity may be relevant in the formation of vortex rings. However, since no efforts have been made on the Reynolds number effect in this study, it will be omitted from here on.

Therefore, the penetration can be described by

$$\frac{Z}{d_j} = G[\left(\frac{f \cdot l_d}{U_T}\right), \left(\frac{\overline{U}_j^2}{U_\infty^2}\right), \left(\frac{X}{d_j}\right)] \qquad (4-15)$$

The vertical trajectory of a vortex ring jet is expected to depend on Strouhal number based upon translational velocity and separation distance between adjacent vortex rings and the momentum flux $(\overline{U}_j^2/U_\infty^2)$.

In order to correlate the pulsating jet flow penetration for different jet to freestream velocity ratios and various frequencies, a modified frequency-momentum length scale is introduced similar to the steady case (Vakili et al., 1991).

$$l_{fm} = d_j\left(\frac{\overline{U}_j^2}{U_\infty^2}\right)\left(1 + \frac{kU_T}{l_d f}\right) \qquad (4-16)$$

where k is a similarity parameter to be determined through a least square fit of the data. The data of Chassaing et al. (1974) was used to be fitted by a regression process. In this calculation the k resulted was 3.8. The result in Figure 4.14 indicates a good correlation of all the various data. This correlation is being considered as a new similarity coordinate. From the match between experimental results and similarity analysis, we can estimate that the effect of excitation on the trajectory is more prevalent than the ratio of momentum flux $(\overline{U}_j^2/U_\infty^2)$ for the

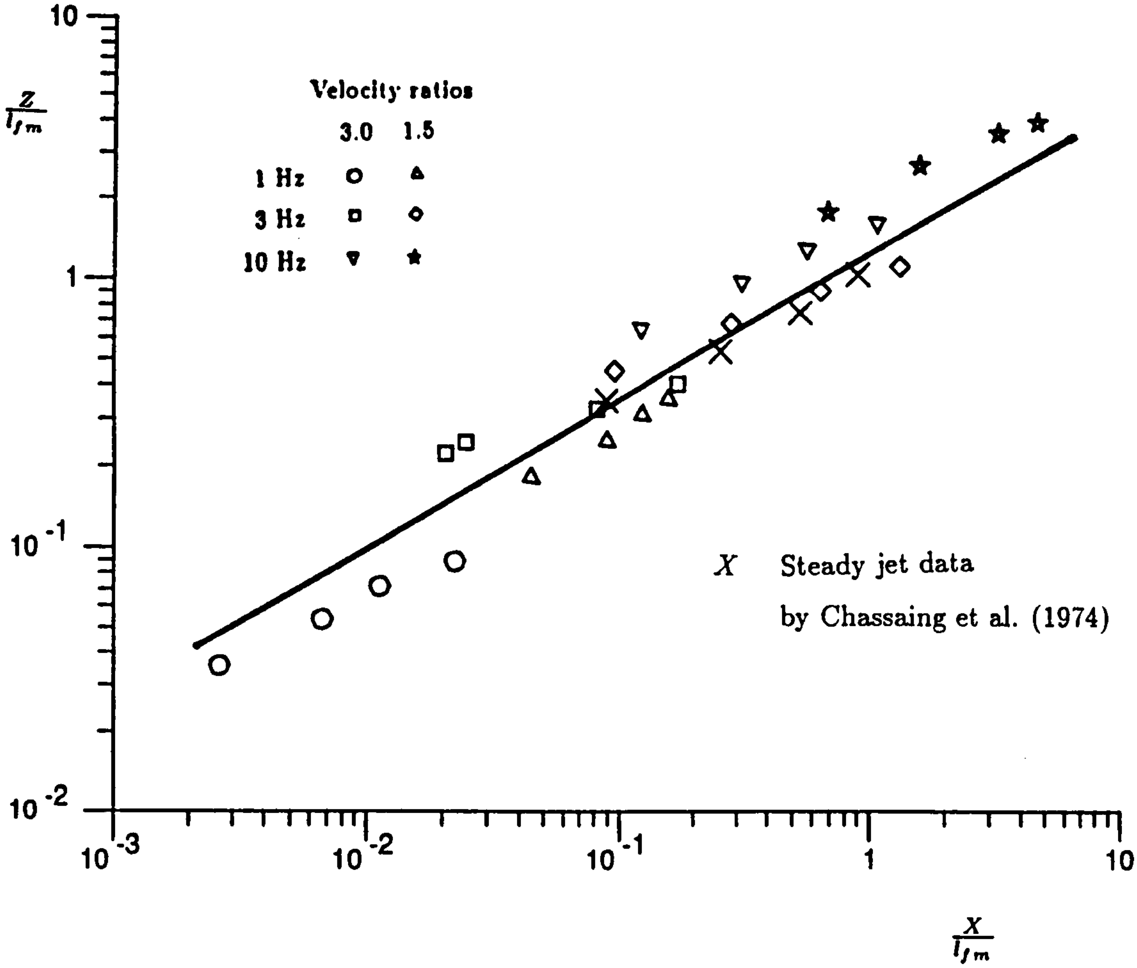

Figure 4.14 Collapsed trajectory for pulsating jet

pulsating jet. It has been well known that the momentum flux ratio $(\overline{U}_j^2/U_\infty^2)$ is one main parameter correlating the characteristics of the steady jet in a cross-flow.

4.6 Bifurcating Rings

An interesting observation was obtained in the course of investigating the vortex rings in cross–flow. At very low cross-flow speeds $(\overline{U}_j/U_\infty = 6.7)$ and for 10 Hz frequency the vortex ring trajectory is not stable and the rings are actually moving into the cross-flow and in the upstream direction, in the lateral directions and the various orientations. The resulting flow looks like a blooming jet obtained by combined axial and orbital excitations (Lee & Reynolds(1984)). This experimental result confirmed that a blooming jet(due to nonuniform vorticity distribution) can be made by axial excitation and a certain geometry to provide passive excitation in a resonance mode of the pipe without active orbital excitation. The divergence angle of the blooming vortex rings was smaller than that of Lee and Reynolds because of the cross–flow effect. The basic mechanism of a blooming jet and a bifurcating jet is discussed by Parekh et al. (1985) and Lee & Reynolds (1984). The prominent mechanism for these particular excited jets is known to be due to the interaction of the vortex with the initial conditions.

In 1955, Anderson(1955) published one paper on the structure and velocity of the periodic vortex ring pattern of a Pfeifenton (Pipe Tone) jet. He also found different and very unusual vortex flow patterns which showed an amazing and reproducible splitting of the jet into two distinct circular vortex trains (bifurcating jet) around 1150 cps. At that time, he just described the phenomena without explanation of the mechanism. This confirms that it is possible to obtain the bifurcating and/or blooming jet by passive excitation or certain geometric condition without active orbital excitation as shown in this experiment. It is important to understand how the rings are generated in the excited jets.

4.7 Additional Observations

As the vortex rings approach a solid boundary, some characteristic flow phenomena are generally observed (Cerra & Smith, 1983). The first feature is the rebounding and reversal in the trajectory of the rings. The second characteristic of the flow interaction observed is the formation of a sheet of secondary vorticity along the outer perimeter of the ring close to the solid boundary. The third characteristic of the flow interaction is a sudden transition to turbulence after the rings impacted the solid boundary.

During this study, it was observed that a vortex ring is unstable very near the free surface due to the interaction between the surface and the ring propagating into the cross-flow. Each vortex ring rebounded from the free surface due to the generation of a boundary layer and then disintegrated, moving into the cross-flow. It was also discovered that low velocity ratio ($\overline{U}_j/U_\infty$) make the ring unstable due to strong momentum flux in the freestream direction.

As indicated by Cerra & Smith (1983), it is observed that the behavior of vortex rings impacting a free surface is similar to that of vortex rings impacting a solid boundary. Saffman (1979) noted that a boundary layer is supposed to be formed at the free surface and it is much weaker than one at a solid surface because of the difference in slip conditions; the free surface is dominated by a surface tension force instead of a non-slip condition.

5. Numerical Methods

The purposes of this numerical study were to better understand the interaction between vortex rings and cross-flow and to explain the flow visualization experiments.

Vortex rings in cross-flow represent typical three-dimensional, unsteady vortical flow. Vortex rings are usually characterized by low viscosity and concentrated regions of vorticity embedded in an otherwise potential flow. This fact allows one to discretize the compact regions of vorticity into an assembly of vortices. Vortex methods simulate this type of flow by discretizing and tracking the discretization in a Lagrangian reference frame. A simplified flow simulation was carried out using the discrete vortex method. That is, a vortex ring was modeled by a vortex filament with a number of nodes in the shape of a torus. A discrete number of nodes which lie along the vortex centerline enable one to be able to solve the deformation problem. These points are located along a given initial configuration of the ring, along with the initial conditions on the translational velocity of each node. The basic assumptions in the Lagrangian vortex methods are inviscid and incompressible flows.

Each node on the vortex ring moves with the local velocity. Therefore, once the induced velocities are known, the movement of each node during a small time step can be calculated by multiplying the local induced velocity by the time step. For this calculation, a second order Runge-Kutta method was used to iterate on the position of the nodes and therefore improve the accuracy of the computations.

The original code was written and developed by Parekh et al. (1988) based upon the discrete-vortex method. This code was developed to investigate the effects of excitation frequency and amplitude on the spreading of the bifurcating jet. They used an analytical function to describe the source flow and discrete, computational vortex elements to represent the vortex rings formed at the jet exit. It was modified for our study to investigate the effect of cross-flow on the vortex rings depending on axial frequency. We compute the evolution of vortex rings in the cross-flow. The advantage of the vortex method is that no finite mesh or grid is required, and this Lagrangian nature makes it unconditionally stable to convection.

As mentioned before, the vortex ring moves into the cross-flow due to the impulse of jet flow and the self-induced motion of each vortex ring element along the circumference of the ring. The effect of the vortex filament on the cross-flow is assumed to be negligible. Aref and Flinchem (1984) estimate that the dominant mechanism in this kind of interacting flow is the advection of the filament by the background, and the neglected terms are much smaller provided that the diameter of the vortex is negligible compared to the characteristic length scale of the background flow. Jet source flow was introduced in order to simulate the impulse due to jet flow. The jet flow was modeled by a semi-infinite cylindrical vortex sheet. It will be discussed in detail later.

5.1 Formulation and Numerical Scheme

The equations which govern an incompressible, inviscid flow are Euler's equations;

$$\frac{D\boldsymbol{u}}{Dt} = \frac{\partial \boldsymbol{u}}{\partial t} + \boldsymbol{u} \cdot \nabla \boldsymbol{u} = -\nabla p \qquad (5-1)$$

and the continuity equation,

$$\nabla \cdot \boldsymbol{u} = 0 \qquad (5-2)$$

expressing the conservation of momentum and mass, respectively.

This computational experiment was conducted to simulate an incompressible flow field of vortex rings where only a small portion is rotational. It will be convenient to describe the above governing equations in terms of the vorticity variable. Equation (5–1) can be rewritten in terms of the vorticity by taking the curl.

$$\frac{D\boldsymbol{\omega}}{Dt} = \frac{\partial \boldsymbol{\omega}}{\partial t} + \boldsymbol{u} \cdot \nabla \boldsymbol{\omega} = \boldsymbol{\omega} \cdot \nabla \boldsymbol{u} \qquad (5-3)$$

where

$$\boldsymbol{\omega} = \nabla \times \boldsymbol{u} \qquad (5-4)$$

Equation (5–3) is called the vorticity transport equation which explains that the vorticity moves along a particle path while it is being tilted and stretched with the evolving strain field ($\nabla \boldsymbol{u}$). Therefore, the term ($\boldsymbol{\omega} \cdot \nabla \boldsymbol{u}$) exists only in a three-dimensional flow.

The vorticity distribution from m filaments or tubes with circulation Γ in three-dimensional flow is given by (Sarpkaya, 1989)

$$\boldsymbol{\omega}(\boldsymbol{r}, t) = \sum_{i=1}^{m} \Gamma_i \int_c \gamma_i \left[\boldsymbol{r}, \boldsymbol{r}_i(s,t)\right] \frac{\partial \boldsymbol{r}_i(s)}{\partial s}\, ds \qquad (5-5)$$

where $\boldsymbol{r}(s,t)$ describes the space curve of the filament centerline in terms of a parameter along the curve (s). The distribution function γ_i is assumed to have the following form

$$\gamma_i(\boldsymbol{r} - \boldsymbol{r}_i) = \frac{1}{\sigma_i^3} f\left(\frac{|\boldsymbol{r} - \boldsymbol{r}_i|}{\sigma_i}\right) \qquad (5-6)$$

where the notation of Leonard is used with σ_i (the core radius of filament i).

Once the vorticity distribution is known, the velocity induced by the vorticity in a bounding region can be calculated from the integration of Equations (5–2) and (5–4). Batchelor (1967) shows that, using vector identity and $\nabla \cdot \boldsymbol{u} = 0$,

$$\nabla^2 \boldsymbol{u} = -\nabla \times \boldsymbol{\omega} \qquad (5-7)$$

$\boldsymbol{u}$ can be expressed as

$$\boldsymbol{u}(\boldsymbol{r}) = -\frac{1}{4\pi}\int \frac{(\boldsymbol{r}-\boldsymbol{r}')\times\boldsymbol{\omega}(\boldsymbol{r}')d\boldsymbol{r}'}{|\boldsymbol{r}-\boldsymbol{r}'|^3} + \nabla\phi \qquad (5-8)$$

where ϕ is the velocity potential related to the homogeneous solution of the above equation which is required to satisfy the boundary conditions as follows:

$$\boldsymbol{u}\cdot\boldsymbol{n}\Big|_{\text{body surface}} = 0 \qquad (5-9)$$

$$\lim_{|\boldsymbol{r}|\to\infty} = \boldsymbol{u}(\boldsymbol{r},t) = \boldsymbol{U}_\infty \qquad (5-10)$$

The resultant velocity will be split into two components based upon the uniqueness of the decomposition of a vector field.

$$\boldsymbol{u}_R = \boldsymbol{u}_s(\boldsymbol{r},t) + \boldsymbol{u}_I \qquad (5-11)$$

where $\boldsymbol{u}_s(\boldsymbol{r},t)$ is a solenoidal field which is a solution of Equation (5–7) and $\boldsymbol{u}_I$ is an external irrotational velocity. The induced velocity of the filament at point $\boldsymbol{r}(s)$ on the axis is given by Biot-Savart law

$$\boldsymbol{u}_s(\boldsymbol{r},t) = -\frac{1}{4\pi}\iiint \frac{(\boldsymbol{r}-\boldsymbol{r}')\times\boldsymbol{\omega}(\boldsymbol{r}',t)}{|\boldsymbol{r}-\boldsymbol{r}'|^3}\, dV(\boldsymbol{r}') \qquad (5-12)$$

With the thin filament approximation, it reduces to

$$\boldsymbol{u}_s(\boldsymbol{r},t) = -\frac{\Gamma}{4\pi}\int_c \frac{[\boldsymbol{r}(s,t)-\boldsymbol{r}'(s',t)]\times\partial\boldsymbol{r}'/\partial s'}{|\boldsymbol{r}(s,t)-\boldsymbol{r}'(s',t)|^3}\, ds' \qquad (5-13)$$

where s describes the coordinate along the lines. The result of this locally induced velocity which in the limit of a vortex filament becomes infinite yields a logarithmic singularity in the self-induced velocity known as a general feature of a curved vortex filament in the three-dimensional flow. This causes an infinite velocity of the filament and also causes instabilities. In order to eliminate this velocity singularities, numerous cut off schemes have been introduced (see, Sarpkaya (1989)).

Another difficulty with the Biot-Savart method will be the number of operations for the induced velocity calculation, since CPU time increases considerably as the number of vortex elements increase.

The modification of Biot-Savart law is achieved by Rosenhead's (1931) method which was modified later by Moore and Saffman (1972). The evolution equation for a three-dimensional, space curve $\boldsymbol{r}_i(s,t)$ $(i = 1, 2, ..., N)$ with N vortex filaments is considered. The induced velocity at a point, $\boldsymbol{r}$, is then calculated as:

$$\boldsymbol{u}_s(\boldsymbol{r},t) = -\sum_j \frac{\Gamma_j}{4\pi} \int \frac{[\boldsymbol{r}(s,t) - \boldsymbol{r}_j(s',t)] \times \partial \boldsymbol{r}_j(s',t)/\partial s'}{\left(|\boldsymbol{r}(s,t) - \boldsymbol{r}_j|^2 + \alpha\sigma_j^2\right)^{3/2}} \, ds' \qquad (5-14)$$

where $\alpha\sigma_j^2$ is a measure of the vortical flow region. σ_j is the core radius and can be changed depending on the distribution of vorticity. A vortex ring with a Gaussian vorticity distribution can be simulated by a single vortex filament with the above vorticity distribution, and then the self-induced velocity has the correct value for $\alpha = 0.413$, (Leonard (1985)). Therefore, this value was used for our numerical simulations. Here, α is a parameter related to the fraction of circulation within the radius $r = \sigma$ (Moore and Saffman (1972)).

To consider the influence of vortex filament i on filament j, $\alpha\sigma_j^2$ can be replaced by $\alpha(\sigma_i^2 + \sigma_j^2)/2$ as follows:

$$\boldsymbol{u}_s(\boldsymbol{r}_i,t) = -\sum_j \frac{\Gamma_j}{4\pi} \int \frac{[\boldsymbol{r}_i(s,t) - \boldsymbol{r}_j(s',t)] \times \partial \boldsymbol{r}_j(s',t)/\partial s'}{\left[|\boldsymbol{r}_i(s,t) - \boldsymbol{r}_j|^2 + \alpha'(\sigma_i^2 + \sigma_j^2)\right]^{3/2}} \, ds' \qquad (5-15)$$

As mentioned before, $\alpha = 0.413$ satisfies the translational velocity of a vortex ring as far as σ_i is much less than the ring radius.

Since a vortex line always consists of the same fluid particle and moves with the fluid in an incompressible flow, the core radius σ is kept uniform along each filament but varies with time to conserve a constant volume. It can be expressed by

$$\frac{d}{dt}(\sigma_i^2 R_i) = 0 \qquad (5-16)$$

where $R_i(t)$ is the instantaneous length of the vortex ring filament i. The size of the core radius can vary with the local stretching of the ring. The total circulation assigned to a vortex segment at each simulation remains constant.

5.2 Calculation Procedures

The dynamics of vortex rings in cross-flow is characterized by a three-dimensional configuration which has variations with location, size and shape. For this simulation, a set of nodes (vortex elements) are incorporated to represent each vortex ring. The spacing between node points was sufficiently small so that length scales of interest would be represented accurately.

For numerical purposes, it is assumed that the core radius of each filament is much smaller than the ring radius. Therefore, the distribution of vorticity is almost Gaussian in magnitude and the vortex lines are parallel at each cross section normal to the filament tangent vector.

Since each vortex element moves with the local fluid velocity, the self-induced velocity field obtained from Equation (5–15) can be integrated in time to find the subsequent location of the vortex elements. Again using Equation (5–15) the velocity field at the next time can be computed and this procedure repeated.

The total velocity induced by a multi-segment filament is obtained by summing the induced velocity of each filament. The detail calculations for the induced velocity by all the vortex filaments are given in Parekh (1988).

The first vortex ring is generated at the origin with the initialization of frequency and time integration parameters. Then, subsequent vortex rings are generated at given distances depending on axial frequency. The circulation of each filament has the same magnitude and is determined by circulation conservation laws. The flux of vorticity in the boundary layer (sheet) is given by $U^2/2$. It is also assumed that the vorticity convected from the cylindrical sheet equals the vorticity convected by the discrete filaments. The conservation constraints show

$$\frac{\Gamma}{\Delta t} = \frac{\gamma^2}{2} \qquad (5-17)$$

in which Γ is the circulation of each ring filament, γ is the circulation per unit length of the cylindrical vortex sheet, and Δt is the time interval between generation of vortex ring filaments.

At each time step, the total velocity at each node due to the combined effects of the vortex segments, jet source flow and external flow is calculated. Both the spatial and the temporal integration are carried out with the second-order, Runge–Kutta method, with the node points being advanced in time

$$x' = x(t) + u(t)\frac{\delta t}{2} \qquad (5-18)$$

$$x(t + \Delta t) = x(t) + u'(t)\delta t \qquad (5-19)$$

in which $x(t)$ and $u(t)$ indicate a node position and velocity at time t, and δt is the time increment between time steps which is typically an order of magnitude smaller than Δt.

5.3 Simulation of Jet Source Flow

The viscosity effect was not incorporated in this numerical experiment. As a result, it is not possible to obtain the characteristics of three-dimensional ring configuration, including shape, position and size. In order to complement this defect, jet source flow was introduced whose flow from a semi-infinite cylindrical vortex sheet is similar to that of an viscous jet issuing from the jet in a wall (Parekh, 1988).

The formulation presented below follows the work of Parekh (1988). In order to simulate a jet flow, the Biot-Savart integral is applied to a semi-infinite, cylindrical vortex sheet of finite thickness. The jet velocity function can be derived to define the mean jet flow. The simple form of equation is given by

$$u_r(\overline{r},\overline{z}) = \frac{\gamma}{2\pi\sqrt{\overline{\nu}}} I(\overline{\eta}) \qquad (5-20)$$

and

$$\begin{aligned} u_z(\overline{r},\overline{z}) = \frac{\gamma}{2\pi\overline{\rho}} \Bigg[\frac{\pi}{2} \left\{ \frac{(2-\overline{\rho})}{\sqrt{1-\overline{\mu}^2}} + \overline{\rho} \right\} \\ - \frac{\overline{z}}{\sqrt{\overline{\nu}}} \Bigg\{ \frac{2}{\sqrt{1+\overline{\eta}}} K(1-m_1) \\ + (\overline{\mu}-\overline{r}) T(\overline{\mu},\overline{\eta}) \Bigg\} \Bigg] \end{aligned} \qquad (5-21)$$

where

$$\overline{r} \equiv \frac{r}{R},$$

$$\overline{z} \equiv \frac{z}{R},$$

$$\overline{\sigma} \equiv \frac{\sigma}{R},$$

$$\overline{\nu} \equiv 1 + \overline{r}^2 + \overline{z}^2 + \alpha\overline{\sigma}^2,$$

$$\overline{\eta} \equiv \frac{2\overline{r}}{\overline{\nu}},$$

$$m_1 \equiv 1 - \frac{(1-\overline{\eta})}{(1+\overline{\eta})},$$

$$\overline{\rho} \equiv 1 + \overline{r}^2 + \alpha\overline{\sigma}^2,$$

$$\overline{\mu} \equiv \frac{2\overline{r}}{\overline{\rho}},$$

$$I(\overline{\eta}) \equiv \int_0^{\pi} \frac{\cos\theta}{\sqrt{1-\overline{\eta}\cos\theta}}\, d\theta,$$

$$T(\overline{u},\overline{\eta}) \equiv \int_0^{\pi} \frac{\cos\theta}{(1-\overline{u}\cos\theta)\sqrt{1-\overline{\eta}\cos\theta}}\, d\theta$$

The detail derivation of Equations (5–20) and (5–21) and integration scheme based upon the fourth-order Newton–Cotes method are described in Parekh (1988).

The semi-infinite sheet of vorticity extends from $-\infty$ to the origin as shown in Figure 5.1. Its axis represents the jet centerline, and the end of the sheet represents the jet exit. Here, it is assumed that the cylindrical sheet effects the motion of the filaments but there is no effect of the filaments on the cylindrical sheet. The trajectory of each filament is determined by the total velocities induced by each filament, jet source function and by a cross-flow. The sheet maintains a cylindrical configuration and it is not moved due to the filaments since the cylindrical sheet corresponds to a mean flow whose centerline is determined only by the position of a physical nozzle.

5.4 Simulation of Roll-Up of Vortex Ring

In the previous numerical algorithm, the first filament representing a vortex ring is created at the jet exit and subsequent filaments are periodically generated according to the specified excitation. To better understand the formation process of a vortex ring with excitation, the scheme was modified to simulate the shear layer dynamics. Multiple-filaments are used to represent each physical vortex ring while considering non-uniformity in the vorticity distribution within a filament.

Although the motion of vortex rings in cross-flow should be three-dimensional,

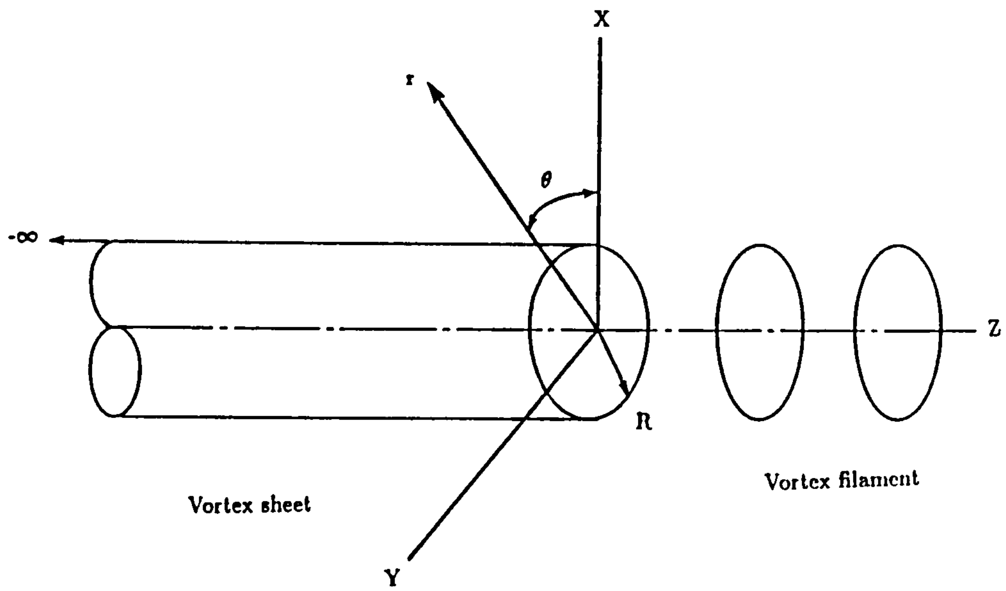

Figure 5.1 Schematic view of numerical model

the experiments show that there is no strong asymmetry in the non-interacting vortex rings. The current simulation of axisymmetric shear layers would be sufficient to predict the effect of cross-flow on the formation process of vortex rings.

In order to take into consideration the effect of cross-flow including viscosity on the roll-up of vortex rings, the random vortex element techniques coupled with simulation of the multiple-filament vortex ring are adopted.

When a fluid motion is impulsively started from rest, the vorticity should be produced on the solid boundary to get rid of any slip velocity. Initially, the slip velocity is generated by the potential flow. To simulate the vorticity within the boundary layer, Chorin (1978) introduced the vortex sheet method that vortex sheets are created along the wall to satisfy the no-slip boundary condition. In this case, the strength of vortex sheets produced to satisfy the no-slip boundary condition is calculated using

$$\Gamma = -\int \overline{u}_s \cdot d\overline{s} \qquad (5-22)$$

where $\overline{u}_s$ is the slip velocity which is equivalent to the initial freestream velocity and $\overline{s}$ is in the tangential plane at the wall.

Since the random vortex method is well documented in the literature, see Chorin (1978, 1980) for details of the method, we will concentrate here on the additional features of this study, i.e., the coupling between vortex sheet method and the simulation of shear layer roll-up. First of all, Chorin's numerical algorithm using the vortex sheet method to approximate the solution of boundary layer equations needs to be summarized.

The first step is to assume that the vortex sheets move according to the discrete approximation to the Euler equations;

$$\xi_t + (\overline{U} \cdot \nabla)\xi = 0 \qquad (5-23)$$

$$\xi = -u_z \tag{5-24}$$

$$u_x + w_z = 0 \tag{5-25}$$

Discrete approximations of these equations become

$$x_i^{m+1} = x_i^m + \Delta t \cdot u_i^m \tag{5-26}$$

$$z_i^{m+1} = z_i^m + \Delta t \cdot w_i^m \tag{5-27}$$

where

$$u_i^m = U_\infty(x_i^m) - \frac{1}{2}\xi_i - \Sigma_j \xi_j d_j,$$

$$w_i^m = -\frac{(I_1 - I_2)}{h},$$

$$d_j = 1 - \frac{|x_i^m - x_j^m|}{h},$$

$$I_1 = U_\infty(x_i^m + \frac{h}{2}) z_i^m - \Sigma_j^+ \xi_j d_j^+ \hat{z}_j^m,$$

$$I_2 = U_\infty(x_i^m - \frac{h}{2}) z_i^m - \Sigma_j^- \xi_j d_j^- \hat{z}_j^m,$$

$$d_j^+ = 1 - (\frac{|x_i^m + \frac{h}{2} - x_j^m|}{h}),$$

$$d_j^- = 1 - (\frac{|x_i^m - \frac{h}{2} - x_j^m|}{h}),$$

$$\hat{z}_j^m = min(z_i^m, z_j^m),$$

$$h = \textit{length of vortex sheet}$$

Σ *is over all vortex sheets* S_j *such that* $z_j^m \geq z_i^m$,

Σ_+ *is the sum over all vortex sheets* S_j *such that* $0 \leq d_j^+ \leq 1$,

Σ_- *is the sum over all vortex sheets* S_j *such that* $0 \leq d_j^- \leq 1$.

The second step is to simulate the viscous effect by adding an independent random variable η_i obtained from Gaussian distribution of mean zero and variance $2\nu t$. Therefore,

$$x_i^{m+1} = x_i^m + \Delta t \cdot u_i^m \tag{5-28}$$

$$z_i^{m+1} = z_i^m + \Delta t \cdot w_i^m + \eta_i \tag{5-29}$$

The third procedure is to satisfy the boundary conditions. The boundary condition at the edge of the boundary layer and the normal boundary condition is automatically satisfied. As mentioned above, the no-slip boundary condition is satisfied through a vorticity creation algorithm. Then, the above procedures are repeated by advancing Δt until the specified time is reached.

6. Numerical Results and Discussion

6.1 Overview of Numerical Results

Numerical results are presented to investigate the interactions between vortex rings and a cross-flow. The remarkable features of the trajectories and motion of vortex rings with different effects of cross-flow, circulation strength and Strouhal number are illustrated in the following.

In order to simulate the dynamics of vortex rings in a cross-flow, discrete vortex filaments are introduced to represent the vortex rings. Each vortex filament consists of 32 nodes of vortex elements, and each vortex segment moves under the action of the induced velocity of the other segments and the cross-flow. The uniform core radius ($\sigma = 0.1$) and non-uniform core radius ($d(\sigma_i^2 R_i)/dt = 0$) varying with the filament radius were used for this calculation. It was found that the variation of core radius has a very small effect on the motion of vortex rings in a cross-flow. The non-dimensional time step for the evolution of the vortex ring was typically below $\delta t = 0.08$. Twenty one different cases were tested to simulate as closely as possible the experimental results as shown in Table 6.1. The streamwise cross-flow is in the X-direction, Z is the vertical direction measured from the jet center. An initial vortex ring is generated at the origin, and then the next ring begins to evolve under the effect of the induced velocity.

Equations $(5-1)$ and $(5-2)$ describing the motion were non-dimensionalized by the characteristic parameters; the initial ring radius R as the reference length, the initial induced velocity U_{ind} as the reference velocity and the initial strength Γ_i as the reference strength. Note that when the background flow is zero the actual value to the experimental circulation (Γ) is not significant, since it is absorbed into a rescaling of the time and frequency variables. In the present calculations,

Table 6.1 Description of twenty one test cases for numerical experimentation

Case	St	Γ	cross flow	Parameter
1	0.35	1.0	*uniform*, 0.125	*frequency*
2	0.25	1.0	*uniform*, 0.125	*frequency*
3	0.17	1.0	*uniform*, 0.125	*frequency*
4	0.35	1.0	*uniform*, 0.250	*frequency*
5	0.25	1.0	*uniform*, 0.250	*frequency*
6	0.17	1.0	*uniform*, 0.250	*frequency*
7	0.35	1.0	*uniform*, 0.350	*frequency*
8	0.25	1.0	*uniform*, 0.350	*frequency*
9	0.17	1.0	*uniform*, 0.350	*frequency*
10	0.35	1.0	*uniform*, 0.125	*circulation*
11	0.35	2.0	*uniform*, 0.125	*circulation*
12	0.35	3.0	*uniform*, 0.125	*circulation*
13	0.25	1.0	*uniform*, 0.125	*circulation*
14	0.25	2.0	*uniform*, 0.125	*circulation*
15	0.25	3.0	*uniform*, 0.125	*circulation*
16	0.35	1.0	*uniform*, 0.125	*cross flow*
17	0.35	1.0	*mean shear*	*cross flow*
18	0.35	1.0	*exponential profile*	*cross flow*
19	0.25	1.0	*uniform*, 0.125	*cross flow*
20	0.25	1.0	*mean shear*	*cross flow*
21	0.25	1.0	*exponential profile*	*cross flow*

it is obtained through the non-dimensionalization that the value of $U_\infty = 0.125$ in the numerical solutions corresponds to the experimental velocity ratio $U_j/U_\infty = 3.0$

The flow visualization results in this experiment show the tilted vortex rings due to the nonuniform distribution of vorticity on the different segments of the ring. In Figure 6.1, the numerical results show some typical and similar tilted vortex rings having the same tilted direction as in the experiment. The back portion of the vortex ring moves upward under the effect of the interaction between the vortex ring and cross-flow. At each time, the side and end views are represented in Figure 6.2. The large value of time was used to observe the deformation of large numbers of vortex rings on each simulation. This inviscid calculations have no provisions for viscous effects.

In order to simulate trailing vortices in a shear wind, an unsteady, two-dimensional, rotational flow field with a concentration of large vorticity in a pair of 'vortical spots' was theoretically and numerically considered by Lin and Ting (1986). They showed a similar tilted vortex pair under the effect of the interaction between a pair of 'vortical spots' and a cross-flow. It presents a reversed tilting direction from the present results because of different coordinate system. This illustrates that for some features of flow phenomena, a two-dimensional problem such as the motion of the vortical spots in a cross-flow, may be useful for a basic understanding of a certain types of three-dimensional flows such as the vortex rings in cross-flow.

In order to study the effect of axial excitation and vorticity within the boundary layer on the initial roll-up of an axisymmetric shear layer into discrete vortex rings, the above numerical scheme was modified by implementing the random vor-

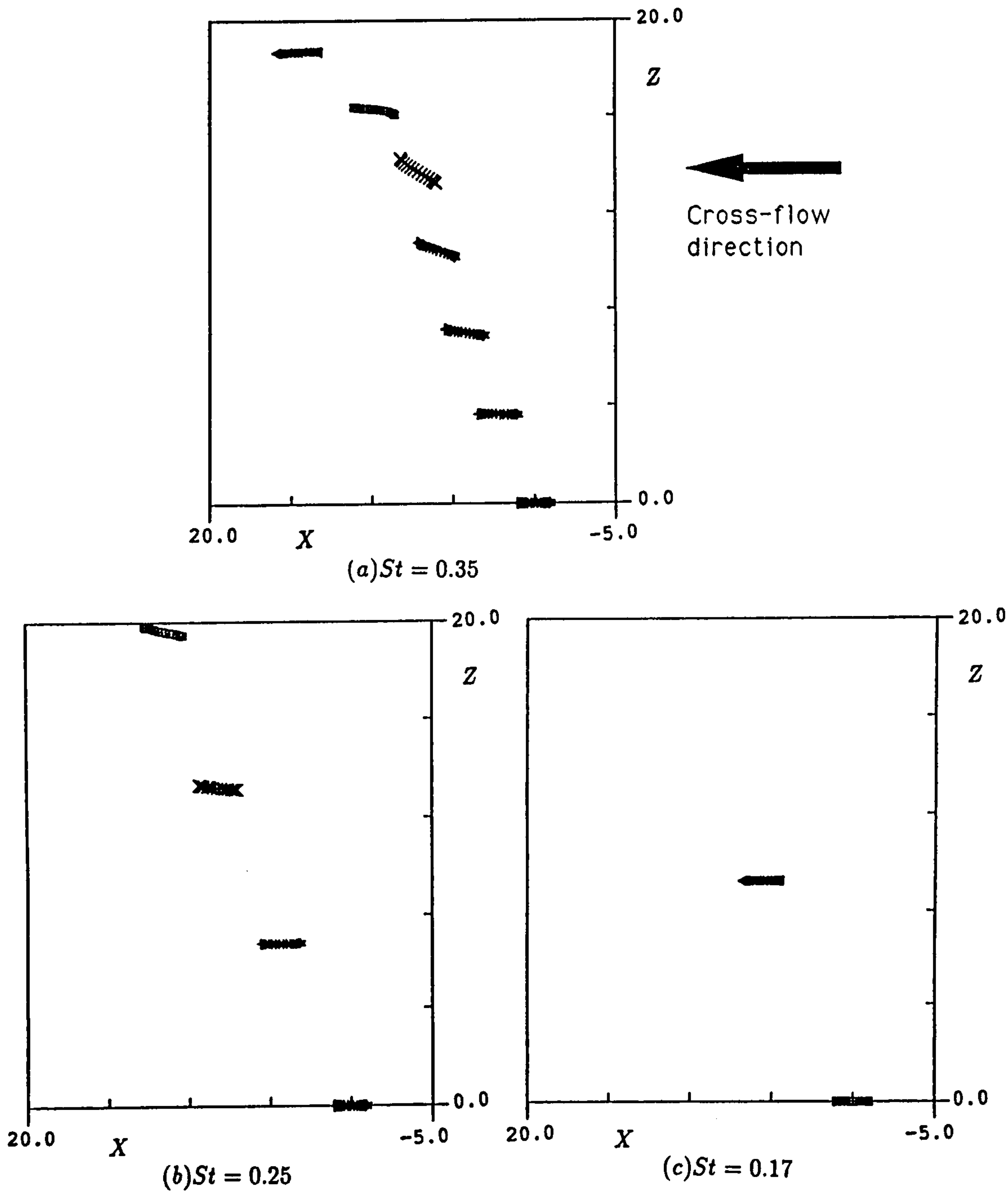

Figure 6.1 Effect of frequency on motion and trajectory at $U_\infty = 0.125$, $\Gamma = 1.0$

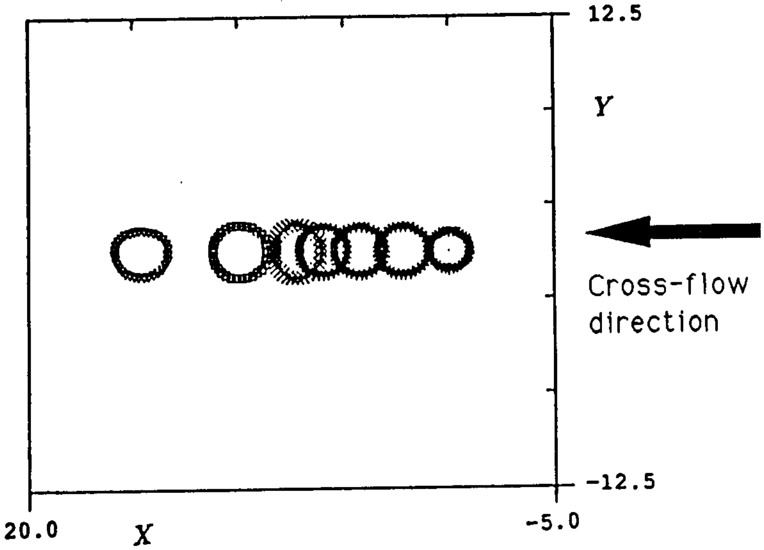

(a) End view

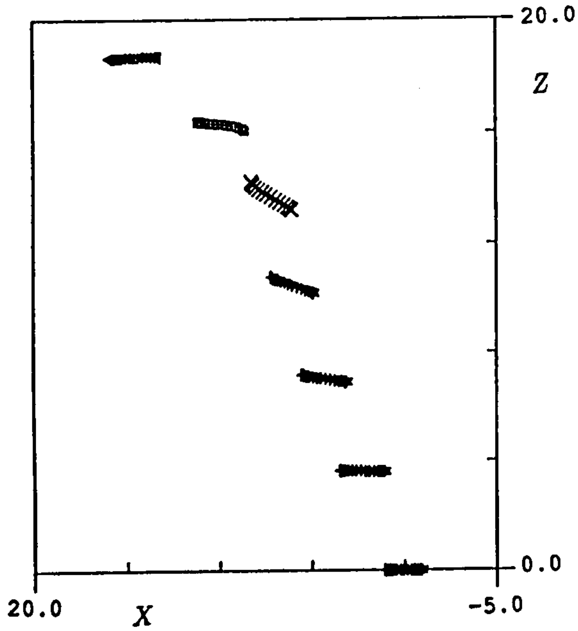

(b) Front view

Figure 6.2 Typical vortex ring evolution at $St = 0.35$, $\Gamma = 1.0$, $U_\infty = 0.125$

tex sheet method originally introduced by Chorin (1978). In this simulation, the shear layer is discretized into a single layer of closely-spaced circular filaments.

In the following subsections, the effects of pulsations through the change of Strouhal number (frequency), circulation strength and cross-flow including constantly uniform, uniform shear and non-uniform flows will be described in terms of ring trajectories and motions. Then, the roll-up of shear layer into vortex rings will be mentioned by considering viscous diffusion and satisfying the no-slip boundary condition along the solid boundary through vorticity creation.

6.2 Effect of Frequency

The sequence of events during vortex ring evolution are shown in Figures 6.1 through 6.4 as a function of frequency. The data in each figure was given a different magnitude of uniform velocity. As the frequency increases, the spatial distance between neighboring vortex rings becomes smaller. Also, the penetration at relatively high frequency is reduced due to the strong interactions between adjacent vortex rings. This observation was revealed in the experimental work described above.

Therefore, it is seen that the spatial distance between vortex rings is determined by the axial pulsation (through Strouhal number). Naturally, the total number of vortex rings generated are reduced within the fixed coordinate frame as the axial frequency increases. Also, the increase of uniform velocity makes the vortex rings more deflected and consequently reduces the penetration with the same pulsation conditions. This causes the total number of rings to be decreased within the fixed frame. The averaged tilting angle in this numerical calculation is in a good agreement with measured value (about 3° to 4°) except for the case of $St = 0.35$ and $U_\infty = 0.125$.

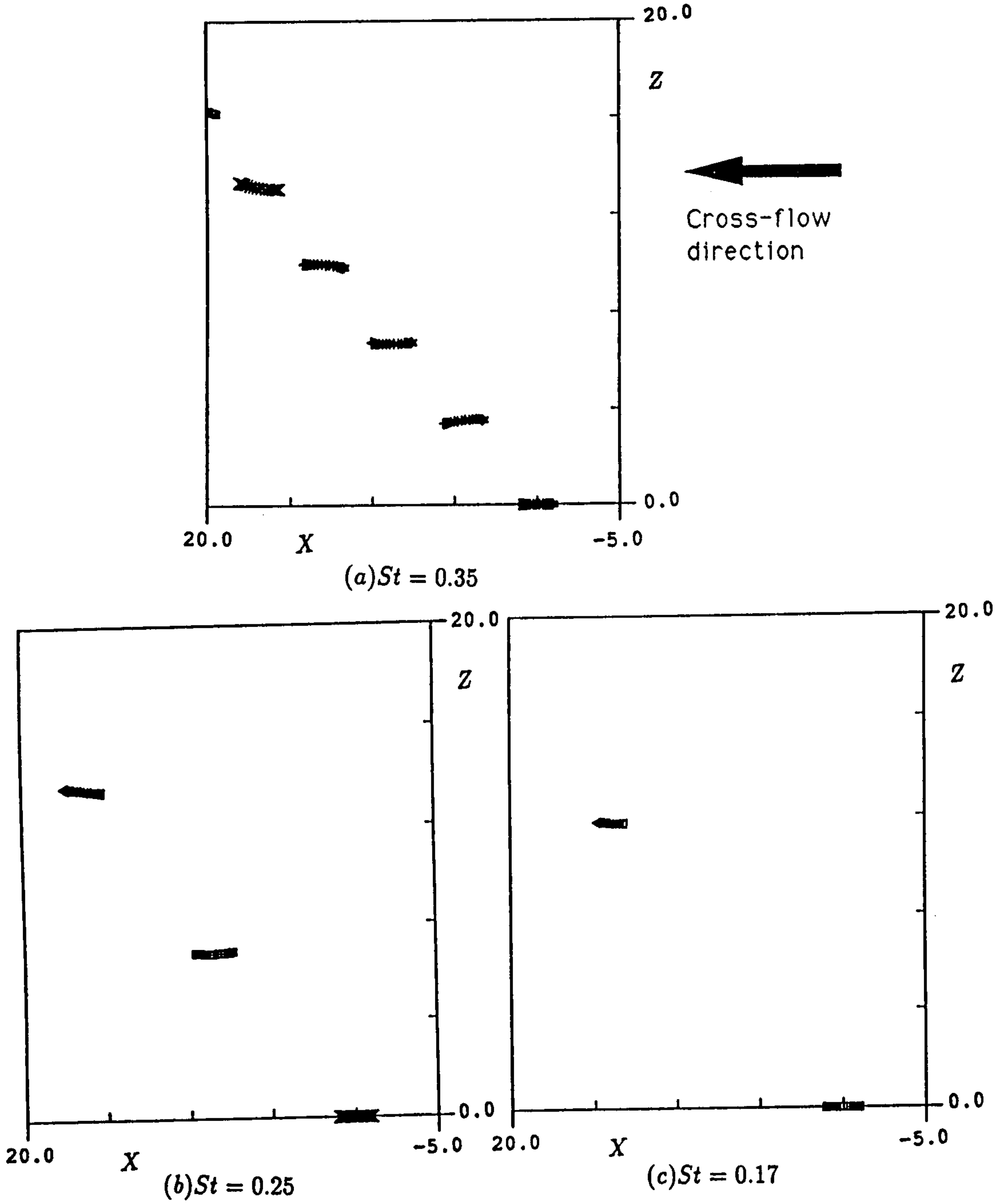

Figure 6.3 Effect of frequency on motion and trajectory at $U_\infty = 0.250$, $\Gamma = 1.0$

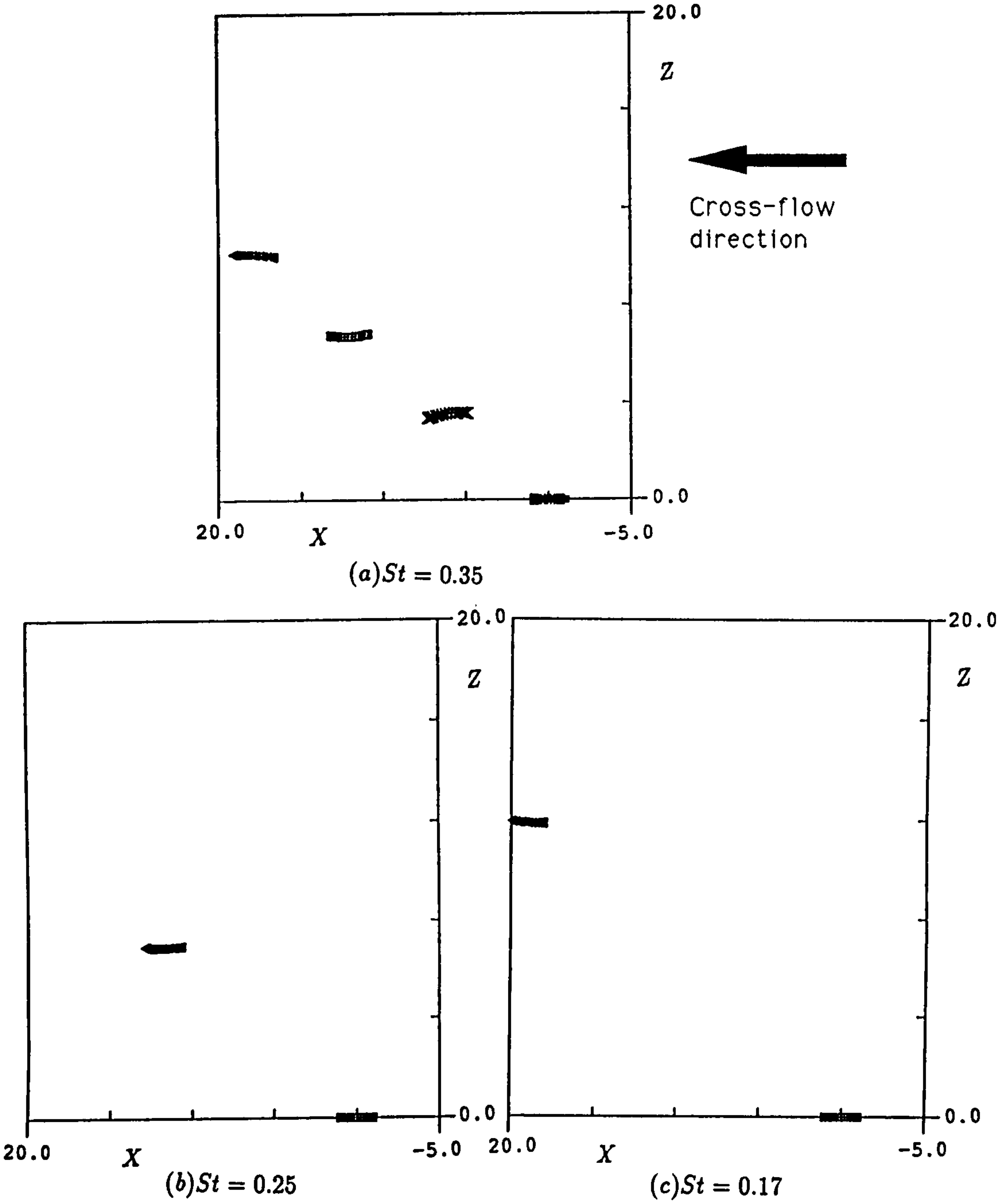

Figure 6.4 Effect of frequency on motion and trajectory at $U_\infty = 0.350$, $\Gamma = 1.0$

6.3 Effect of Circulation

The initial circulation strength of the vortex ring has a significant effect on the trajectories of rings in the cross-flow. As illustrated in Figures 6.5 and 6.6, the penetration of vortex rings into the cross-flow are considerably deeper with the increase of circulation strength. The circulation effect was investigated with two different ranges of Strouhal number.

At relatively high Strouhal number (0.35), as the circulation increases, a tangle of vortex rings is caused due to the strong interaction of two neighboring vortex rings as presented in Figure 6.5. In Figure 6.6 ($St = 0.25$), as expected, a tremendous increase of penetration was observed without entanglement due to the interaction of adjacent vortex rings. Also, the tilted configuration of the ring was not considerably changed as long as the relatively low pulsation is concerned.

6.4 Effect of Cross-Flow

We also investigated the effect of background flow on the vortex ring by just adding different kinds of velocity profile to the right-hand side of equation (3-11). It was discussed by Aref and Flinchem(1984) that the incorporation of the background flow is an approximation which neglects the effect of the vortex ring on the background flow.

The case of uniform shear flow was considered first with $U(Z) = mZ$ where m is 0.125. Next, we impose a non-uniform shear flow with exponential velocity profile as follows,

$$U(Z) = n(1 - exp(-Z)) \qquad (6-1)$$

With $n = 0.125$, this profile has the same shear rate at $Z = 20$ as in the uniform shear flow case. This indicates that it has larger shear rates, than uniform shear case, below $Z = 20$. The vortex ring evolution is shown in Figures 6.7 and 6.8. The

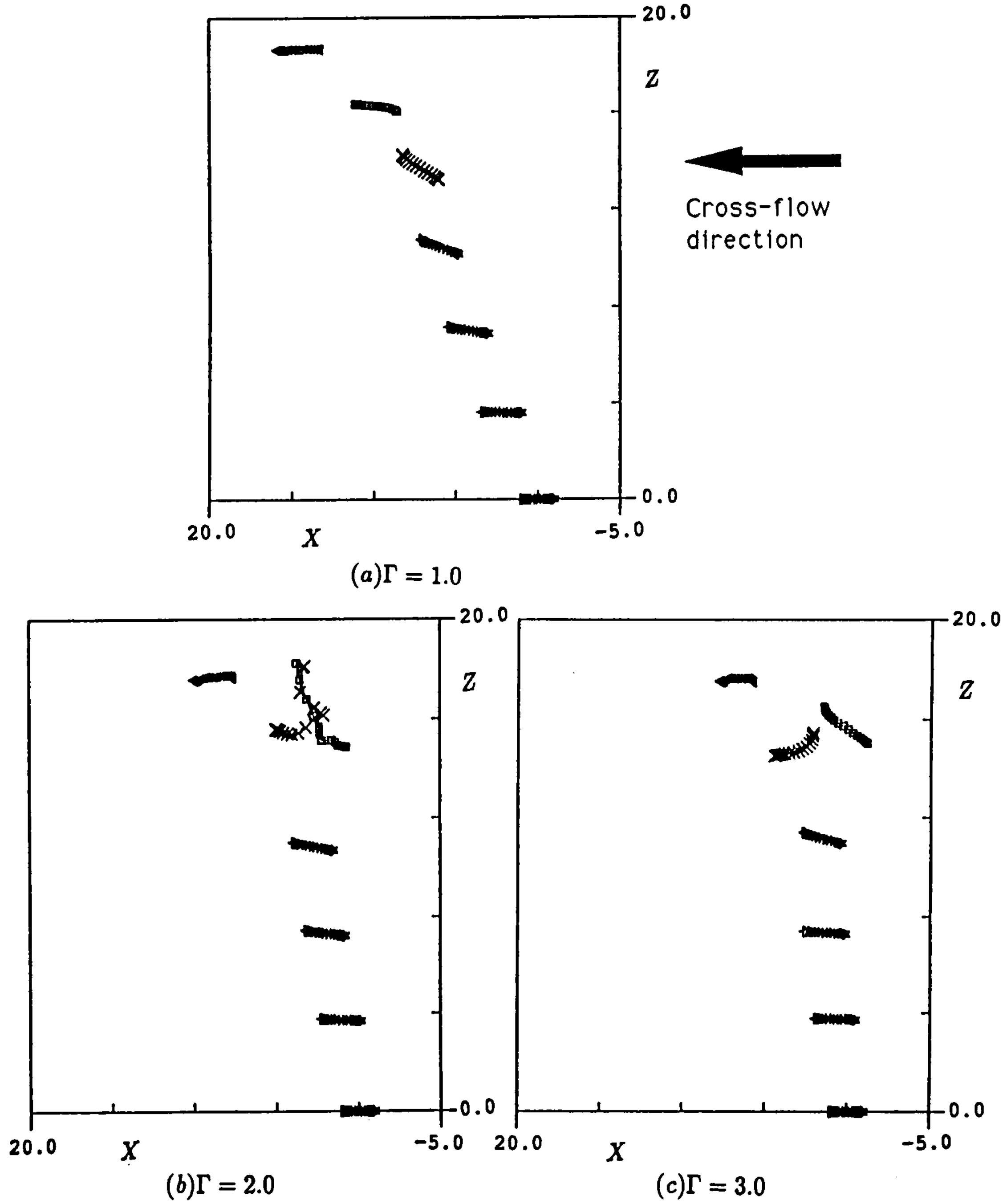

Figure 6.5 Effect of circulation on motion and trajectory at $St = 0.35$, $U_\infty = 0.125$

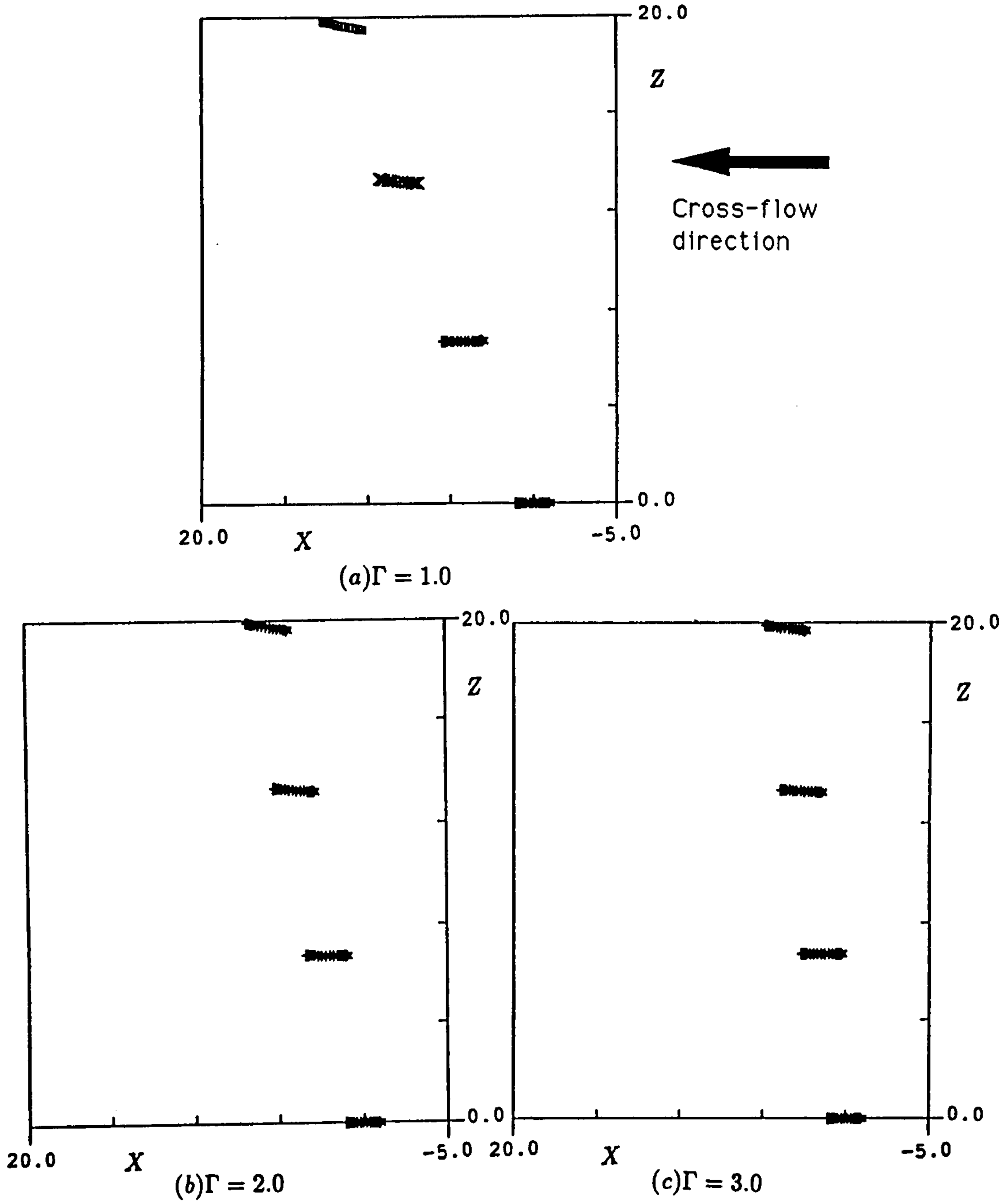

Figure 6.6 Effect of circulation on motion and trajectory at $St = 0.25$, $U_\infty = 0.125$

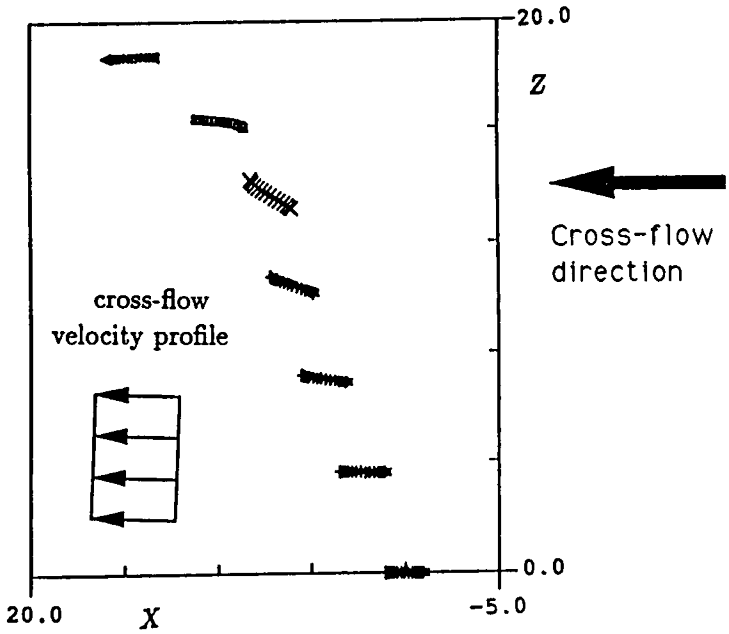

(a) Uniform flow

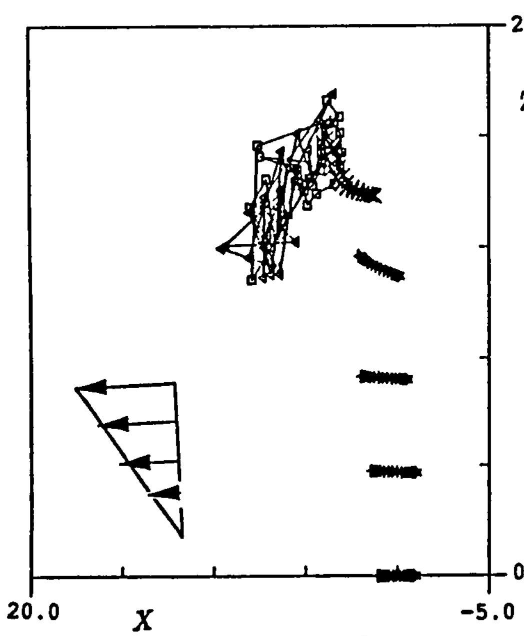

(b) Mean shear flow

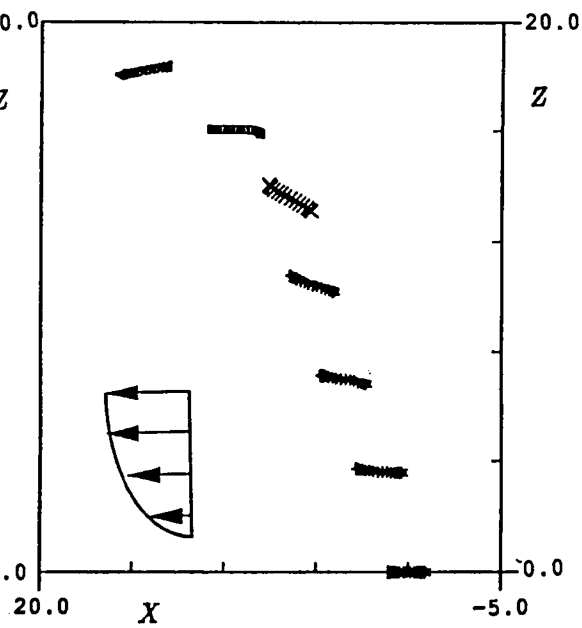

(c) Exponential flow

Figure 6.7 Effect of cross-flow on motion and trajectory at $St = 0.35$, $\Gamma = 1.0$

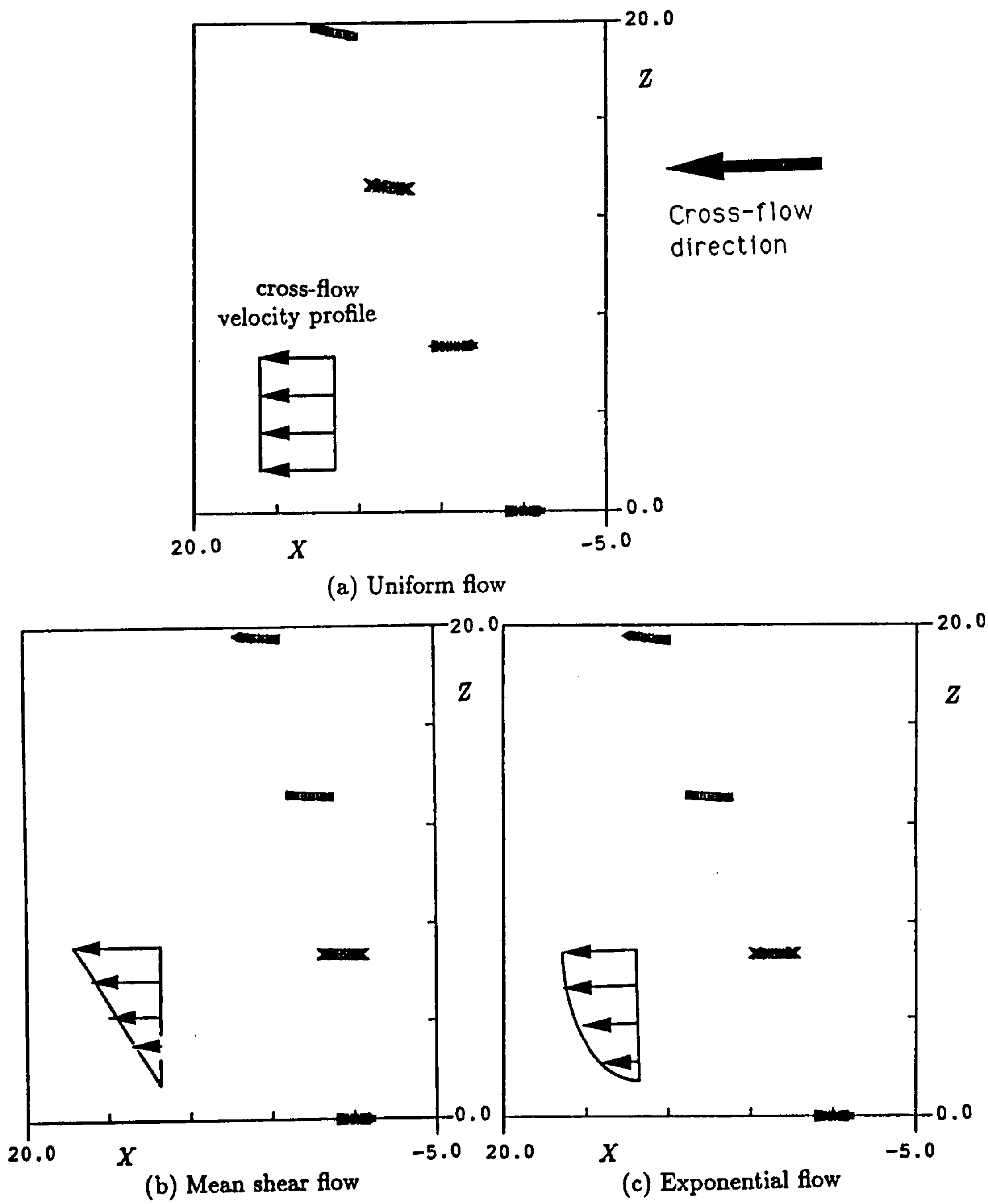

Figure 6.8 Effect of cross-flow on motion and trajectory at $St = 0.25$, $\Gamma = 1.0$

uniform shear flow has more penetration due to the low shear rates, however, at relatively high Strouhal number it tends to easily entangle with strong interactions between adjacent vortex rings. The exponential velocity profile shows more or less close trajectories and motion of vortex rings compared to the constantly uniform cross-flow case.

Two important results are illustrated from this numerical simulation. One is the general motion of vortex rings due to the effect of cross-flow. The other is the tilted configuration of vortex rings in the cross-flow. As shown in the experimental results, the basic circular shape maintains within the fixed coordinate frame.

In order to make more meaningful comparisons between numerical and experimental results, it is necessary to match basic parameters and initial conditions for the generation of vortex rings accurately. That is, at the same time t, the position and induced velocity of the vortex ring should be calculated to reasonably predict the subsequent behavior of the ring.

6.5 Roll-Up of Shear Layer with Viscosity Consideration

The purpose of this simulation is to consider the viscous effect within the boundary layer as well as axial excitations on the ring formation. Since Parekh (1988) described the effects of source flow, forcing, vorticity-matching scheme, forcing amplitude and core size variations on the shear layer dynamics in his study, we will study a viscous effect by just adding the simulation of the viscous diffusion with satisfying no-slip boundary condition along the solid boundary through a vorticity generation to roll-up of shear layer into vortex rings.

First of all, the Blasius-type boundary layer flow was calculated along the wall according to Chorin's random vortex sheet scheme. The simplified geometry of a flat plate wall with an arbitrary and artificial jet exit is shown in Figure

6.9. The assumed jet exit is located downstream after the fully-developed flow is formed. To simplify the problem, the cross-flow is assumed to be a solid flat plate flow without a real jet hole. The roll-up of the shear layer into vortex rings is assumed to consist of individual vortices which are interacting with the vortex elements within the boundary layer without considering three-dimensional effect. This is not expected to cause major errors since the azimuthal variations are anticipated not to be dominating as reviewed in the experimental study. However, the existence of real jet exit forces this analysis to be three-dimensional which requires the solution of full Navier-Stokes equations. At the inlet section, the velocity profile is a uniform potential flow produced by the potential component of the flow. The boundary layer grows along the plate wall with satisfying the no-slip boundary condition through vorticity creation. Figure 6.9 presents the development of the velocity profile along the wall. The boundary layer edge of the fully-developed flow corresponds to $Z = 0.4$ in the shear layer calculation. This boundary layer thickness was estimated from the experiments. Therefore, at $Z \leq 0.4$ it is the boundary layer flow and outside the boundary layer the cross-flow is uniform without any vortex element.

The time evolution of a forced shear layer without cross-flow is shown in Figure 6.10. The diamond symbols represent the positions of the cores of filaments. The gathering of circular filaments into a distinct group corresponds to the formation of a discrete vortex ring. One group of filaments is formed for each excitation period. Figure 6.10 (a) shows the formation of filaments at the end of one excitation period. Depending on the pairing phenomenon, the number of groups can be reduced by one. The existence of pairing can cause two groups to combine into one group with doubling the distance between filament groups. Figure 6.10 (b) presents a symmetrical configuration of three groups of filaments with no pairing event until

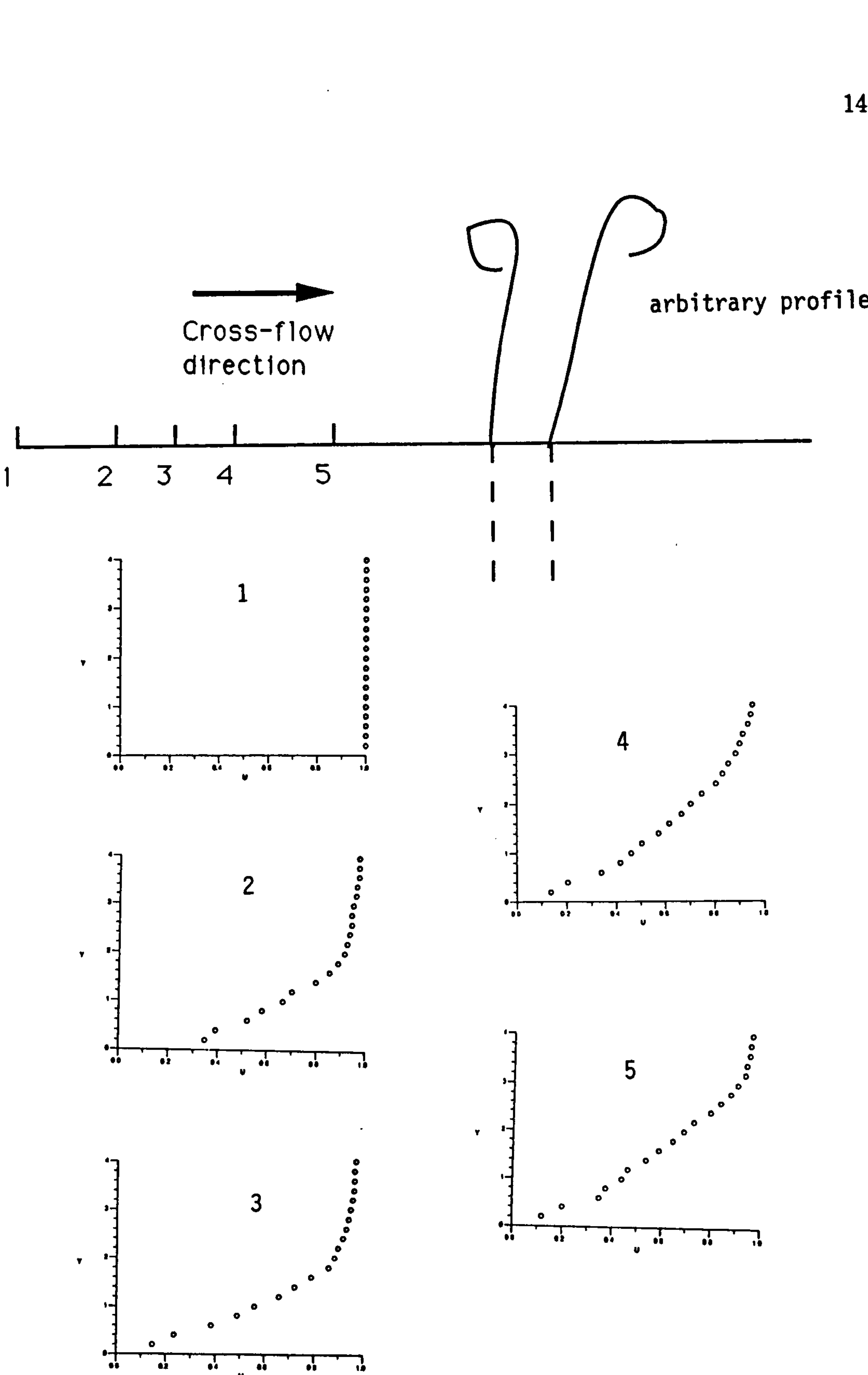

Figure 6.9 A simplified geometry and cross-flow velocity profiles for a developing flow on the wall

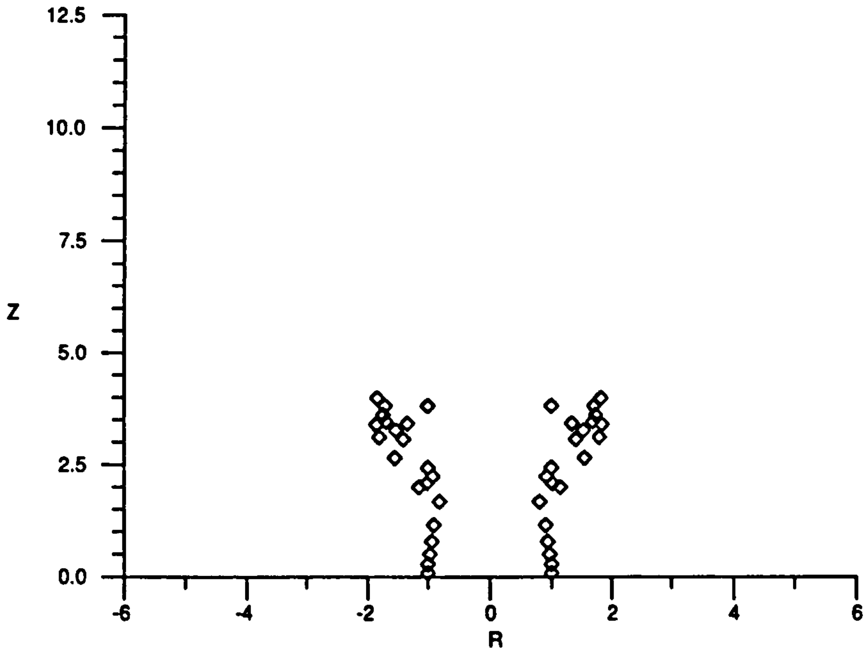

(a) t = 10.0

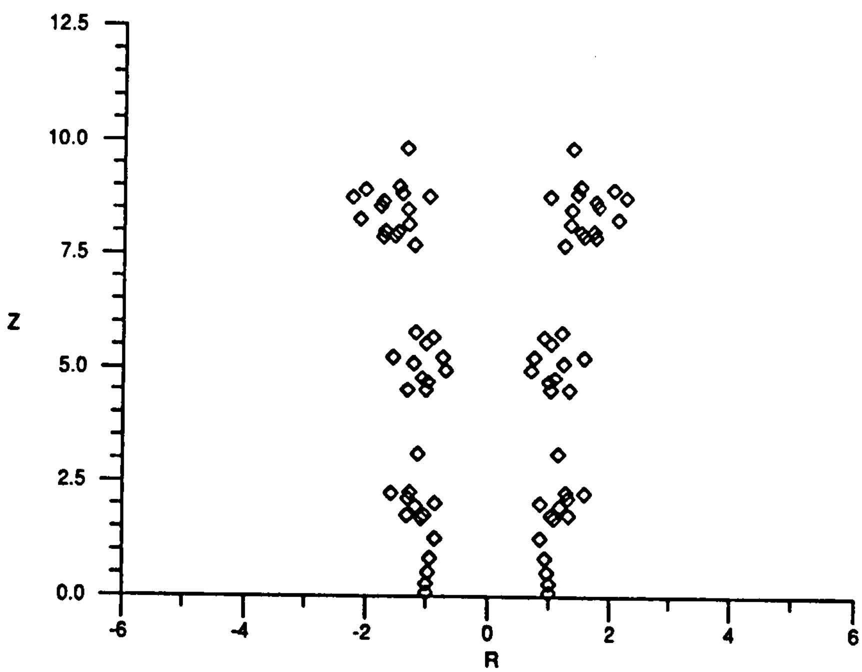

(b) t = 20.0

Figure 6.10 Time evolution of shear layer into vortex ring without cross-flow time $t = 20$ *sec*.

Then, it is attempted to investigate the effect of uniform cross-flow on the roll-up of a shear layer without satisfying the no-slip boundary condition on the wall. It is tended to be tilted with a unsymmetrical configuration as shown in three-dimensional vortex ring simulation as shown in Figure 6.11. It is confirmed that the shear layer calculation shows the same orientation of tilting, i.e., the front part of the core is tilted down and the rear part of the core tilted up for the on-coming cross-flow.

In order to study the effect of a boundary layer on the vortex structure we make an effort to do the numerical simulation of shear layer into vortex ring with cross-flow including the effect of the viscous boundary condition. The numerical and flow parameters used are as followings; For a shear layer simulation, initial ring radius and core radius selected are 1.0 and 0.1, respectively. Strouhl number St and amplitude A_a of forced excitation are 0.4 and 0.2, respectively. Ring circulation Γ was fixed at 0.255 and jet circulation γ varied from the initial value of 1.0. The vortex sheet length h is 0.2 and the maximum intensity of sheet ξ_{max} is 0.2. The viscosity used is 10^{-6}. In this coupled code, the time step Δt and total steps N are 0.05 and 400, respectively. The uniform potential flow U_∞ is 0.0625 and it is matched with the boundary edge velocity at $Z = 0.4$.

Initially, there was no vortex elements generated at time $t = 0$. In a typical run, the average number of vortex elements (sheets) in the boundary layer were 200 to satisfy no-slip boundary condition on the wall. Figure 6.12 illustrates a sequence of time frame representing the evolution of shear layer into vortex ring. As mentioned before, the cross-flow velocity profile is composed of the boundary layer flow below $Z = 0.4$ and uniform potential flow above that. It shows the same

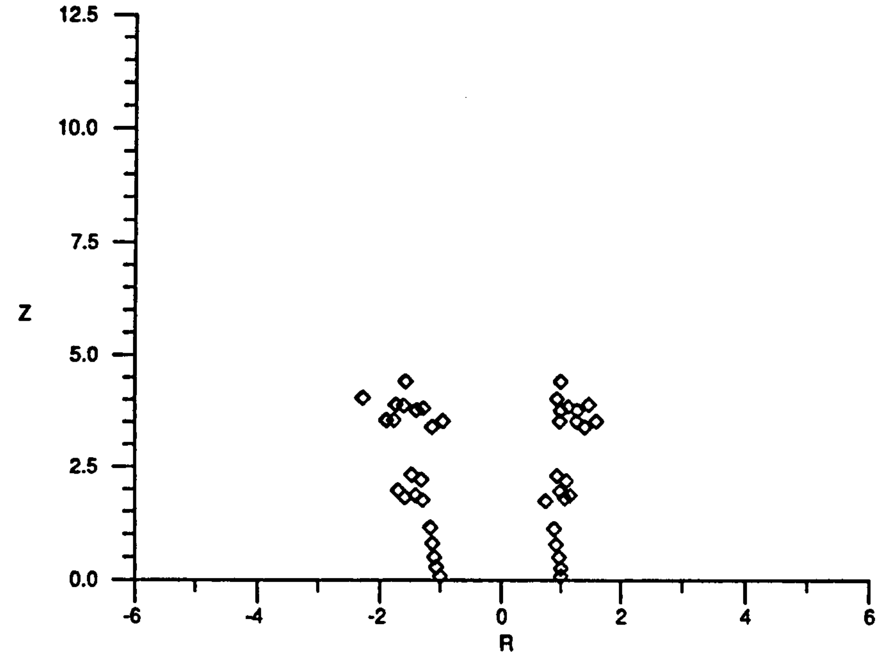

(a) t = 10.0

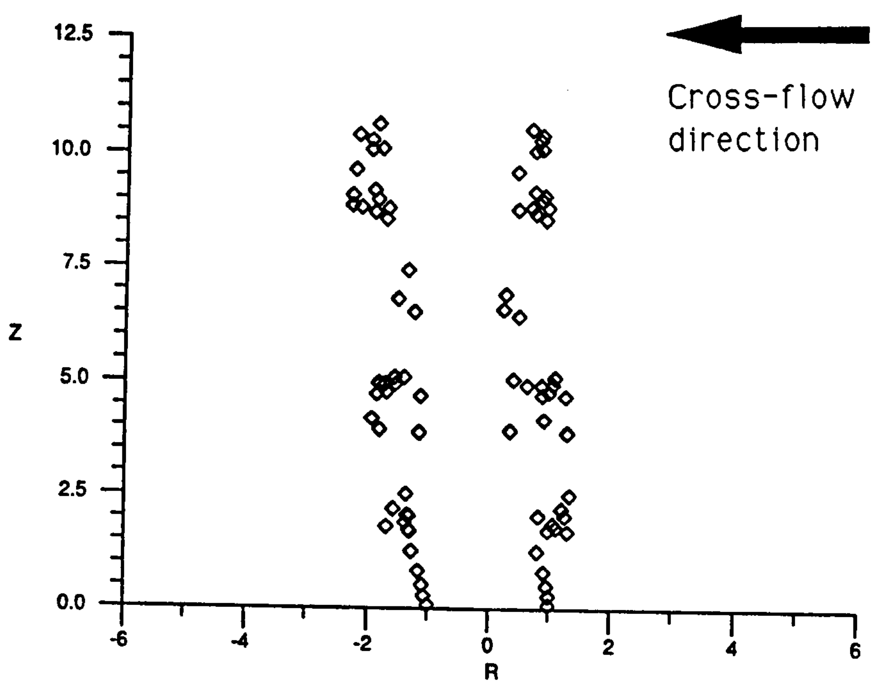

(b) t = 20.0

Figure 6.11 Time evolution of shear layer into vortex ring with uniform cross-flow at $U_\infty = 0.0625$

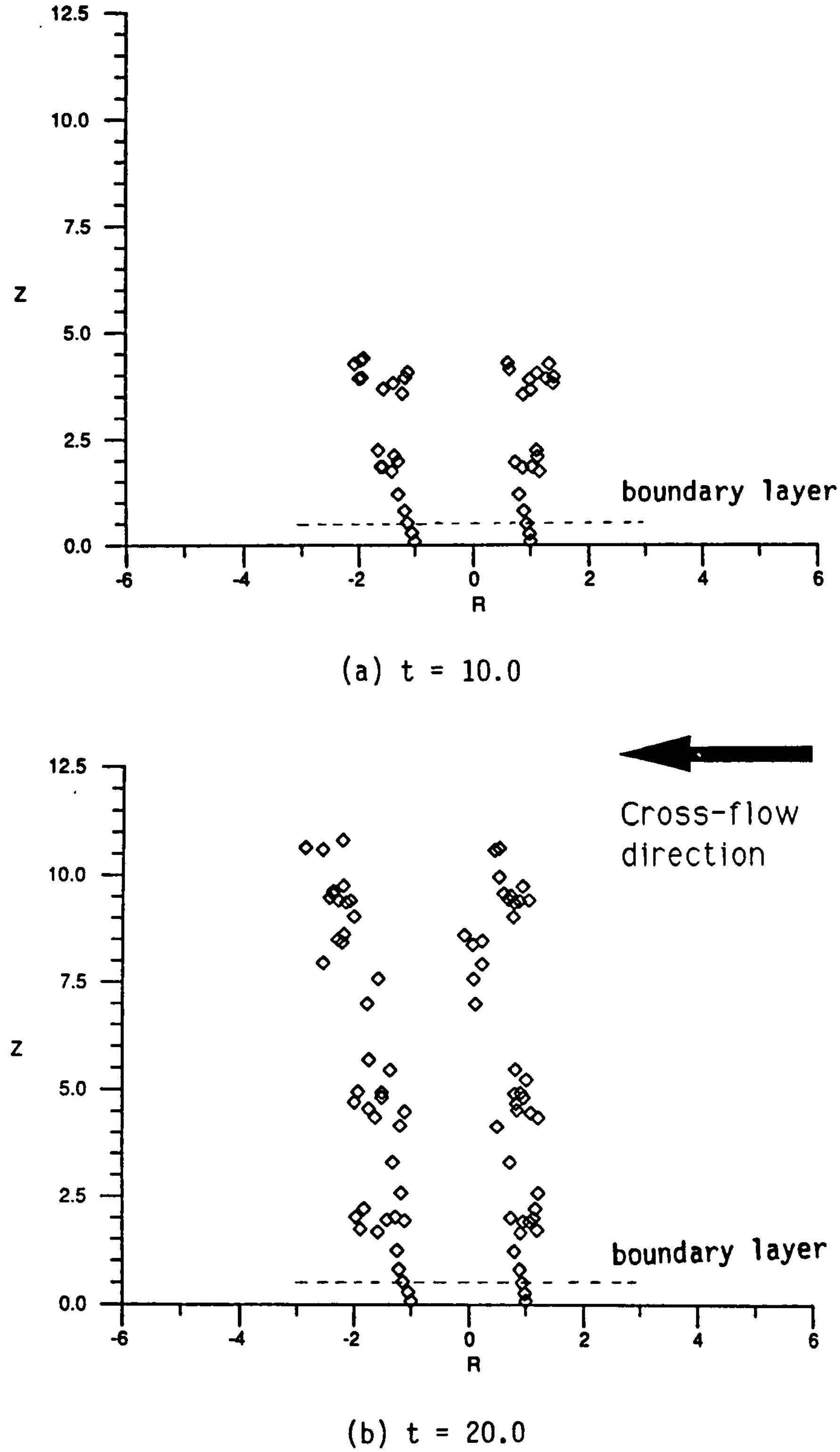

Figure 6.12 Time evolution of shear layer into vortex ring with no-slip boundary condition

grouping of vortex structure corresponding to the formation of a discrete vortex ring as in the uniform cross-flow case of Figure 6.11. However, it is observed that there is no significant contribution to the initial roll-up of the shear layers by the boundary layer effect.

7. Conclusions and Recommendations

The present study was conducted in three different ways; First, through an experimental study, the vortex ring produced by pulsed transverse injection into a uniform cross-flow was investigated using flow visualization techniques and hot-film anemometry. Second, analysis has been done to examine the penetration trajectory, the tilted motion of vortex rings in the cross-flow. Third, a numerical simulation for three-dimensional vortex rings in the cross-flow was carried out using Lagrangian, grid-free, three-dimensional vortex method to compare with experimental results.

Some selected features of vortex rings moving into a cross-flow have been investigated within the pulsation range that the mutual interactions between adjacent rings are negligible. The vortex rings were generated either by the periodic closing and opening of a jet flow (a continuous pulsation) or by the sudden movement of a piston inside cylinder (a single pulsation) in the water tunnel experiments.

A summary of the important results and conclusions will be separately described for each study as followings. The first conclusions are derived for the continuous pulsation. The results for numbers 1 through 5 are obtained from the visual observation using flow visualization techniques including LIF, whileas the results for numbers 6 through 11 are evaluated by hot-film probe measurements.

1. As a result of full pulsation of the jet flow, vortex rings were formed and these vortex rings at low frequencies penetrated into the cross-flow to a height much higher than for high frequencies or for the steady jet.
2. The vortex rings, under the ranges of parameters in this study, moved as a unit blob of fluid with little change in their general shape.

3. The back portion of the vortex ring moves upward (tilted) under the effect of interaction between vortex ring and cross-flow. This fact was qualitatively confirmed from the numerical simulation of three-dimensional vortex ring in cross-flow.
4. The diameter of the vortex ring increased nonlinearly while it moves into the cross-flow. This variation was closely related to the penetration trajectory.
5. It was also observed from the collapsed pulsating jet analysis that the frequency(excitation) is more dominating parameter than momentum flux effect in a pulsating jet.
6. The velocity flow field within the vortex ring pulsed at 1 Hz frequency was measured in detail using a hot-film probe.
7. The detail quantitative data on the translational velocity, circulation, core and ring sizes were obtained at three different downstream locations ($Z = 3\ d_j$, $7\ d_j$ and $10\ d_j$) for a typical vortex ring generated at 1 Hz pulsation.
8. The tilting angle for a typical vortex ring mentioned above was measured using hot-film probe. Generally, the tilted angle was increased as the ring moves downstream at three point measurements. The average tilted angle was approximately between 3° and 4°.
9. It was found from the velocity traces that the vortex ring was fully-formed at $Z = 3\ d_j$. This was a good agreement with other experiments in air as well as computational results.
10. The radius ratio between core and ring was maintained almost constant, which conflicts with inviscid equation $R^2 a = const.$ where R and a indicate ring and core radius, respectively.
11. The amount of circulation measured by the hot-film probe was close to that predicted by a simple 'slug' model. At $Z = 3\ d_j$, 9.2 % of the ideal circulation

was lost from the ring while 24.2 % was lost at 10 d_j.

The following conclusions are drawn from the single pulsation study to mainly investigate the influence of different exit geometries.

1. For the same piston velocity, the exit velocity and consequently the translational velocity of a vortex ring for a sharp-edged orifice exit was much faster than that for a straight walled tube. Therefore, the penetration height for the sharp-edged orifice is deeper than that for the straight walled tube.
2. For the same exit velocity which is obtained by different piston pressures and piston velocities, the penetration level did not vary significantly. However, it was slightly deeper for the sharp-edged orifice than for the straight walled tube.
3. A vortex ring ejected from the sharp-edged orifice entrained less fluid than that ejected from the straight walled tube exit.
4. It was found that the jet exit boundary condition is a key parameter which determines the vorticity strength and the formation process of a vortex ring.

The following conclusions are drawn through analytical investigation.

1. It was found that the penetration level and the motion of vortex ring depend on the ratio of cross-flow velocity to ring translational velocity and the pulsating frequency (piston velocity in the single pulse experiment).

Finally, the following conclusions are drawn from the numerical calculations.

1. The effects of frequencies, circulation strengths and background flow were investigated in terms of the motion and penetrations of the vortex rings.
2. As the frequency (Strouhal number) increased, the spatial distance between neighboring vortex rings became smaller. Also, the penetration at relatively high frequencies was reduced due to the strong interactions between adjacent

vortex rings as already indicated in the continuous pulsation experiment.

3. The tilting motion of the vortex ring moving into the cross-flow was qualitatively confirmed.

Some suggestions in terms of the extension of this study can be made as followings.

1. A bigger vortex ring will be easier to obtain more accurate quantitative data with minimizing the interference of hot-film probe within the vortex ring.
2. The effect of the ratio between piston length and exit diameter on the formation process, characteristic parameters and penetration of the ring will be another interesting topics using single pulsation in the cross-flow.
3. More information on three-dimensional velocity field will be needed for full understanding of three-dimensional vortex ring in cross-flow.
4. In order to investigate the amount of entrainment in terms of mixing improvement, some detail measurements at relatively high frequency range ($5-15\ Hz$) should be carried out.

Bibliography

Bibliography

1. Abernethy, R. B. and Thompson, J. W., "Handbook; Uncertainty in Gas Turbine Measurements," AEDC-TR-73-5, 1973.

2. Akhmetov, D. G. and Kisarov, O. P., "Hydrodynamic Structure of a Vortex Ring," J. Applied Mechanics and Technical Physics, Vol. 7, No. 4, 1966, pp. 87–90.

3. Anderson, A. B. C., "Structure and Velocity of the Periodic Vortex- Ring Flow Pattern of a Primary Pfeifenton(Pipe Tone) Jet," J. Acoustical Society of America, Vol. 27, No. 6, 1955, pp. 1048–1053.

4. Andreopoulos, J. and Rodi, W., "Experimental Investigation of Jets in a Crossflow," J. Fluid Mech., Vol. 138, 1984, pp. 93–127.

5. Aref, H. and Flinchem, E. P., "Dynamics of a Vortex Filament in a Shear Flow," J. Fluid Mech., Vol. 148, 1984, pp. 477–497.

6. Arnold, O., "Verhalten von Wirbelringen in turbulenzarmer und turbulenter Umgebung," Ph.D. Dissertation, University of Karlsruhe, Germany, 1974.

7. Ashurst, W. T. and Meiburg, E., "Three–Dimensional Shear Layers via Vortex Dynamics," J. Fluid Mech., Vol. 189, 1988, pp. 87–116.

8. Auerbach, D., "Stirring Properties of Vortex Rings," Phys. Fluids A 3, 1991, pp. 1351–1355.

9. Batchelor, G. K., An Introduction to Fluid Dynamics, Cambridge University Press, 1967.

10. Bernal, L. P., Hirsa, A., Kwon, J. T. and Willmarth, W. W., "On the Interaction of Vortex Rings and Pairs with a Free Surface for Varying Amounts of Surface Active Agent," The Physics of Fluids, Vol. 1, No. 12, Dec. 1989, pp. 2001–2004.

11. Binder, G. And Favre-Marinet, M., "Mixing Improvement in Pulsating Turbulent Jets," in Fluid Mechanics of Mixing (ed. Uram and Goldschmidt), ASME United Engineering Center, 1973, pp. 167-172.

12. Boldes, U. and Ferreri, J. C., "Behaviour of Vortex Rings in the Vicinity of a Wall," The Phys. of Fluids, Vol. 16, 1973, pp. 2005–2006.

13. Brasseur J. G. and Chang, I., "Combination of Kinematics with Flow Visualization to Compute Total Circulation," AIAA J., Vol. 19, 1981, pp. 878–884.

14. Bremhorst, K. and Harch, W. II., "Near Field Velocity Measurements in a Fully Pulsed Subsonic Air Jet," Turbulent Shear Flows I, Springer-Verlag, Berlin, 1979, pp. 480–500.

15. Bruun, H. H., "Interpretation of a Hot-Wire Signal Using a Universal Calibration Law," J. Phys. E:Sci. Instrum. Vol. 4, 1971, pp. 225–231.

16. Cerra, A. W. and Smith, C. R., "Experimental Observations of Vortex Ring Interaction with the Fluid Adjacent to a Surface," Report FM-4, Dept. of Mechanical Engr. & Mechanics, Lehigh University, 1983.

17. Champagne, F. H., Sleicher, C. A. and Wehrmann, O. H., "Turbulence Measurements with Inclined Hot-Wires:Part 1," J. Fluid Mech., Vol. 28, 1967, pp. 153–176.

18. Chassaing, P., George, J., Claria, A. and Sananes, F,, "Physical Characteristics of Subsonic Jets on a Cross-Stream," J. Fluid Mech., Vol. 62, 1974, pp. 41–64.

19. Cheer, A. Y., "Numerical Study of Incompressible Slightly Viscous Flow Past Blunt Bodies and Airfoils," SIAM J. Sci. Stat. Comput., Vol. 4, 1983, pp. 685–705.

20. Cheer, A. Y., "Unsteady Separated Wake Behind an Impulsively Started Cylinder in Slightly Viscous Fluid," J. Fluid Mech., Vol. 201, 1989, pp. 485–505.

21. Choi, Y., Humphrey, A. C. and Sherman, F. S., "Random-Vortex Simulation of Transient Wall-Driven Flow in a Rectangular Enclosure," J. Comput. Phys., Vol. 75, 1988, pp. 359–383.

22. Chorin, A. J., "Numerical Study of Slightly Viscous Flow," J. Fluid Mech., Vol. 57, 1973, pp. 785–796.

23. Chorin, A. J., "Vortex Street Approximation of Boundary Layers," J. Comput. Phys., Vol. 27, 1978, pp. 428–442.

24. Chorin, A. J., "Vortex Models and Boundary Layer Instability," SIAM J. Sci. Stat. Comput., Vol. 1, 1980, pp. 1–22.

25. Chu, C. C. and Falco, R. E., "Vortex Ring/Viscous Wall Layer Interaction Model of the Turbulence Production Process Near Walls," Experiments in Fluids, Vol. 6, 1988, pp. 305–315.

26. Collins, F., "Description of the University of Tennessee Space Institute Water Tunnel," UTSI Report 82-1, University of Tennessee Space Institute, TN, 1982.

27. Dahm, M. and Rasmussen C. G., "Effect of Wire Mounting System on Hot-Wire Probe Characteristics," Disa Information No. 7, 1969, pp. 19–24.

28. Dahm, W. J. A., Scheil, C. M. and Tryggvason, G., "Dynamics of Vortex Interaction with a Density Interface," J. Fluid Mech., Vol. 205, 1989, pp. 1–43.

29. Didden, N., "Untersuchung laminarer, instabiler Ringwirbel mittels Laser-Doppler-Anememetrie," Mitt Nr. 64, Gottingen: Max-Planck-Inst., Stromungsforschung, 1977.

30. Didden, N. "On the Formation of Vortex Rings: Rolling-Up and Production of Circulation," ZAMP, Vol. 30, 1979, pp. 101–106.

31. Doligalski, T. L., Smith, C. R. and Walker J. D. A., "A Production Mechanism for Turbulent Boundary Layer Flows," Viscous Flow Drag Reduction, edited by Gary Hough, Progress in Astronautics and Aeronautics, Vol. 72, 1980.

32. Drubka, R. E. and Nagib, H. M., "On-temperature and Yaw Dependence of Hot-Wires," IIT Fluids and Heat Transfer Report R77-1, Illinois Institute Technology, 1977.

33. Falco, R. E., "A Synthesis and Model of Turbulence Structure in the Wall Region," in Structure of Turbulence in Heat and Mass Transfer, edited by Z. P. Zaric, Hemisphere, 1982.

34. Favre-Marinet, M. and Binder, G., "Some Characteristics of Pulsating or Flapping Jets," Unsteady Turbulent Shear Flows, Springer-Verlag, New York, 1981, pp. 370–379.

35. Fingerson, L. M. and Freymuth, P., "Thermal Anemometers,", in IFA 100 System Instruction Manual, TSI, 1983.

36. Fohl, T. and Turner J. S., "Colliding Vortex Rings," The Phys. of Fluids, Vol. 18, 1975, pp. 433–436.

37. Fraenkel, L.E., "On Steady Vortex Rings of Small Cross-Section in an Ideal Fluid," Proc. Roy. Soc. Lond. A 316, 1970, pp. 29–62.

38. Fujita, H. and Kovasznay, S. G., "Measurements of Reynolds Stress by a Single Rotated Hot-Wire Anemometer," Rev. Sci. Instrum., Vol. 39, 1968, pp. 1131–1135.

39. Fung, Y. T., Liu, C. H. and Gunzburger, M. D., "Simulation of the Pressure Field near a Jet by Randomly Distributed Vortex Rings," J. AIAA, Vol. 17, 1979, pp. 553–557.

40. Ghoniem, A. F. and Sethian J. A., "Effext of Reynolds NUmber on the Structure of Recirculating Flow," J. AIAA, Vol. 25, 1987, pp. 168–171.

41. Glezer, A., "An Experimental Study of a Turbulent Vortex Ring," Ph.D. desertation at California Institute of Technology, 1981.

42. Glezer, A., "The Formation of Vortex Rings," The Phys. of Fluids, Vol. 31, Dec. 1988, pp. 3532–3542.

43. Guhler, M. and Sallet, D. W., "The Formation of Vortex Rings and Their Initial Motion," Z. Flugwiss Weltraumoforsch, Vol. 3, 1979, pp. 109–115.

44. Hicks, W. M., "Researches on the Motion of Vortex Rings," Proc. Roy. Soc. Lond. 176, Part 2, 1885, pp. 725–780.

45. Hinze, J. O., "Turbulence" 2nd edition, McGraw-Hill, Chapter 2, 1959.

46. Hussaini, M. Y., Collier, F. and Bushnell, D. M., "Turbulence Alteration Due to Shock Motion," IUTAM Symposium, Turbulent Shear–layer/Shock–Wave Interactions, edited by J. Delery, Springer–Verlag, New York, 1985, pp. 371–381.

47. Irdmusa, J. Z. and Garris, C. A., "Influence of Initial and Boundary Conditions on Vortex Ring Development," J. AIAA, Vol.25, 1987, pp. 371–372.

48. Irwin, H. P. A. H., "The Longitudinal Cooling Correction for Wires Inclined to the Prongs and Some Turbulence Measurements in Fully Developed Pipe Flow," Mech. Eng. Res. Lab. TN 72-1, McGill University, 1971.

49. Johnson, G. M., "Researches on the Propagation and Decay of Vortex Rings," ARL 70–0093, Wright-Patterson AFB, OH, June 1970.

50. Jorgensen, F. E., "Directional Sensitivity of Wire and Fiber-Film Probes," Disa Information No. 11, 1971, pp. 31–37.

51. Kambe, T. and Oshima, Y., "Generation and Decay of Viscous Vortex Rings," J. Phys. Society of Japan, Vol. 38, 1975, pp. 271–280.

52. Kamotani, Y. and Greber, I., "Experiments on a Turbulent Jet in a Cross Flow," J. AIAA, Vol.10, 1972, pp. 1425–1429.

53. Keffer, J. F. and Baines, W. D., "The Round Turbulent Jet in a Cross Wind," J. Fluid Mech., Vol. 15, 1963, pp. 481–497.

54. Kline, S. J. and McClintock, F. A., "Describing Uncertainties in Single-Sample Experiments," Mechanical Engineering, 75, Jan., 1953, pp. 3–8.

55. Krutzsch, C. H., "Uber ein instabiles Gebiet bei Wirbelringen," ZAMM, Vol. 16, 1936, pp. 352–353.

56. Lee, M. J. D., "Bifurcating and Blooming Jets," Ph.D Thesis, Stanford University, 1985.

57. Leonard, A., "Vortex Methods for Flow Simulation," J. of Comp. Physics, Vol. 37, 1980, pp. 289-335.

58. Leonard, A., "Computing Three–Dimensional Incompressible Flows with Vortex Elements," Ann. Rev. Fluid Mech., Vol. 17, 1985, pp. 523–559.

59. Liess, C., " Experimentelle Untersuchung des Lebenslaufes von Ringwirbeln," Max-Planck-Institut für Strömungsforschung, Göttingen, Bericht 1/1978.

60. Liu, C. H., Maestrello, L. and Gunzburger, M. D., "Simulation by Vortex Rings of Unsteady Pressure Field near a Jet ," Progress in Astronautics and Aeronautics-Aeroacoustics:Jet Noise, Combustion and Core Engine Noise. Edited by I. R. Schwartz, AIAA, New York, 43, pp. 47–64.

61. Liu, C. H. and Ting, L., "Motion and Interaction of Decaying Trailing Vortices in Spanwise Shear Wind," NASA TP–2599, 1986.

62. Lo, K. C. R. and Ting, L., "Studies of Merging of Two Vortices," The Physics of Fluids, Vol. 19, 1976, pp. 912–913.

63. Lockwood, R. M., "Pulse Reactor Lift-Propulsion System Development Program," Hiller Aircraft Company, Rept. No. ARD-308, March 1963.

64. Lovett, J. A. and Turns, S. R., "Experiments on Axisymmetrically Pulsed Turbulent Jet Flames," AIAA J., Vol. 28, 1990, pp. 38–46.

65. Magarvey, R. H. and MacLatchy, C. S., "The Formation and Structure of Vortex Rings," Canad. J. Physics, Vol. 42, 1964(a), pp. 678–683.

66. Maxworthy, T., "The Structure and Stability of Vortex Rings," J. Fluid Mech., Vol. 51, 1972, pp. 15–32.

67. Maxworthy, T., "Turbulent Vortex Rings," J. Fluid Mech., Vol. 64, 1974, pp. 227–239.

68. Maxworthy, T., "Some Experimental Studies of Vortex Rings," J. Fluid Mech., Vol. 81, 1977, pp. 465–495.

69. McCracken, M. F. and Peskin, C. S., "A Vortex Method for Blood Flow through Heart Valves," J. Comput. Phys., Vol. 35, 1980, pp. 183–205.

70. Moore, D. W. and Saffman, P. G., "The Motion of a Vortex Filament with Axial Flow," Phil. Trans. Roy. Soc. London, Series A272, 1972, pp. 403–429.

71. Norbury, J., "A Family of Steady Vortex Rings," J. Fluid Mech., Vol. 57, 1973, pp. 417–431.

72. Oshima, Y., "Motion of Vortex Ring in Water," J. Phys. Society of Japan, Vol. 32, 1972, pp. 1125–1131.

73. Oshima, Y. and Asaka, S., "Interaction of Two Vortex Rings Along Parallel Axes in Air," J. Phys. Society of Japan, Vol. 42, 1977, pp. 708–713.

74. Oshima, Y., Kambe, T., and Asaka, S., "Interaction of Two Vortex Rings Moving Along a Common Axis of Symmetry," J. Phys. Society of Japan, Vol. 38, 1975, pp. 1159–1166.

75. Oshima, Y. and Asaka, S., "Interaction of Multi-Vortex Rings," J. Phys. Society of Japan, Vol. 42, 1977, pp. 1391–1395.

76. Oshima, Y., "Head-On Collision of Two Vortex Rings," J. Phys. Society of Japan, Vol. 44, 1978, pp.328–331.

77. Oshima, Y. and Kuwahara, K., "Experimental and Numerical Study of Vortex Interactions," AIAA Paper 84–1546, 1984.

78. Oshima, Y. and Izutsu, N., "Cross-Linking of Two Vortex Rings," The Phys. of Fluids, Vol. 31, 1988, pp.2401–2403.

79. Parekh, D. E., Leonard, A. and Reynolds, W. C., "Bifurcating Jets at High Reynolds Numbers," Report No. TF–35, Thermosciences Division, Dept. of Mechanical Engineering, Stanford University, 1988.

80. Patton, A. J., Test, F. L. and Hagist, W. M., "An Experimental Investigation of a Heated Two-Dimensional Water Jet Discharge into a Moving Stream," J. Heat Transfer, August, 1974, pp. 273–278.

81. Patton, A. J., Test, F. L. and Hagist, W. M., "An Experimental Investigation of a Heated Two-Dimensional Water Jet Discharge into a Moving Stream," ASME Paper No. 74-HT-GG, 1974.

82. Pullin D. I., "Vortex Ring Formation at Tube and Orifice Openings," The Phys. Fluids, Vol. 22, March, 1979, pp. 401–403.

83. Reynolds, W. C. and Bouchard, E. E., "The Effect of Forcing on the Mixing-Layer Region of a Round Jet," Unsteady Trubulent Shear Flows, Springer-Verlag, New York, 1981, pp. 402–411.

84. Rosenhead, L., "The Formation of Vortices from a Surface of Discontinuity," Proc. Roy. Soc. Series A, Vol. 134, 1931, pp. 170–192.

85. Saffman, P. G., "The Velocity of Viscous Vortex Rings," Studies in Applied Math., Vol. 49, 1970, pp. 371–379.

86. Sallet, D. W. and Widmayer, R. E., "An Experimental Investigation of Laminar and Turbulent Vortex Rings in Air," Z. Flugwiss., Vol. 22, 1974, pp. 207–215.

87. Sarohia, V. and Bernal, L. P., "Entrainment and Mixing in Pulsatile Jets," Proceedings of the 3rd Symp. Turbulent Shear Flow, 1981, pp. 11.30–11.35.

88. Sarpkaya, T., "Computational Methods with Vortices– The 1988 Freeman Scholar Lecture," J. Fluid Engineering, Vol. 111, March, 1989, pp. 5–52.

89. Schatzle, P. R., "An Experimental Study of Fusion of Vortex Rings," Ph.D Thesis, California Institute of Technology, 1987.

90. Sherif, S. A., "Measurements of the Flow and Thermal Characteristics of Turbulent Jets in Cross-Flow," Ph D. thesis, Iowa State University,

91. Southerland, K. B., Porter, J. R., Dahm, W. J. A. and Buch, K. A., "An Experimental Study of the Molecular Mixing Process in an Axisymmetric Laminar Vortex Ring," Phys. Fluids A 3, 1991, pp. 1385–1392.

92. Sullivan, J. P., Widnall, S. E., and Ezekiel, S., "Study of Vortex Rings Using a Laser Doppler Velocimeter," AIAA J., Vol 11, 1973, pp. 1384–1389.

93. Summers D. M., Hanson, T. and Wilson, C. B., "A Random Vortex Simulation of Wind-Flow over a Building," International J. Numerical Methods in Fluids, Vol. 5, 1985, pp. 849–871.

94. Taylor, G. I., "Formation of a Vortex Ring by Giving an Impulse to a Circular Disk and then Dissolving it Away," J. Applied Physics, Vol. 24, No. 1, 1953, p. 104.

95. Thomson, J. J., A Treatise on the Motion of Vortex Rings, Macmillan, London, 1883.

96. Ting, L., and Tung, C., "Motion and Decay of a Vortex in a Nonuniform Stream," The Physics of Fluids, Vol. 8, No. 6, 1965, pp. 1039–1051.

97. Tung, C. and Ting, L., "Motion and Decay of a Vortex Ring," The Phys. of Fluids, Vol. 10, No. 5, 1967, pp. 901–910.

98. Vakili, A. D., Chang, Y. K. and Wu, J. M., "Vortex Rings in Uniform Cross-Flow," Presented at 29th Aerospace Sciences Meeting, AIAA, AIAA Paper 91-0522, Reno, Jan. 1991.

99. Vakili, A. D., Wu, J. M., Chang, Y. K. and Yu, F. M., "Pulsed Jets in Cross-Flow," Presented at International Symposium on Unsteady Flow in ASME, Toronto, Canada, June 1990.

100. Vandsburger, U., Lewis, G., Seitzman, J. M. and Allen, M. G., "Flame-Flow Structure in an Acoustically Driven Jet Flame," Western States Section/The Combustion Institute Fall Meeting, University of Arizona, Paper 86–19, 1986.

101. Viets, H., and Sforza, P. M., "Dynamics of Bilaterally Symmetric Vortex Rings" The Physics of Fluids, Vol. 15, No. 2, 1972, pp. 230–240.

102. Walker, J. D. A., Smith, C. R., Cerra, A. W., and Doligalski, T. L., "The Impact of a Vortex Ring on a Wall," J. Fluid Mech., Vol. 181, 1987, pp. 99–140.

103. Wan, T. and Payne, F., "An Unsteady Vortex-Ring Model for Microburst Simulation," AIAA paper 89-0811, 1989.

104. Webster, C. A. G., "A Note on the Sensibility to Yaw of a Hot-Wire Anemometer," J. Fluid Mech., Vol. 13, 1962, pp. 307–312. 1985.

105. Whitehead, K. D., "The Generation and Development of a Viscous Vortex Ring," Georgia Institute of Technology, School of Aerospace Engineering, Rep. 68–4, 1968.

106. Widnall, S. E. and Sullivan, J. P., "On the Stability of Vortex Rings," Proc. Roy. Soc., A 332, 1973, pp. 335–353.

107. Widnall, S. E., Bliss, D. B., and Tsai, C. Y., "The Instability of Short Waves on a Vortex Ring," J. Fluid Mech., Vol. 66, 1974, pp. 35–47.

108. Wu, J. M., Vakili, A. D., and Yu, F. M., "Investigation of Interacting Flow of Nonsymmetric Jets in Cross-Flow," AIAA J, Vol. 26, 1988, pp. 940–947.

109. Yamada, H. and Matsui, T., "Preliminary Study of Mutual Slip-Through of a Pair of Votices," The Phys. of Fluids, Vol. 21, 1978, pp.292–294.

110. Yamada H., Koshaka, T., Yamabe, H. and Matsui, T., "Flowfield Produced by a Vortex Ring near a Plane Wall," J. Physical Society of Japan, Vol 51, 1982, pp. 1663–1670.

111. Zawadzki, I and Aref, H., "Mixing during Vortex Ring Collision," Phys. Fluids A 3, 1991, pp. 1405–1410.

Appendices

Appendix A. Calibration of Hot-Film Anemometer

In this Appendix, an attempt has been made to describe the calibration setup as well as the calibration procedures for the hot-film probe. An accurate calibration is required to ensure high accuracy in the experimental results.

A.1 Description of Calibration Channel

The circular calibration water channel has been constructed as shown in Figure A.1. The water channel has the dimension of 218.5 *cm* long with 11.43 *cm* internal diameter. Two parallel steel rails are mounted on the upper side of the channel to be able to move a carriage back and forth. The carriage is made of aluminum and has two linear ball bearing supports on each side. A Motomatic E-500 D.C. servo motor which is mounted at one end of the channel is used to move the carriage. A steel cable passing over a set of 3.175 *cm* diameter pulleys drives the carriage. The speed range of the carriage is between 0.508 *cm/sec* and 81.28 *cm/sec*. A 1.27 *cm* wide opening was made on the top of the channel along the length of the channel.

Three photo-cells are installed at three different positions along the channel. The initial spacing between the first and second one ensures that the probe is travelling at a constant velocity in the measurement section. The second and third photo-cells sense the start and stop signals, respectively. Hence, by measuring the time between the second and third photo-cells the velocity can be calculated. After the carriage reaches the third photo-cell, it is halted and automatically returned to the position of the first photo-cell. The photo-cells that determine the length of the measurement section are 71.12 *cm* apart and located approximately 105.4 *cm* from the starting position of the carriage.

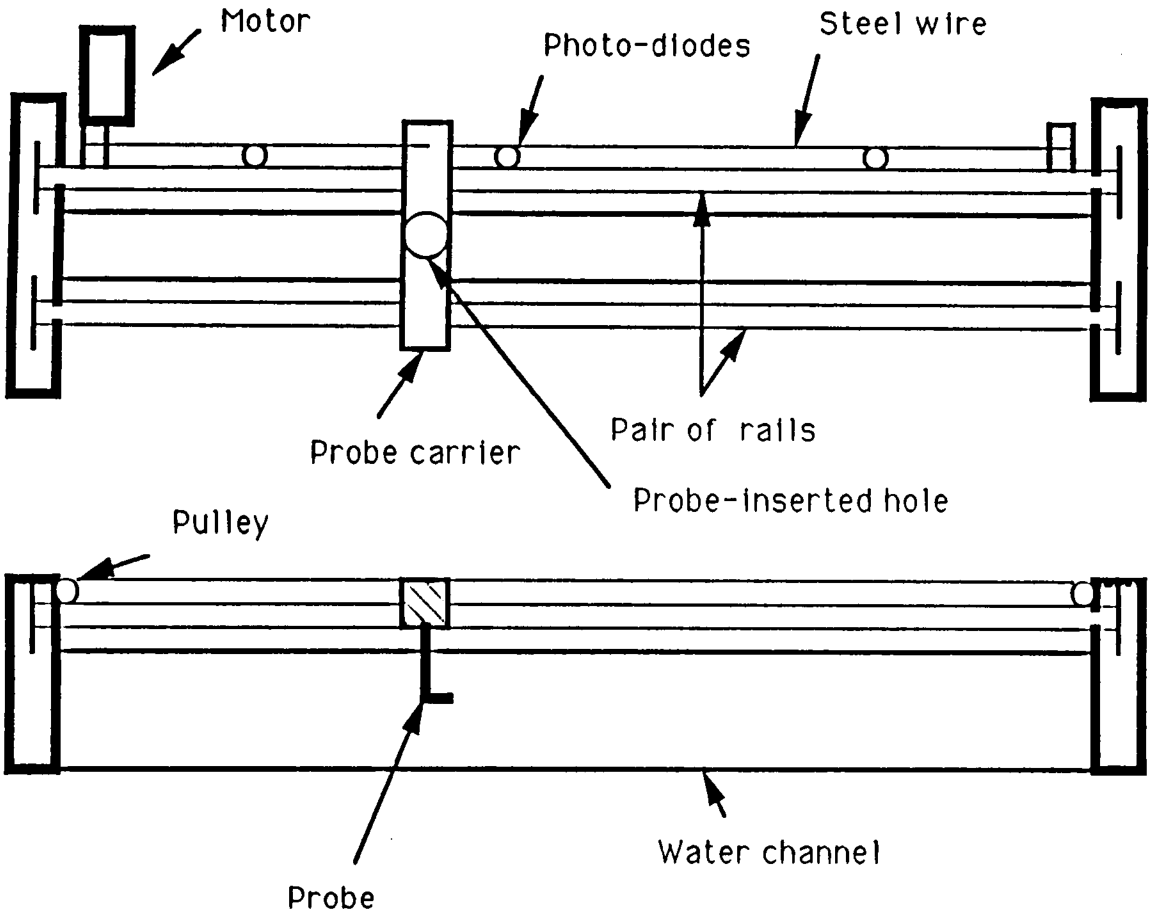

Figure A.1 Schematic of a calibration water channel

The hot-film probe and support are inserted into the carriage that can transverse the length of the water channel on its track. The probe sensor was located in a horizontal position with its axis perpendicular to the axis of the channel flow. At high speed of calibration, some period of time was necessary for water fluctuation to subside to an acceptable level.

A.2 Probe Calibration

The calibration of the probe was carried out over the required velocity range in the calibration channel mentioned above. The speed of the probe relative to the still water is directly measured and the time taken for calibration is sufficiently short such that there is no need to consider any temperature variation.

The probe was calibrated by adjusting the anemometer and recording their output voltages versus known velocity values. In general, the relationship between anemometer output voltages E and velocity V can be represented as:

$$E^2 = A + BV^n \qquad (A-1)$$

where A, B and n are constants to be determined from a linear regression least square curve fitting method. The typical unlinearized calibration curves for output voltages versus probe speed are shown in Figure A.2 for different ambient temperatures. The constants, A, B and n calculated from least square computer program are presented in each figure. First, n, A and B were evaluated to maintain least deviation curve at specific temperature. Then, A and B were computed with fixed n (in this work, it was $n = 0.34$) for the other temperature calibration.

When measurements are conducted at a temperature different from the calibration temperature, it is needed to correct for the temperature contamination of the velocity signals in the constant-temperature mode. In this study the water

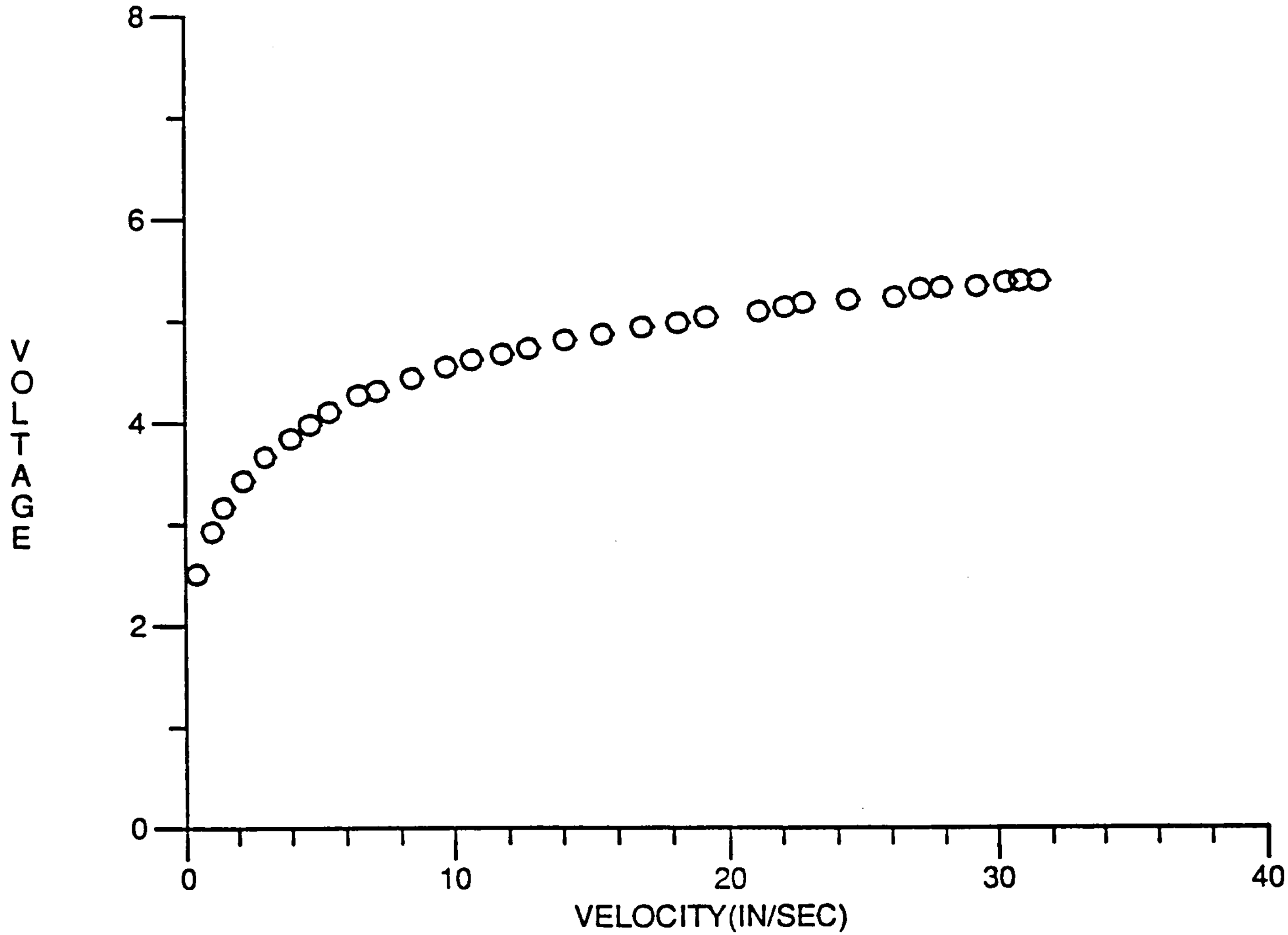

CALIBRATION CURVE FOR SINGLE PROBE AT 56 F.

Figure A.2 Unlinearized calibration curve

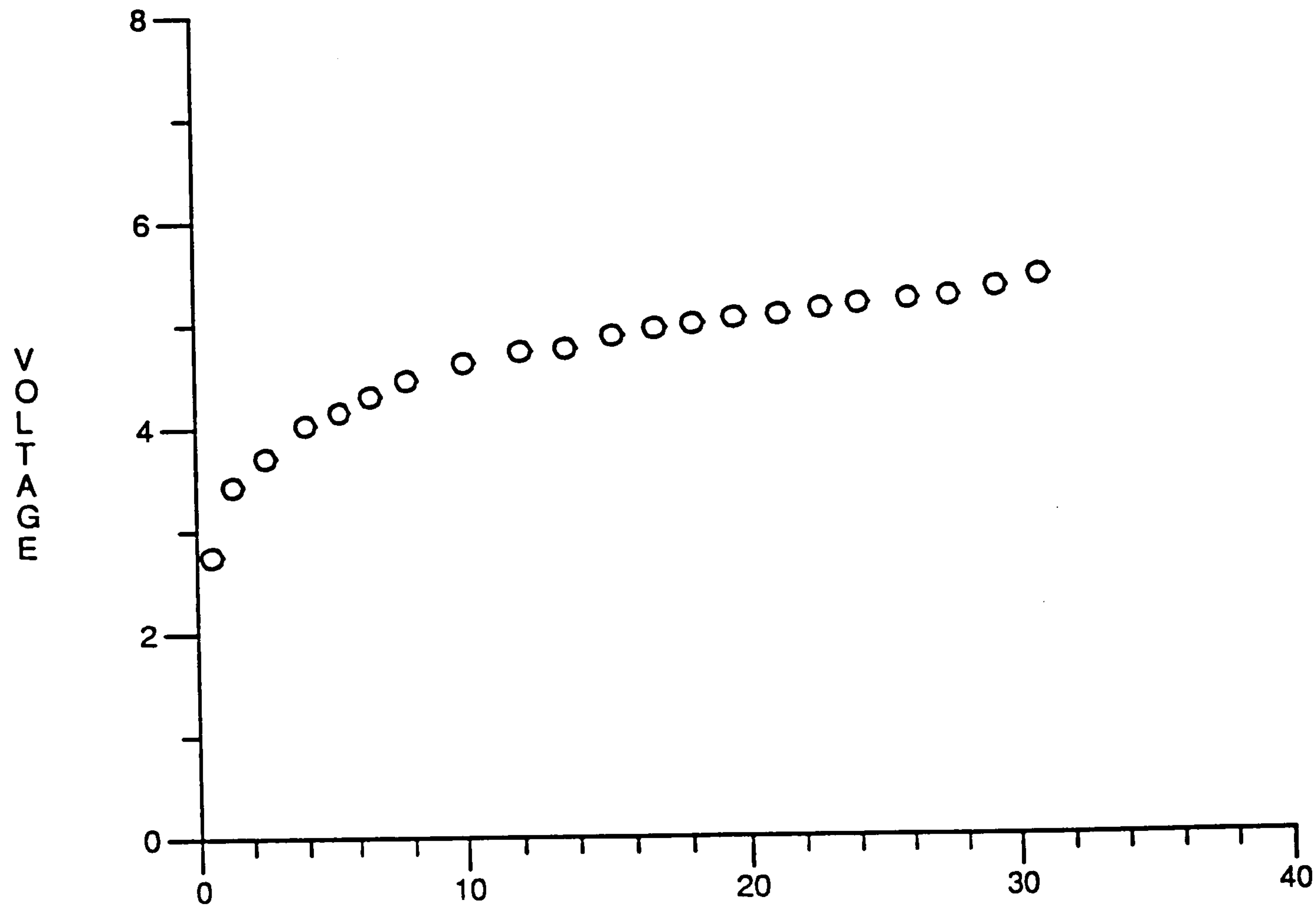

CALIBRATION CURVE FOR SINGLE PROBE AT 64 F.

Figure A.2 Continued

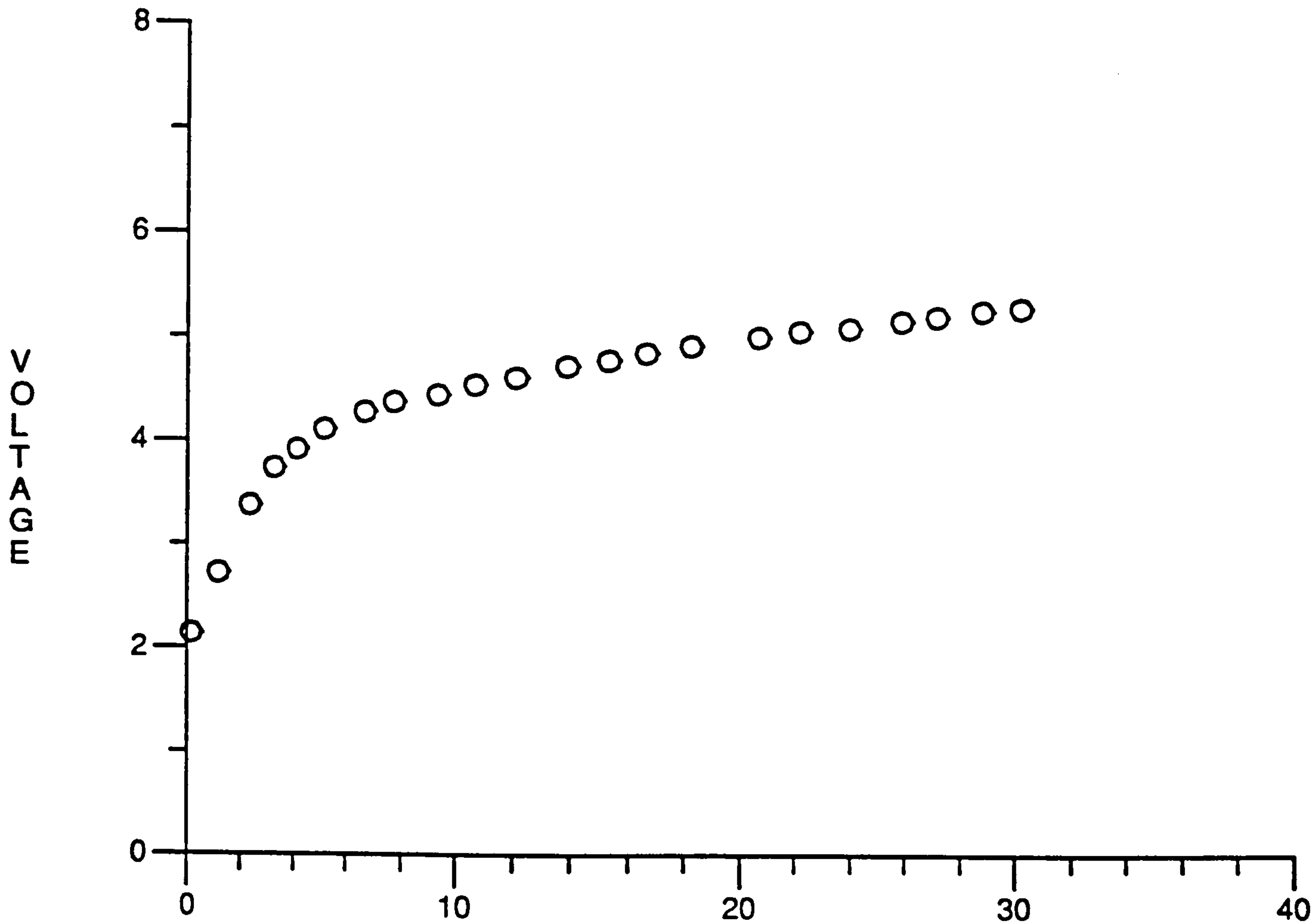

CALIBRATION CURVE FOR SINGLE PROBE AT 74 F.

Figure A.2 Continued

temperature of jet injection was different from the cross-flow temperature. Since the vortex ring moves downstream without significant entrainment from outside fluid, the jet temperature was assumed to be the ambient temperature for temperature calibration. A typical formulae to correct for the unlinearized output of a constant-temperature anemometer will be discussed by considering basic convective heat transfer from the sensor to its environment (Fingerson and Freymuth, 1983).

$$I_s{}^2 R_s = Nu \cdot \pi \cdot (2l) \cdot k_f \cdot (T_s - T_a) \qquad (A-2)$$

where

Nu = Nuselt number $(\frac{hd_s}{k_f})$

I_s = Probe current

R_s = Probe resistance

d_s = Sensor diameter

h = Convective heat transfer coefficient

k_f = Thermal mal conductivity of the fluid at the film temperature, T_f.

$T_f = \frac{1}{2}(T_s + T_a)$

T_s = Sensor temperature

T_a = Ambient temperature of fluid

$2l$ = Length of sensitive area of hot-film

Assuming a linear relationship between resistance and temperature:

$$R = R_r[1 + \alpha_r(T - T_r)] \qquad (A-3)$$

Therfore, the following can be written in terms of equation (A-3)

$$R_s = R_r[1 + \alpha_r(T_s - T_r)] \qquad (A-4)$$

$$R_a = R_r[1 + \alpha_r(T_a - T_r)] \qquad (A-5)$$

We can get the following expression by subtracting equation (A-5) from (A-4),

$$(R_s - R_a) = \alpha_r R_r (T_s - T_a) \qquad (A-6)$$

Arranging equations (A-2) and (A-6),

$$I_s^2 R_s = \frac{\pi \cdot (2l) k_f Nu}{\alpha_r R_r} \cdot (R_s - R_a) \qquad (A-7)$$

Kramers (1946) proposed an empirical relationship between the Nusselt number and the Reynolds number as followings:

$$Nu = 0.42 Pr^{0.26} + 0.57 Pr^{0.53} Re^{0.50} \qquad (A-8)$$

which covers the range $0.71 \leq \mathrm{Pr} \leq 525$ and $2.0 \leq \mathrm{Nu} \leq 20.0$. Fluid properties are to be selected at the film temperature, T_f. Equation (A-8) can be written in a similar form as King's law;

$$Nu = A' + B' \overline{U}_{eff}{}^{n} \qquad (A-9)$$

Comparing with equation (A-8),

$$A' = 0.42 Pr^{0.26}$$

$$B' = 0.57 Pr^{0.53} \left(\frac{d}{\nu}\right)^{0.50}$$

$$n = 0.50$$

Combining equations (A-7) and (A-9), we get

$$I_s^2 R_s = \frac{\pi (2l) k_f}{\alpha_r R_r} (R_s - R_a) [A' + B' \overline{U}_{eff}{}^{n}] \qquad (A-10)$$

The output voltage of anemometer, $\overline{E}$, is expressed in terms of the sensor current, I_s, as followings:

$$\overline{E} = [R_s + R_b + R_{cable}] I_s \qquad (A-11)$$

where

R_b = the bridge top resistance

R_{cable} = the cable resistance

Substituting equation (A-11) into equation (A-10),

$$\overline{E}^2 = \frac{\pi(2l)k_f}{\alpha_r R_r}\frac{(R_s - R_a)}{R_s}(R_s + R_b + R_{cable})^2[A' + B'\overline{U}_{eff}{}^n] \qquad (A-12)$$

Equation (A-12) can be written in the form of King's law,

$$\overline{E}^2 = A + B\overline{U}_{eff}{}^n \qquad (A-13)$$

where

$$A = \frac{\pi(2l)k_f}{\alpha_r R_r}\frac{(R_s - R_a)}{R_s}(R_s + R_b + R_{cable})^2 \cdot A' \qquad (A-14)$$

$$B = \frac{\pi(2l)k_f}{\alpha_r R_r}\frac{(R_s - R_a)}{R_s}(R_s + R_b + R_{cable})^2 \cdot B' \qquad (A-15)$$

Equation (A-13) can be expressed in terms of each condition as follows.

$$\overline{E}_c{}^2 = A_c + B_c\overline{U}_{eff}{}^n \qquad (A-16)$$

$$\overline{E}_a{}^2 = A_a + B_a\overline{U}_{eff}{}^n \qquad (A-17)$$

where

$$A_c = \frac{\pi(2l)k_f}{\alpha_r R_r}\frac{(R_s - R_c)}{R_s}(R_s + R_b + R_{cable})^2 \cdot A_c{}' \qquad (A-18)$$

$$B_c = \frac{\pi(2l)k_f}{\alpha_r R_r}\frac{(R_s - R_c)}{R_s}(R_s + R_b + R_{cable})^2 \cdot B_c{}' \qquad (A-19)$$

Also, in terms of ambient condition,

$$A_a = \frac{\pi(2l)k_f}{\alpha_r R_r}\frac{(R_s - R_a)}{R_s}(R_s + R_b + R_{cable})^2 \cdot A_a{}' \qquad (A-20)$$

$$B_a = \frac{\pi(2l)k_f}{\alpha_r R_r}\frac{(R_s - R_a)}{R_s}(R_s + R_b + R_{cable})^2 \cdot B_a{}' \qquad (A-21)$$

Assuming constant fluid properties and a linear relationship between resistance and temperature, we can derive the following form.

$$\frac{A_c}{A_a} = \frac{R_s - R_c}{R_s - R_a} = \frac{T_s - T_c}{T_s - T_a} \qquad (A-22)$$

$$\frac{B_c}{B_a} = \frac{R_s - R_c}{R_s - R_a} = \frac{T_s - T_c}{T_s - T_a} \qquad (A-23)$$

Therefore, a simple expression for the relation between actual measured value and corrected output is found by combining equations (A-16), (A-17), (A-22) and (A-23).

$$\overline{E}_c = (\frac{T_s - T_c}{T_s - T_a})^{\frac{1}{2}} \overline{E}_a \qquad (A-24)$$

The above simple form was used to correct the temperature difference between calibration and actual temperature in this experiment. In Appendix C, the equation (A-24) is useful for uncertainty analysis.

In order to determine the directional characteristics of the probe, yaw and pitch effects on the cooling velocity should be considered. The effective cooling velocity was given in terms of yaw and pitch factors in equation (3-1).

$$U_{eff}{}^2 = U_N{}^2 + k_1{}^2 U_T{}^2 + k_2{}^2 U_{BN}{}^2 \qquad (3-1)$$

Refer to Figure 3.11.

For the case of zero pitch angle,

$$U_{eff}(\phi)^2 = U^2(0)(\cos^2\phi + k_1{}^2\sin^2\phi) \qquad (3-2)$$

For the case of zero yaw angle,

$$U_{eff}(\psi)^2 = U^2(0)(\cos^2\psi + k_1{}^2\sin^2\psi) \qquad (3-3)$$

where

k_1 = yaw factor

k_2 = pitch factor

ϕ = yaw angle

ψ = pitch angle

The following simple expressions for the yaw and pitch factors can be derived from equations (A-1), (3-2) and (3-3).

$$k_1 = \frac{1}{\sin\phi}[(\frac{E^2(\phi) - A}{E^2(0) - A})^{\frac{2}{n}} - \cos^2\phi]^{\frac{1}{2}} \qquad (A-25)$$

$$k_2 = \frac{1}{\sin\psi}[(\frac{E^2(\psi) - A}{E^2(0) - A})^{\frac{2}{n}} - \cos^2\psi]^{\frac{1}{2}} \qquad (A-26)$$

The yaw factor k_1 was evaluated using equation (A-25) and presented as a function of yawing angle ϕ at two different velocities as shown in Figure A.3. It is found that the yaw factor decreases with increasing values of yaw angles. This agrees with the results of Jorgensen (1971). It appears that the yaw factor k_1 is slightly reduced with increasing velocity for whole range of yaw angles. Jorgensen (1971) suggested that the value of k_1 selected for $\phi = 90°$ may be used inside the full range of ϕ from 0° to 90°, which is resulting in errors on $U(0)$ from 4% to 10%, increasing with decreasing prong spacing and length-to-diameter ratio. Accoring to his suggestion, k_1 was incorporated into the data reduction program to consider the yaw effect in this study.

The pitch effect is known to be due to the blockage of the probe body on the flow and changes in heat conduction to the prong with varying degrees of inclination relative to the direction of flow. The pitch factor k_2 depends on sensor geometry and prong length, however, since the pitch factor k_2 is nearly constant inside the full range of ψ from 0° to 90°, it was not considered in this investigation.

Neglecting the pitch correction, the maximum errors occurred are usually between 5 and 12% (Jorgensen, 1971).

Appendix B. Output Signal Analysis

In order to analyze the output signal in the general three-dimensional flow field, a general slanted probe is considered in Figure B.1. The effect of the velocity vector depends both on its magnitude and direction, and the method of decomposition chosen depends on the coordinate system which is used. Although the results are required in a 'laboratory coordinate system', the calibration and analysis of the hot-wire/film is best considered in a 'probe-fixed coordinate system'. Therefore the 'laboratory coordinate system' can be transformed to the 'probe-fixed coordinate system' through the following system of equations (1985):

$$U_T = U cos\theta sin\alpha - V sin\theta sin\alpha - W cos\alpha \qquad (B-1)$$

$$U_N = U cos\theta cos\alpha + V sin\theta cos\alpha + W sin\alpha \qquad (B-2)$$

$$U_{BN} = U sin\theta + V cos\theta \qquad (B-3)$$

where α is the probe slant angle and θ is the rotation angle measured from the reference plane about Z-axis. Substituting equations (B–1) through (B–3) into (3–1) and expanding:

$$\begin{aligned} U_{eff}{}^2 = & [\cos^2\theta(\cos^2\alpha + k_1{}^2\sin^2\alpha) + k_2{}^2\sin^2\theta]U^2 + \\ & [\sin^2\theta(\cos^2\alpha + k_1{}^2\sin^2\alpha) + k_2{}^2\cos^2\theta]V^2 + \\ & (\sin^2\alpha + k_1{}^2\cos^2\alpha)W^2 + \\ & [\sin 2\theta(\cos^2\alpha - k_1{}^2\sin^2\alpha + k_2{}^2]UV + \\ & [\sin 2\alpha \sin\theta(1 + k_1{}^2)]VW + \\ & [\sin 2\alpha \cos\theta(1 - k_1{}^2)]WU \end{aligned} \qquad (B-4)$$

Since the instantaneous velocity is the sum of time-mean and fluctuating velocities, it can be split as follows:

$$U = \overline{U} + u' \qquad (B-5)$$

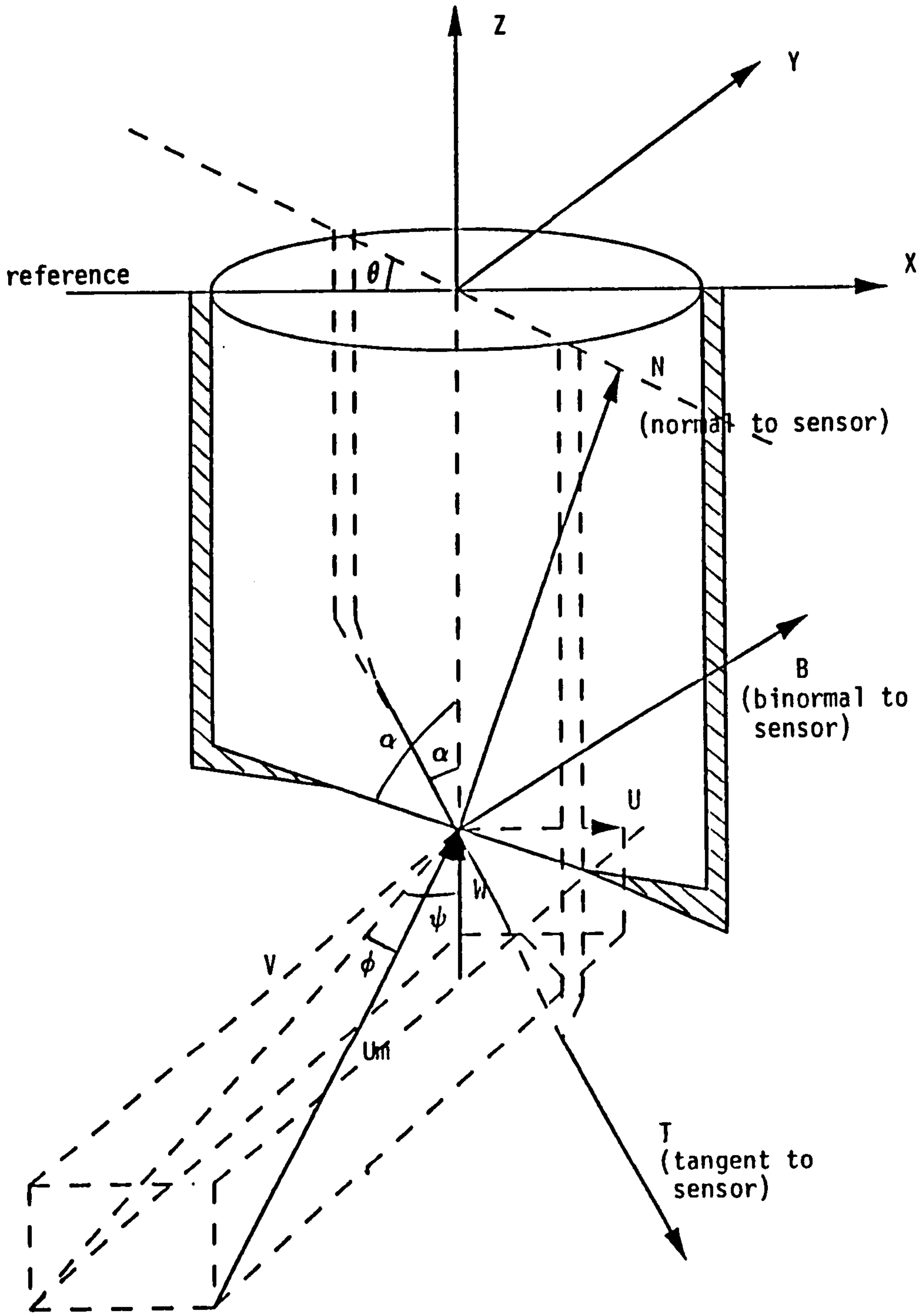

Figure B.1 Schematic of a hot-wire/film sensor in the three dimensional flow field

$$V = \overline{V} + v' \qquad (B-6)$$

$$W = \overline{W} + w' \qquad (B-7)$$

Also,

$$U_{eff} = \overline{U}_{eff} + u'_{eff} \qquad (B-8)$$

Substituting equations (B–5) through (B–8) into equation (B–4) and time-averaging both sides of the equation. The time-averaged and fluctuating parts of the instantaneous effective cooling velocity can be obtained. Since we are measuring only the time-averaged part during the experiment, the fluctuating part will not be considered here. The time-averaged part of the effective cooling velocity becomes:

$$\begin{aligned}\overline{U}_{eff}{}^2 =& [\cos^2\theta(\cos^2\alpha + {k_1}^2\sin^2\alpha) + {k_2}^2\sin^2\theta]\overline{U}^2 + \\ & [\sin^2\theta(\cos^2\alpha + {k_1}^2\sin^2\alpha) + {k_2}^2\cos^2\theta]\overline{V}^2 + \\ & (\sin^2\alpha + {k_1}^2\cos^2\alpha)\overline{W}^2 + \\ & [\sin 2\theta(\cos^2\alpha - {k_1}^2\sin^2\alpha + {k_2}^2]\overline{UV} + \\ & [\sin 2\alpha\sin\theta(1 + {k_1}^2)]\overline{VW} + \\ & [\sin 2\alpha\cos\theta(1 - {k_1}^2)]\overline{WU}\end{aligned} \qquad (B-9)$$

For the single probe ($\phi = 90°$), the above equation is reduced to:

$$\begin{aligned}\overline{U}_{eff}{}^2 =& [{k_1}^2\cos^2\theta + {k_2}^2\sin^2\theta]\overline{U}^2 + \\ & [{k_1}^2\sin^2\theta + {k_2}^2\cos^2\theta]\overline{V}^2 + \overline{W}^2 + \\ & [\sin 2\theta({k_2}^2 - {k_1}^2)]\overline{UV}\end{aligned} \qquad (B-10)$$

We can determine the time-averaged velocity components $\overline{U}$ and $\overline{W}$ simply by rotating the probe about the Z-axis. Since the velocity component $\overline{V}$ is one order of magnitude less than either $\overline{U}$ or $\overline{W}$, the term $\overline{V}$ can be neglected for the vortex ring problem in cross-flow. This assumption actually considers the vortex rings problem in cross-flow as two-dimensional. Many investigators adopted this assumption for the study of the jet problem in cross-flow (Pattern (1974), Sherif (1985)). For the $\theta = 90°$ of the single probe, equation (B–10) reduced to

$$\overline{U}_{eff}^{\,2}(\theta = 90°) = k_2^{\,2}\overline{U}^2 + \overline{W}^2 \qquad (B-11)$$

For the $\theta = 0°$ of the single probe, equation (B-10) reduced to

$$\overline{U}_{eff}^{\,2}(\theta = 0°) = k_1^{\,2}\overline{U}^2 + \overline{W}^2 \qquad (B-12)$$

This system of equations is linear with two unknowns $\overline{U}^2$ and $\overline{W}^2$. Hence the mean velocity components will be

$$\overline{U}^2 = \frac{1}{k_2^{\,2} - k_1^{\,2}}(\overline{U}_{eff}^{\,2}(\theta = 90°) - \overline{U}_{eff}^{\,2}(\theta = 0°)) \qquad (B-13)$$

$$\overline{W}^2 = \frac{1}{k_2^{\,2} - k_1^{\,2}}(k_2^{\,2}\overline{U}_{eff}^{\,2}(\theta = 0°) - k_1^{\,2}\overline{U}_{eff}^{\,2}(\theta = 90°)) \qquad (B-14)$$

Appendix C. Uncertainty of Experimental Results

C.1 Error Analysis

An attempt has been made to estimate the magnitude of the uncertainties in terms of the various measurements and experimental methods in this experimental study.

Any measurement has some errors which are the differences between the measured values and the true values due to finite test numbers and inaccuracy in the experimental technique. Uncertainty is defined by the maximum error which might reasonably be expected and is a measure of accuracy, i.e., the closeness of the measurement to the true value (Abernethy, et al. 1973).

There are two types of measurement error; fixed and random error. The fixed error arises from the improper experimental procedures characterized by systematic and consistent nature. On the other hand, the random error is occurred in repeated measurements characterized by inconsistent and random nature. It is possible to minimize the fixed errors by proper experimental procedures.

The uncertainties caused by water tunnel and experimental setup including vortex ring generator:

(1) Freestream turbulence levels were less than 0.1% of the freestream (cross-flow) velocity (Collins, 1982).

(2) The maximum temperature drift of the cross-flow was less than $\pm 0.28°$ for each run.

(3) Uncertainty in flow meter during the pulsation was 0.033 GPM (10%).

(4) Frequency uncertainty in frequency generator was less than $\pm 2.5\%$.

The uncertainties introduced by hot-film measurements:

(1) The calibration constants (A and B) was $\pm 4\%$.

(2) the probe position in the streamwise direction is ± 0.0159 cm.

(3) the probe position in the vertical direction is ± 0.0254 cm.

(4) the probe position in the spanwise direction is ± 0.0254 cm.

(5) the probe position in the angular direction (yaw and pitch) is $\pm 2.5°$.

The uncertainty in the calculated value can be evaluated using the following standard uncertainty equation (Kline and McClintock, 1953) based upon the uncertainties in the primary measurements:

$$\Delta Q = [(\frac{\partial Q}{\partial X_1}\Delta X_1)^2 + (\frac{\partial Q}{\partial X_2}\Delta X_2)^2 + \cdots + (\frac{\partial Q}{\partial X_n}\Delta X_n)^2]^{\frac{1}{2}} \qquad (C-1)$$

where

$Q = Q(X_1, X_2, X_3, \cdots, X_n)$.

ΔQ is the uncertainty of quantity Q.

ΔX_i is the uncertainty of the independent variables.

In the above expressions, the uncertainties of the independent variables are assumed to be all given with the same odds. The uncertainty obtained from the above equation $(C-1)$ is the maximum expected deviation from the measured value.

In the next sections, uncertainties associated with the mean jet velocity, sensor operating temperature, corrected effective cooling velocity, time-averaged mean velocity components, the measurement of circulation, translational velocity, core size and ring size will be estimated using the equation $(C-1)$ in the derived or computed quantities in the present study.

The following uncertainties estimated for a typical vortex ring at $Z = 3d_j$ are valid for all vortex ring cases with the same odds.

C.2 Uncertainty in Mean Jet Velocity

The mean jet velocity in the steady flow is given by

$$\overline{U}_j = \frac{15.402\dot{Q}}{\pi {d_j}^2} \qquad (C-2)$$

where d_j is jet exit diameter in *inch* and $\dot{Q}$ is a flow rate in GPM. Applying the equation $(C-1)$ to equation $(C-2)$, we can evaluate the uncertainty in mean jet velocity as followings.

$$\Delta\overline{U}_j = [(\frac{15.402\Delta\dot{Q}}{\pi {d_j}^2})^2 + (\frac{-30.804\dot{Q}\Delta d_j}{\pi {d_j}^3})^2]^{\frac{1}{2}} \qquad (C-3)$$

where

$d_j = 0.500\ in \pm 0.001\ in$

$\dot{Q} = 0.300\ GPM \pm 0.033\ GPM$ at $\overline{U}_j = 5.88\ in/sec.$

Therefore,

$$\begin{aligned}\Delta\overline{U}_j =& [(\frac{15.402 \cdot 0.033}{\pi(0.500)^2})^2 + \\ & (\frac{-30.804 \cdot 0.300 \cdot 0.001}{\pi(0.500)^3})^2]^{\frac{1}{2}} \\ =& \ 0.648\ in/sec\ \ or\ \ 1.646\ cm/sec\ \ or\ \ 11.01\%\ \ of\ \ \overline{U}_j\end{aligned}$$

C.3 Uncertainty in Sensor Operating Temperature

The sensor operating resistance determines the operating temperature due to the probe's linear relationship between resistance and temperature in the constant-temperature mode. The linear relationship can be represented as:

$$R_s = R_r[1 + \alpha_r(T_s - T_r)] \qquad (C-4)$$

where

R_r = resistance at reference temperature, T_r

T_s = average sensor operating temperature

α_r = temperature coefficient of resistance

The value of α_r will be dependent on the reference temperature, T_r. The sensor operating resistance, R_s, can be expressed in terms of the overheat ratio (OHR):

$$R_s = R_r \cdot OHR \qquad (C-5)$$

Comparing the equations $(C-4)$ and $(C-5)$, the sensor operating temperature, T_s, can be written as:

$$T_s = \frac{(OHR-1)}{\alpha_r} + T_r \qquad (C-6)$$

where T_r is a fixed reference temperature.

Applying the equation $(C-1)$ to $(C-6)$, we get the expression for the uncertainty of sensor operating temperature, ΔT_s.

$$\Delta T_s = [(\frac{\Delta(OHR-1)}{\alpha_r})^2 + (\frac{-(OHR-1)\cdot\Delta\alpha_r}{{\alpha_r}^2})^2]^{\frac{1}{2}} \qquad (C-7)$$

Typical values selected for this experiment are

$(OHR-1) = 0.04 \pm 0.005$

$\alpha_r = 0.0022 \pm 0.00005$

So,

$$\begin{aligned}\Delta T_s =& [(\frac{0.0005}{0.0022})^2 + \frac{(0.04\cdot 0.00005}{0.0022^2)}^2]^{\frac{1}{2}}\\ &= 0.22^\circ\ F \ \ or\ \ 0.15\%\ \ of\ \ T_s = 152.06^\circ\end{aligned}$$

C.4 Uncertainty in Corrected Effective Cooling Velocity

If the temperature change is slow, the following technique can be used for correcting the output data for the temperature difference between calibration and actual ambient temperature as derived in Appendix A.

$$\overline{U}_{eff,c} = (\frac{T_s - T_{cal}}{T_s - T_a})^{\frac{1}{2}} \cdot \overline{U}_{eff} \qquad (C-8)$$

where

T_{cal} = calibration temperature

T_a = ambient temperature

Applying the equation $(C-1)$ to $(C-8)$ and neglecting the uncertainty, $\Delta\overline{U}_{eff}$, we get the uncertainty in the corrected effective cooling velocity as followings:

$$\begin{aligned}\Delta\overline{U}_{eff,c} =& [(\frac{-\overline{U}_{eff}}{(T_s - T_a)^{\frac{1}{2}}(T_s - T_{cal})^{\frac{1}{2}}} \cdot \Delta T_{cal})^2 \\ &+ (\frac{-(T_s - T_{cal})^{\frac{1}{2}}}{2(T_s - T_a)^{\frac{3}{2}}} \cdot \overline{U}_{eff}\Delta T_a)^2 \\ &+ (\frac{\overline{U}_{eff}(T_{cal} - T_a)}{2(T_s - T_{cal})^{\frac{1}{2}}(T_s - T_a)^{\frac{3}{2}}} \cdot \Delta T_s)^2]^{\frac{1}{2}}\end{aligned} \qquad (C-9)$$

The typical values for the run number 130364 at $Z = 3d_j$ are:

$T_s = 152.06°$ F

$T_{cal} = 55.0°$ F

$T_a = 58.5°$ F

The effective cooling velocity output for the same run number at probe angle $\theta = 90°$ was $\overline{U}_{eff} = 10.485$ in/sec. Using the equation $(C-8)$, $\overline{U}_{eff,c}$ was obtained as 10.679 in/sec. The uncertainty in the temperature, ΔT_{cal}, during the calibration was at most $0.5°F$, and the temperature uncertainty, ΔT_a, in the course of the experiments was below $0.2°F$. The uncertainty in sensor temperature was evaluated as $\Delta T_s = 0.22°F$ in the above section.

Therefore, the uncertainty of the effective cooling velocity in this case is

$$\begin{aligned}\Delta\overline{U}_{eff,c} =& [(\frac{-10.485}{(152.06-58.50)^{\frac{1}{2}}(152.06-55.00)^{\frac{1}{2}}}\cdot 0.5)^2 \\ &+ (\frac{-(152.06-55.00)^{\frac{1}{2}}}{2(152.06-58.50)^{\frac{3}{2}}}\cdot 10.485\cdot(0.2))^2 \\ &+ (\frac{10.485(55.00-58.50)}{2(152.06-55.00)^{\frac{1}{2}}(152.06-58.50)^{\frac{3}{2}}}\cdot 0.2224)^2]^{\frac{1}{2}} \\ &= 0.060\ in/sec\ \ or\ \ 0.153\ cm/sec\ \ or\ \ 0.563\%\ \ of\ \ \overline{U}_{eff,c}\end{aligned}$$

C.5 Uncertainties in Mean Velocity Components

The mean velocity components in the streamwise and vertical directions ($\overline{U}$ and $\overline{W}$) were derived in the equations (3-16) and (3-17).

$$\overline{U} = [\frac{1}{{k_2}^2-{k_1}^2}({\overline{U}_{eff,c}}^2(\theta=90°)-{\overline{U}_{eff,c}}^2(\theta=0°))]^{\frac{1}{2}} \qquad (C-10)$$

$$\overline{W} = [\frac{1}{{k_2}^2-{k_1}^2}({k_2}^2{\overline{U}_{eff,c}}^2(\theta=0°)-{k_1}^2{\overline{U}_{eff,c}}^2(\theta=90°))]^{\frac{1}{2}} \qquad (C-11)$$

Applying the equation $(C-1)$ to equations $(C-4)$ and $(C-5)$, we can estimate the uncertainties in the $\overline{U}$ and $\overline{W}$ as followings.

$$\begin{aligned}\Delta\overline{U} =& \frac{1}{\overline{U}\cdot({k_2}^2-{k_1}^2)}\cdot[(\overline{U}_{eff,c}(\theta=90°)\cdot\Delta\overline{U}_{eff,c}(\theta=90°))^2 \\ &+(\overline{U}_{eff,c}(\theta=0°)\cdot\Delta\overline{U}_{eff,c}(\theta=0°))^2]^{\frac{1}{2}}\end{aligned} \qquad (C-13)$$

$$\begin{aligned}\Delta\overline{W} =& \frac{1}{\overline{W}\cdot({k_2}^2-{k_1}^2)}\cdot[({k_2}^2\overline{U}_{eff,c}(\theta=0°)\cdot\Delta\overline{U}_{eff,c}(\theta=0°))^2 \\ &+({k_1}^2\overline{U}_{eff,c}(\theta=90°)\cdot\Delta\overline{U}_{eff,c}(\theta=90°))^2]^{\frac{1}{2}}\end{aligned} \qquad (C-14)$$

By substituting typical values for the above parameters, The estimated uncertainties for the mean velocities $\overline{U}$, and $\overline{W}$ are

$$\begin{aligned}\Delta\overline{U} =& \frac{1}{5.4657\cdot(1.0^2-0.258^2)} \\ &\cdot[(10.679\cdot 0.06012)^2+(9.282\cdot 0.0488)^2]^{\frac{1}{2}} \\ &= 0.154\ in/sec\ \ or\ \ 0.391\ cm/sec\ \ 2.82\%\ \ of\ \ \overline{U}\end{aligned}$$

Also,

$$\Delta\overline{W} = \frac{1}{9.1742 \cdot (1.0^2 - 0.258^2)} \cdot \left[(1.0^2 \cdot 9.282 \cdot 0.0488)^2 + (0.258^2 \cdot 10.679 \cdot 0.06012)^2\right]^{\frac{1}{2}}$$

$$= 0.053\ in/sec \ \ or\ \ 0.135\ cm/sec\ \ 0.58\%\ \ of\ \ \overline{W}$$

C.6 Uncertainty in Translational Velocity

At the inner edge of the core, the velocity, $\overline{W}$, is given as the sum of core rotational velocity, U_{rot}, and ring translational velocity, U_T. On the other hand, the vertical velocity component is the difference between U_{rot} and U_T at the outer edge of the core. Therefore, the translational velocity, U_T, was calculated from the inner edge and outer edge velocities of the vortex core. Since the translational velocity is directly obtained from the vertical velocity component $\overline{W}$, the uncertainty in the translational velocity is supposed to be the same order of magnitude as that of the mean vertical velocity, $\Delta\overline{W}$, obtained from previous section for the same run number. It is noted here that any uncertainty caused by theoretical analysis was neglected. By the same argument, it is considered that the uncertainty in the rotational velocity U_{rot} has the same order of magnitude.

C.7 Uncertainty in Ring Size Measurements

The uncertainty in the core diameter is determined by how we can measure the exact vortex core center. The core center was detected by the trace when the center of the core passes over the hot-film probe. The outstanding dip was found in the mid of the trace, which is caused by the rotation of the vortex ring core. The magnitude of minimum dip is responsible for the translational velocity. Therefore, there is only one uncertainty in the core measurement which is is the uncertainty in the radial distance moved. The uncertainty in the radial distance moved is occurred from the uncertainty in determining the exact horizontal location of the center of the vortex ring core. The core center location error is estimated to be 0.0125 *cm* around the core center. Therefore, the uncertainty in the core radius is expressed by the simplified form,

$$\Delta a = [(\frac{\Delta X_a}{a})^2]^{\frac{1}{2}} \qquad (C-15)$$

By substituting $X_a = 0.0125\ cm$ and $a = 0.3175\ cm$, The uncertainty of core radius is estimated to be

$$\Delta a = 0.0394 = 3.94\%$$

Since the uncertainty in the ring radius is related to the ring center position as well as the core, the equation (C-15) can be modified by considering above two effects as follows:

$$\Delta R = [(\frac{\Delta X_a}{a})^2 + (\frac{\Delta X_c}{R})^2]^{\frac{1}{2}} \qquad (C-16)$$

Typical values are $X_c = 0.025\ cm$ and $R = 1.08\ cm$ for $Z = 3d_j$. Therefore, the estimated uncertainty in the ring radius measurements becomes

$$\Delta R = 0.0457 = 4.57\%$$

C.8 Uncertainty in Circulation Measurements

The measured circulation can be estimated directly from the core circulation of the vortex ring from the following relationships. In this case,

$$\Gamma_m = \frac{\Gamma_c}{0.715} \qquad (C-17)$$

$$\Gamma_c = 2\pi a \cdot U_{rot} \qquad (C-18)$$

By assuming that there is no uncertainty due to the theoretical analysis, the uncertainty in the circulation $\Delta\Gamma_m$ can be evaluated as followings.

$$\Delta\Gamma_m = \frac{2\pi}{0.715}\left[(U_{rot}\cdot\Delta a)^2 + (a\cdot\Delta U_{rot})^2\right]^{\frac{1}{2}} \qquad (C-19)$$

Therefore, the uncertainty in the measured circulation becomes

$$\begin{aligned}\Delta\Gamma_m =& \frac{2\pi}{0.715}[(12.981\cdot 0.0394)^2 + (0.3175\cdot 0.053)^2]^{\frac{1}{2}}\\ &= 4.497\ cm^2/sec \ \ or \ \ 12.42\% \ \ of \ \ \Gamma_m = 36.218\ cm^2/sec\end{aligned}$$

Vita

Young Keun Chang was born on October 27, 1957 in Seoul, Republic of Korea. He received the Bachelor of Science in Mechanical Engineering with honors from Hankuk Aviation University in February, 1981. The following March he entered Seoul National University with a national fellowship. In February, 1983 he received Master of Science in Mechanical Engineering there. Upon graduating from Seoul National University, he joined the Korea Third Military Academy and discharged as an officer in January, 1984. The following February he joined to work for Technical Center, Daewoo Motor Company, in Incheon, Korea. He worked as a Research and Design Engineer in the area of internal combustion engine there for two and half years.

He entered The Virginia Polytechnic Institute and State University in September 1986 as a graduate research assistant. He was awarded Master of Science with a major in Aerospace Engineering in September 1988. He has continued his Ph.D. study in the Department of Aerospace Engineering in The University of Tennessee Space Institute, and completed a degree of Doctor of Philosophy with a major in Aerospace Engineering in September, 1991.

He is a member of American Institute of Aeronautics and Astronautics and Korean Society of Mechanical Engineers.

He is married to the former Hye Jung Choi in Seoul, Korea. They have one lovely son, Jiwon and one beautiful daughter, Jenny.